Thanks to the work of the editors and reviewers.

The corrected manuscript is on Page 10—42, in which the corrections have been highlighted with different colors and numbered.

Corrections corresponding to the first reviewer are highlighted with magheta color and labeled with “An”
Corrections corresponding to the second reviewer are highlighted with green color and labeled with “Bn”

Some sections, such as the ‘Abstract’ and ‘Discussion’, are with important corrections as suggested by the reviewers. So the title of these sections have been highlighted.

Thanks to the reviewer for the very helpful advice. We appreciate the reviewer's help and effort in reviewing this paper. The answers to the reviwers' are listed below.

A unique data set of mineral dust optical properties taken in western China close to the Taklamakan desert is presented. The observations were performed with an advanced multiwavelength Raman and polarization lidar. It is probably (almost) impossible for non-Chinese research teams to travel to the westernmost part of China. This makes the data set so valuable.
The paper is well written. I recommend publication after minor revision.

Abstract: Do we need all these details to all 4 discussed cases in the abstract? A few summarizing sentences would be sufficient to my opinion! **see A1**
Answer: The abstract has been modified.

Introduction: P2,L26: Please mention the important role of dust particles to serve as ice-nucleating particles, reference: Kanji, Z. A., Ladino, L. A., Wex, H., Boose, Y., Burkert-Kohn, M., Cziczo, D. J., and Kramer, M.: Chapter 1: Overview of ice nucleating particles, Meteor Monogr., Am. Meteorol. Soc., 58, 1.1-1.33, https://doi.org/10.1175/amsmonographs-d-16-0006.1, 2017.
see A2
Answer: It is added. Thanks for the suggestion.

P2, L46: Besides the Hofer 2017 paper there are two additional Hofer papers in 2020. The last of these three articles is on lidar ratios and depolarization ratios measured '…a few kilometers upwind…' of your Kashi lidar station. This paper should be used for comparison regarding the potential impact of long-range transport of dust and pollution advected from Africa and the Middle East.
see A3 and the manuscript
Answer: Hofer et al. 2020 has been cited and used as comparison in the manuscript.

P4, L92: Basic information about the methods (Fernald, Raman, smoothing lengths, least squares fit, reference height in backscatter determination, input parameters) regarding the computation of the backscatter and extinction coefficients would be fine. The same for the retrieval of the particle depolarization ratio from the volume depolarization ratios. Information on the used temperature and pressure profiles is required. Did you use GDAS profiles? Kashi is a radiosonde station, that means the re-analyzed GDAS data consider these radiosonde observations and are thus perfect to be used in your lidar data analysis. **see A4**
Answer: A brief introduction to the input parameters in the calculation has been added in the manuscript. We did not use the re-analyzed data from GDAS. The temperature and pressure profiles needed in the data processing are from the radio sounding measurements obtained from the radiosonde site ~6 km to the observation site. There are 2 measurements per day. The time difference between our lidar measurements and the radiosonde measurements is about a few hours.

P4, L116: Improve I… , better write I340 and I380 represent…
Answer: It has been corrected in the manuscript. **see A5**

P5, L142: Are you sure that the photometer can correctly measure an AOD of 4.7?

Answer: It is true that the AOD =4.7 is touching the limit of the capability of the sun photometer. The measurement was taken by an old version sun photometer who max AOD could be about 4.0 (With the new version photometer, CE318-N, the max AOD could reach 7.0). Under this condition, the incident solar radiation was very weak, but not that weak because the solar zenith angle is still enough. So the accuracy of the the detection might decrease but not the result should not be rediculously wrong. A brief explanation been added in the manuscript: "It should be noted, in this extreme case, the accuracy of the measured AOD (i.e. 4.70) may degrade because of decreased signal-to-noise ratio. " By the way, we are using this value to prove, qualitatively, that the AOD was extremely high, and never used it in any scientific calculation. **see A6**

P6, Case 1: The depolarization ratios point to pure dust, and more important, to nearsource dust with a large fraction of coarse particles and especially giant particles (radius > 20 microns). This is probably the reason for the strong difference between the lidar ratio at 355 nm of around 60 sr and of 45 sr for 532 nm and the corresponding backscatter wavelength dependence. The Dushanbe observations (Hofer papers) of central Asian, Saharan, and Middle East dust did not show that. Should be discussed.

Answer: Thank you for the advice. This argument has been added in the presentation of Case 1 and in the discussion part.

see A7

P6-7: Case 2 is almost 'no case', and indicates again the dominance of giant dust particles, causing these extremely large particle depolarization ratios of 0.32 at 355 nm and 0.37 at 532 nm. It should be mentioned that the depolarization ratios were exceptionally high because of the presence of very large particles. Burton et al. (ACP) measured very high depolarization ratios at 532 nm close to dust sources, but never at 355 nm. Should be discussed.

Answer: A short discussion has been added in the end of Case 2.

see A8

P7-8: Case 3: You mention that this is a polluted case, ..and dust was contaminated and coated. Do you have clear indications for that? There is long debate on external or internal mixture of dust and pollution aerosol. Researchers (e.g., Kandler and his team) who investigated Saharan dust particles in the Caribbean did not find any significant coating. They found the same during the SAMUM-2 campaign with strong pollution and dust mixtures. Kandler did not find strong hinds on coating and concluded that dust and pollution is mainly externally mixed. If you do not have clear hinds on coating then one should clearly indicate that by writing… we hypothesize that dust is coated or so…. **see A9**

Answer: We realized that it is not cautious to say "…but when *coated* by hygroscopic aerosol species…". Due to the lack of aerosol samples at the boundary layer top, we do not have enough evidence to tell the occurrence of hygroscopic growth and the mix00ing state of dust and pollution. The above mentionned paragraph has been rewritten:

"but when mixed with hygroscopic aerosol species, for example, nitrate, the ensemble of aerosol mixture could become hygroscopic. The fine mode particles can be hydrophobic or hydroscopic, depending on their chemical compositions. In this case, there were no no clear evidence indicating the occurrence of hygroscopic growth or the mixing state of dust and pollution particles."

P8-9: Case 4: This dust case is ideal to compare all the numbers with the findings of Hofer et al. (2020) on lidar and depol ratios. See A10

Answer: The comparison to Hofer et al. 2020 has been added. Some sentenses referring to Hofer et al. 2020 have been added in Case 4.

Discussion: Again, please state clearly that the measurements are taken at a site rather close to a strong dust source so that giant particles have a strong impact on the measurements. This is not the case for almost all the observations published in the literature. After 1000 km travel most giant particles are gone, and the influence of fine dust on the optical properties increases. There is always fine-mode dust and coarse mode dust and giant-mode dust. Fine dust produces depolarization ratio below 20% at 532 and 1064 nm. Not only pollution aerosol can lead to a decrease of the depolarization ratio. See A11

Answer: Thank you for the suggestion. It is added in the manuscript.

P10, P286: I am a bit surprised that you did not mentioned the Hofer et al. papers in this context! Should be improved. It is good to have Table 3 for comparison and discussion. Please check Hofer 2020 (on lidar ratios and depol ratios) and include it here.

Answer: Hofer et al. 2020 (on lidar ratio and depolarization) has been included in Table 3. See A12

Figure 1: Kashi is at 39.47N and 75.98E, is the lidar field site really at 74.95 E as indicated in Figure 1? By the way, you could even include Dushanbe at 38.53N and 68.77 E in the map. see A13

Answer: As indicated in the manuscript, the observation site was located at 39.51N, 75.93E, which is in the northwest of the Kashi city. The orthogonal lines labeling longitude and latitude are not well aligned because the base map was in a 3D globe mode, not flat. To simplify the map (because there are already too many elements on the map), the author decided to remove the label of latitudes and longitudes. In addition, Dushanbe has been added on the map. Thanks to the reviewer's suggestion.

Figure 3: PM10 does not include the contribution by giant particles. Visibility observations (at the Kashi airport?) would be nice and conversion of the visibility-related extinction coefficients into mass concentrations…That would then clearly show the impact of giant particles.

Answer: we are agree that the PM10 data do not include giant particles with radius greater than 20 microns. The visibility data were for Kashi airport and data are public on the website: https://www.timeanddate.com/weather/china/kashgar/historic?month=4&year=2019
But we cannot assure the quality of the data and have no information about how these measurements were made. We referred the values of visibility to show that dust content was extremely high, but we do not use the visibility data for calculation.

Figure 6: (a) the height profiles of the extinction coefficients are fine and indicates large particles. But why is the 532 nm backscatter coefficient always larger than the 355 nm backscatter coefficient, even above the dust layer at heights above 4 km? I would assume that giant particles are not present anymore at such large heights, and clearly above the main dust layer. Please check the data analysis.

Answer: We have checked the data analysis, there is no sign showing a decrease versus height in the spectral dependency of backscattering coefficient between 355 and 532 nm. Moreover, the vertical variability of the PLDRs is also not very important. It indicates that particles were mixed well. This case on 09 April started from the morning of 08 April, very strong convection injected dust from the surface to the boundary layer. This event settled down in the night of 10 April. In the 3-day observations, we did not see any significant vertical variations of the backscatter-related Angstrom exponent and the PLDRs in the dust layer.

Figure 11 indicates similar air mass flow at all heights from 1000 to 3000 m.

Answer: Indeed, the back trajectory indicates the air mass at the three different levels are all originated from the same region, which is the west of the Taklamakan desert. From the UVAI maps, we can see that there were no evident dust activities during the overpass of the air mass. This explains the relatively low dust content, observed by the lidar. While the aerosol properties shown by the lidar profiles present distinct characteristics, showing features of pure dust in the lower boundary layer and polluted dust in the upper boundary layer. If we look into the trajectories of air mass when they are approaching the observation site, we can see that the air mass in upper boundary layer were lifted from near the surface in the urban region, while air mass in lower boundary layers were descending from the rural region. So, the air mass in upper boundary layer are more possible to mixed with some anthropogenic components. Moreover, air mass clustering in Figure 14 shows that, statistically, a nonnegligible proportion air mass at upper levels is originated from the long-distance west-to-east transport. This process may not be captured by a single back trajectory.

Figure 10: According to Fig.11 the extinction profiles and the 532 and 1064 nm backscatter and depolarization ratio profiles are fine. But I have always a bit my doubts concerning the 355 nm backscatter and depolarization ratio values. If the particle backscatter profile is a bit wrong in the case of 355 nm then the particle depol. Ratio will be wrong as well. The conversion from volume to particle depol ratio is very sensitive to the 355 nm backscatter values.

see A14

Answer: We agree that the errors in the backscattering coefficient will directly enter into the particle linear depolarization ratio. The error of PLDR is estimated accounting for the error of the backscatter coefficient, the volume depolarization ratio and the molecular depolarization ratio (Hu et al. 2019). And the error for PLDR at 355 nm is about 15% for dust cases (assuming 10% of error in the backscattering coefficient profile). An example is give below. We were also surprised when we found so high PLDR at 355 nm. But during the one-month observation, we found this value is very stable. Although the aerosol content changed, the mean PLDR at 355 nm varied 0.29—0.32 in dust from the Taklamakan desert. In addition, simultaneous cloud observations (in the night of 15-16 April 2019) showed that the PLDR at 355 nm for clouds at 9500-11500 m was in the range of 0.38-0.45, which are reasonable values. Therefore, we think this high PLDR at 355 nm is realistic and is resulted from the coarse-mode and giant particles in fresh dust.

Case 1:

Wavelength (nm)	R	VLDR	MDR	E_R	E_VLDR	E_MDR	PLDR	E_PLDR
355	2.6	0.19	0.015	10%	10%	200%	0.33	15%
532	9.80	0.31	0.020	10%	10%	300%	0.36	11%

Thanks to the reviewer for his/her helpful advice. We appreciate the reviewer's help and effort in reviewing this paper. The answers to the reviwers' are listed below.

General comments

This paper reports the lidar observations in Kashi, China located west of the Taklamakan Desert. The location is very interesting, and the quality of the observations with a multi-wavelength Raman lidar looks high, and consequently the results merit publication. However, the discussion on dust characterization in the present manuscript is only conceptual and very ambiguous. No strong conclusions are obtained. The authors discuss polluted dust cases, but the definition of polluted dust is not clear. The location of the observation is relatively clean except for desert dust. Is the polluted dust a mixture with anthropogenic air pollution? Is it external mixture or internal mixture? Probably, it would not be possible to characterize it only with lidar data.

Answer: We have to admit that, with lidar measurements, we are not able to provide further information to tell the exact species of the pollutants nor the mixing state of dust and pollution, although they are very important information. To obtain such information and to get "strong conclusion", in-situ measurements are required.

According to long-term observations in <Li et al. 2018: Comprehensive study of optical, physical, chemical, and radiative properties of total columnar atmospheric aerosols over China: an overview of sun--sky radiometer observation network (SONET) measurements> and Figure 2, the role of anthropogenic aerosol is not negligible, so Kashi cannot be simply regarded as a 'clean site'. Kashi is a populated city in Xinjiang (see the figure below, referring to <Doxsey-Whitfield, Erin, et al. "Taking advantage of the improved availability of census data: a first look at the gridded population of the world, version 4." Papers in Applied Geography 1.3 (2015): 226-234.>), anthropogenic emission should be reasonably expected to occur. As to the mixing state, it is out of the scope of this paper and beyond what we can obtain on the basis of what we have.

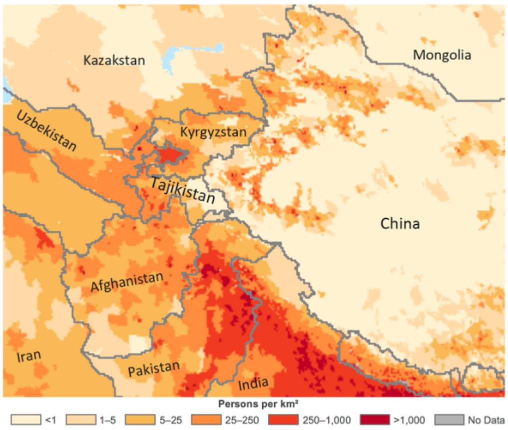

Variability of the characteristics of "pure" dust is not well understood. Also, optical parameters are dependent on particle size distribution even if the composition is the same. The manuscript should be rewritten, in my opinion, with more focus on detailed comparison of the observed parameters (lidar ratio, particle depolarization ratio, Angstrom exponents) with previously reported results. The discussion with Table 3 in the present manuscript is not sufficient. Discussion on the change in optical characteristics by mixing with pollution should be given, if “polluted dust” is discussed. see B1

Answer: The definition of ‘pure dust’ is given in the beginning of the ‘Discussion’ section. In this paper, the ‘pure’ Taklamakan dust is defined with PLDR >0.32 at 532 nm and the EAE(355-532) smaller than 0.1. The identification of Taklamakan dust is also confirmed with back trajectory. The definition of polluted dust is “PLDR <0.3 at 532 nm and EAE >0.2”. Again, back trajectory is used to support the identification. We agree that the optical properties are dependent on not only the composition but also the size distribution. For example, dust aerosol with different fraction of fine dust could present different optical properties, such as BAE, PLDR… This issue is added in the manuscript and the discussion part is improved.

Detailed comments

Line 19: T yr-1 -> Tg yr-1 **see B2**

Answer: Corrected.

Line 28-35: The authors should describe how the lidar data can be used as input and validation of models. see B3

Answer: A common way of involving lidar data into models is to simulate lidar profiles (of lidar signal, backscatter coefficient profile, extinction profile or depolarization profile) with the output or description of models for a model-given atmospheric state. For example, Sekiyama et al. 2010 assimilated the backscatter coefficient and depolarization profiles of CALIPSO Level 1B data. In the model, the backscatter coefficient equals to the sum of backscatter coefficients of several aerosol component, such as sulfate, sea-salt and dust, whose concentrations are model prognostic variables. Zhang et al. 2011 and Campbell et al. 2010 chose to deal with the extinction coefficient of CALIPSO in mass transport model. Apart from satellite lidar, modelers also used ground-based lidar measurements as input of models. Wang et al. 2013 used AirBase lidar network data to simulate PM10 concentrations. As to model validation, it mostly depends on the output of models and the variables to be validated. In Yu et al. 2010, both vertical profiles, e.x. extinction profile, and integrated variable, e.x. AOD from CALIPSO are used to validate the GOCART model. However, the authors consider this detailed information is not so relevant to the topic of our paper. So, a brief description and a list of references given in the manuscript will be sufficient.

Line 75-77 “Moreover, there are populated cities in the neighboring countries such as Kyrgyzstan, Tajikistan and Pakistan. Under favorable meteorological conditions, various aerosol, for example, pollution, could be potentially transported to Kashi and mix with dust aerosols. “: This statement is not convincing, looking at the map. see B4

Answer: In Figure 14, the air mass clustering indicates that the air mass arriving at the observation site may be originated from Kyrgyzstan, Tajikistan, Afghanistan… The air mass coming from Pakistan are not seen by the back trajectory, so we decide to exclude it from the manuscript.

Line 96-98: To my knowledge, the error analysis cannot be this simple. The error in extinction must be different from that in backscatter. Also, the error must be dependent on height and the background radiation. It should be mentioned that the Raman lidar measurement was limited in the nighttime, if so. In addition, it would be better to have some descriptions about the advantage of using rotational Raman instead of vibrational Raman at 532 nm. **see B5**

Answer: A sentence presenting the advantage of rotational Raman channel has been added and one reference paper has been given. That measurements were made in nighttime has been added in the manuscript. The error estimate is presented in the appendix <Hu et al. 2019: Long-range-transported Canadian smoke plumes in the lower stratosphere over northern France>, so it is not repeated in this paper. The error is height dependent but here we selected typical values at a certain vertical level, calculated the error and then apply it to all the vertical levels. The 15% of error is a conservative value derived with 10% of error in the backscattering coefficient, volume depolarization ratio and 200-300% in the molecular depolarization ratio. We re-calculated the error more carefully and find that in some cases, the error at 355 nm exceeds 15%, for example, Case 3. The errors in the upper layer and lower in Case 3 and 4 are calculated separately. Two examples of the calculated errors are shown in the following tables:

Case 1:

Wavelength (nm)	R	VLDR	MDR	E_R	E_VLDR	E_MDR	PLDR	E_PLDR
355	2.6	0.19	0.015	10%	10%	200%	0.33	15%
532	9.80	0.31	0.020	10%	10%	300%	0.36	11%

Case 3:

Wavelength (nm)	R	VLDR	MDR	E_R	E_VLDR	E_MDR	PLDR	E_PLDR	
355	1.7	0.83	0.015	10%	10%	200%	0.21	21%	Upper layer
532	2.88	0.16	0.010	10%	10%	200%	0.24	13%	
1064	10.0	0.23	0.020	20%	10%	300%	0.26	11%	
355	1.64	0.11	0.015	10%	10%	200%	0.30	24%	Lower layer
532	4.58	0.25	0.010	10%	10%	200%	0.34	12%	
1064	28.0	0.30	0.012	20%	10%	300%	0.31	10%	

Figure 3: The periods of Case1, 2, 3 and 4 should be indicated in Figure 3.
Answer: Corrected. **see B6**

Figure 5: Case1, 2, 3 and 4 should be indicated in Figure 5. **see B7**
Answer: They were indicated in the caption of Figure 5, so we think it is not necessary to be indicated on the figure.

Figure 3: Legend “500 nm” should be AOD (500 nm).

see B6

Answer: Corrected.

Line 166-168: The backscatter coefficient at 1064 nm below 1800 m should be indicated in Fig. 6.

Answer: On 09 April 2019, the aerosol content was very high, so the signal at 1064 nm is not useable because of signal distortion. This is the reason why it was not plotted in Figure 6. The explanation has been given in the manuscript.

Line 169-170: "EAE" and "BAE" are not defined. **see B8 and B1**

Answer: Thanks. It has been corrected.

Line 183-187: Is the description consistent with Figure 3?

L182-187: "… limit of the sun/sky photometer, so the AERONET and SONET retrieval can not be applied. A large and intense plume was first detected in the morning of 23 April 2019 (Figure 4). And on 24 April, a hot spot of UVAI appeared over the observation site. The daily average of AOD is 3.63 and Ångström exponent is about -0.01, according to the daytime sun/sky photometer measurements… "

Answer: Yes, it is consistent. I am not sure what inconsistencies you have observed in this paragraph. I guess maybe you mean the values of AOD and AE? The values we mentioned in this paragraph are daily averaged values, not the instantaneous values in Figure 3. If you were wondering why we say "an intense plume was detected on 23 April", but that was not reflected by Figure 3, the answer is that this plume was not over our observation site. I hope I got your question.

Line 227-228: What is the "clear evidence of polluted dust"? **see B9**

Answer: It is the decrease of PLDRs and increase of EAE, which indicates the occurrence of fine particles and particles with more spherical shapes. The increase of BAE also corroborates that aerosols above 2200 m are not the same with those below 2000 m. You might want to point out that pollution may not be the only cause, the deposition of coarse-mode and giant particles could also lead to this effect. We agree, the manuscript has been improved with taking into account this issue.

Line 229-232: The structure at around 2500 m is interesting and should be studied further. Is the type of dust (or "polluted" dust) the same in 1000-2200 m and 2400-2800 m or different? Why relative humidity was high in 2400-2800 m? **see B9**

Answer: They are different aerosol types since signatures in PLDR, EAE and BAE are different. The WVMR is also a tracer of air mass. The relatively higher WVMR or RH at 2400-2800 m indicates that the air mass at 2400-2800 m could have different origins with the air mass at lower altitudes. This is one reason why we supposed it is polluted dust. But the increase of WVMR is not significant enough to confirm that they are definitively different air mass.

Figure 9: Captions for (c) and (d) **see B10**

Answer: The caption has been complemented.

The characterization of Taklamakan dust properties using a multi-wavelength Raman polarization lidar in Kashi, China

Qiaoyun Hu[1], Haofei Wang[2,4,5], Philippe Goloub[1], Zhengqiang Li[2], Igor Veselovskii[3], Thierry Podvin[1], Kaitao Li[2], and Mikhail Korensky[3]

[1]Univ. Lille, CNRS, UMR 8518 - LOA - Laboratoire d'Optique Atmosphérique, F-59000 Lille, France
[2]State Environmental Protection Key Laboratory of Satellite Remote Sensing, Aerospace Information Research Institute, Chinese Academy of Sciences, Beijing, China
[3]Physics Instrumentation Center of General Physics Institute, Troitsk, Moscow, 142190, Russia
[4]University of Chinese Academy of Sciences, Beijing, 100101, China
[5]Key Laboratory of Radiometric Calibration and Validation for Environmental Satellites, National Satellite Meteorology Center, Beijing, 100081, China

Correspondence: Haofei Wang (wanghf@radi.ac.cn)

A1 **Abstract.** The Taklamakan desert is an important dust source for the global atmospheric dust budget and a cause of the dust weather in Eastern Asia. The characterization of Taklamakan dust in the source region is still very limited. To fill this gap, the DAO (Dust Aerosol Observation) was conducted in April 2019 in Kashi, China. Kashi site is about 150 km to the west rim of the Taklamakan desert and is strongly impacted by desert dust aerosols, especially in spring time, i.e. April and May. According to sun/sky photometer measurements, the aerosol optical depth (at 500 nm) varies in the range of 0.07–4.70 and the Ångström Exponent (between 440 and 870 nm) varies in the range of 0.0–0.8 in April 2019. In this study, we provide the first profiling of the $2\alpha+3\beta+3\delta$ parameters of Taklamakan dust based on a multi-wavelength Mie-Raman polarization lidar. For Taklamakan dust, the Ångström Exponent related to extinction coefficient (EAE, between 355 and 532 nm) is about 0.01±0.30, and the lidar ratio is found to be 45±7 (51±8–56±8) sr at 532 (355) nm. The particle linear depolarization ratios (PLDRs) are about 0.28–0.32±0.07 at 355 nm, 0.36±0.05 at 532 nm and 0.31±0.05 at 1064 nm. Both lidar ratios and depolarization ratios are higher than the typical values of Central Asia dust in the literature. The difference is probably linked to the fact that observations in the DAO campaign were collected close to the dust source, therefore, there is a large fraction of coarse-mode and giant particles in the Taklamakan dust. Apart from dust, fine particles coming from local anthropogenic emissions and long-range transported aerosols are also non-negligible aerosol components. The signatures of pollution emerge when dust concentration decreases. The polluted dust (defined by $\mathrm{PLDR}_{532} \leq 0.30$ and $\mathrm{EAE}_{355-532} \geq 0.20$) is featured with reduced PLDRs and enhanced $\mathrm{EAE}_{355-532}$ compared with Taklamakan dust. The mean PLDRs of polluted dust generally distributed in the range of 0.20–0.30. Due to the complexity of the nature of the involved pollutants and their mixing state with dust, the lidar ratios exhibit larger variabilities compared with dust. The study provides the first reference of novel characteristics of Taklamakan dust measured by Mie-Raman polarization lidar. The data could contribute to complementing the dust model and improving the accuracy of climate modeling.

1 Introduction

B2

Airborne dust is the most abundant aerosol species and accounts for nearly 35% of the total aerosol mass in the atmosphere (Boucher et al., 2013), with an annual flux of 1000–5000 Tg per year (Engelstaedter et al., 2006; Textor et al., 2006; Huneeus et al., 2011). According to the estimation of Ginoux et al. (2012), about 75% of the atmospheric dust is originated from natural emission and anthropogenic dust emission accounts for ∼25%. The area spreading from the Sahara desert, the Arabian Peninsula, Central Asia to East Asia is the most significant natural dust source. Based on model simulations, Tanaka and Chiba (2006) estimated that the Saharan desert contributes to ∼62% of the total dust emission and the contribution of Arabian Peninsula, Central Asia and East Asia is about half of the Saharan emission. The dust sources in North and South America, and Australia altogether account for about 25% of total emission. The suspending dust particles can directly influence the planetary radiation budget, and indirectly impact the climate through interfering with cloud properties and cloud process. Dust particles, as well as other ice nucleating particles (INP), can aide the formation of ice crystals in the heterogeneous ice nucleation regime. A2 Due to their effective ice nucleating capability and abundant concentration, mineral dust particles are considered as the most important INP (Kanji et al., 2017). Recent studies found that atmospheric dust is also linked to the activity of tropical cyclones and rainfall (Reed et al., 2019; Thompson et al., 2019).

A comprehensive dataset of dust properties is of significant importance for understanding the effects of dust in the eco-system and for reducing the uncertainties of climate model. However, this task is very challenging and needs the support of observational data. The properties of dust particles are determined by the texture of soils, the mineralogical compositions, vegetation cover and surface properties, which could vary globally from location to location. The modeling of dust horizontal and vertical distribution, and dust cycle, i.e. dust emission, transport and deposition, is crucial to climatic modeling. So far, the vertically resolved information can only be obtained from lidar (Light detection and ranging) measurements. A multi-wavelength Mie-Raman polarization aerosol lidar can obtain multiple parameters at a vertical level. This capability makes it a useful tool for aerosol study. The profiles of backscatter coefficient, extinction coefficient and depolarization ratio derived from satellite lidar and ground-based lidars have been used as model inputs and have been proved useful for improving the accuracy of model simulation and forecasting (Yumimoto et al., 2008; Campbell et al., 2010; Sekiyama et al., 2010; Wang et al., 2013; Zhang et al., 2011, 2012). B3

In Asia, dust sources distribute over a large area and cover different terrain types. The high-elevated bare lands in Iran, Afghanistan and Tajikistan, and the Taklamakan desert in the Tarim basin, the Loess plateau and the Gobi desert in China are the main dust sources. In addition, excessive land-use and human activities formed new dust sources. There are a good number of publications reporting transported Asian dust observed in the downwind countries in East Asian (Liu et al., 2002; Murayama et al., 2004; Huang et al., 2008; Iwasaka et al., 2008). Long-range transported dust can cross the Pacific ocean and occasionally reach America (VanCuren and Cahill, 2002; Uno et al., 2009). However, very few field campaigns have been carried out for Asian dust study. Compared with Saharan dust, the characteristics of Asian dust were not adequately explored. The earliest field campaign characterizing Asian dust date back to 1989, when an experiment was carried out in Tajikistan for studying desert dust properties and the impact on meteorological conditions. The CADEX (Central Asian Dust EXperiment) project was planned to provide a data set of optical and microphysical properties of dust from Central Asia. A multi-wavelength Mie-Raman polarization lidar was deployed in Dushanbe, Tajikistan. This results in Hofer et al. (2017) and Hofer et al. (2020) A3 provided important dust properties, such as vertically resolved lidar ratios, linear depolarization ratios and mass concentrations. In 2002 and 2009, a elastic polarization lidar system (without Raman channel) was set up in Aksu (40.62°N, 80.83°E, in Xinjiang, China) near the north rim of Taklamakan desert (Kai et al., 2008; Jin et al., 2010). Jin et al. (2010) obtained the first lidar ratio of the Taklamakan dust in the source region, however, it requires extra assumptions and supplementary measurements. Sparse lidar observations in the downwind of transported Taklamakan dust have been reported but none of them provides intensive dust characteristics and the observation sites are far from the desert.

In 2019, the DAO (Dust Aerosol Observation) campaign was conducted in April to June in China. This campaign was supported by the "Belt and Road Initiative" and involved researchers from China, France and Russia. The first observation site in the DAO campaign is in Kashi (also called Kashgar) in April 2019, which is about 150 km to the western rim of the Taklamakan desert. The objective of the first session of DAO campaign is to study the characteristics of Taklamakan dust. The second session of the campaign was in Beijing in May and June, for investigating the impact of transported dust on the air quality in megacity. The main topic of this paper is the characterization of Taklamakan dust, therefore, only the measurements in Kashi will be analyzed. This study is organized into 5 sections. The description of DAO campaign is presented in Section 2, and the results and case study is in Section 3. The discussions and conclusions are presented in Section 4 and 5, respectively.

2 The DAO (Dust Aerosol Observation) campaign

2.1 Overview

The Taklamakan desert is located in the center of the Tarim Basin in the Uygur Autonomous Region of Xinjiang, China, covering an area of about 320,000 km^2. The mean elevation of the Taklamakan desert is about 1200–1500 m a.s.l (Petrov and S.Alitto, 2019). It is surrounded in three directions by high mountain ranges (see Figure 1). The observation site (39.51°N, 75.93°E, time zone: GMT+08:00) is in the northwest of the Kashi city and close to the border to Tajikistan, Kyrgyzstan and Afghanistan. Kashi features a desert climate with a big temperature difference between winter and summer. The coldest month is January with average temperature of -10.2–0.3°C and the warmest month is in July with average temperature of 18.6–32.1°C. The annual rainfall in Kashi is about 64 mm. The spring in Kashi is long and comes quickly. The rapidly heated surface sand in the desert could generate ascending currents which could result in frequent dust storm in springtime. This is the main reason that the field campaign was performed in springtime.

Except for desert dust, anthropogenic emission is another important aerosol source. There are about 4.65 million habitants (predicted for 2017, see the link) in the Kashi prefecture, including the Kashi city and 11 subordinate counties. Kashi prefecture is a very populated region in Xinjiang with more than 1000 persons per square kilometer in the city center (Doxsey-Whitfield et al., 2015). Fine aerosol particles originated from biomass burning and local anthropogenic emissions, such as heating, traffic and industrial pollution are an important aerosol component. Moreover, there are populated cities in the neighboring countries such as Kyrgyzstan and Tajikistan. Under favorable meteorological conditions, various aerosols, for example, pollution, could be potentially transported to Kashi and mix with dust aerosols. B4

2.2 Instrumentation and methodology

Lidar system

The multi-wavelength Mie-Raman polarization lidar called LILAS (Lille Lidar Atmosphere Study) is the main instrument installed in observation site. The lidar system has been operated in LOA (Laboratoire d'Optique Atmosphérique, Lille, France) since 2013 (Bovchaliuk et al., 2016; Veselovskii et al., 2016; Hu et al., 2019). During the DAO campaign, LILAS was transported from Lille to Kashi (and Beijing in the second session of the campaign) to perform observations. LILAS uses a Nd: YAG laser that emits at three wavelengths: 355, 532 and 1064 nm. The laser repetition rate is 20 Hz. A Glan prism is used to clean the polarization of the laser beam. The emitting power after the Glan prism is about 70, 90 and 100 mJ at 355, 532 and 1064 nm, respectively. LILAS system has three Raman channels, including 387 (vibrational-rotational), 530 (rotational) and 408 nm (water vapor). The use of rotational Raman at 530 nm provides a stronger Raman signal and relieves the dependence of the derived extinction and backscatter coefficients on the assumption of Ångström exponent (Veselovskii et al., 2015). B5 The backscattered light is collected by a 400 mm Newton telescope. The incomplete overlap range of LILAS system is about 1000–1500 m in distance, depending on the selected field of view angle. In the receiving optics, the three elastic channels are equipped with both a perpendicular and a parallel channel with respect to the polarization plane of the emitted linearly polarized laser light, in order to measure the linear depolarization ratio at three wavelengths. LILAS can provide the profiles of the $2\alpha+3\beta+3\delta$ (α: extinction coefficient, β: backscatter coefficient, δ: particle linear depolarization ratio (PLDR)) parameters. Benefited from the coupled Raman channels, the extinction and backscatter coefficients at 355 and 532 nm are calculated using the Raman method proposed by Ansmann et al. (1992). The Raman signal generated by the radiation at 1064 nm is not measured by LILAS, thereby Raman method is not applicable. The backscatter coefficient at 1064 nm is calculated using the Klett method, where a vertically constant lidar ratio (extinction-to-backscatter ratio) is assumed (Klett, 1985). The particle linear depolarization ratios are derived from Equation 1: A4

$$\delta^p = \frac{(1+\delta^m)\delta^v R - (1+\delta^v)\delta^m}{(1+\delta^m)R - (1+\delta^v)}, \qquad (1)$$

where R represents the ratio of the total backscatter coefficient, involving molecules and particles, to the particle backscatter coefficient. δ^m represents the molecular depolarization ratio. δ^v represents the volume linear depolarization ratio (VLDR), which equals to the calibration coefficient multiplied by the ratio of the signal of the perpendicular channel to the parallel channel. The polarization calibration is performed following the ±45° method (Freudenthaler et al., 2009). During the DAO campaign, the polarization calibration has been performed at least once per day.

The Ångström exponent of the extinction coefficient and backscatter coefficient are calculated by the Equation 2:

$$\mathring{A} = -\frac{\log p(\lambda_1) - \log p(\lambda_2)}{\log \lambda_1 - \log \lambda_2} \qquad (2)$$

where $p(\lambda)$ represents the optical parameters, such as AOD, extinction or backscatter coefficient at wavelength λ, $\mathring{A}$ represents the Ångström exponent of the corresponding parameters $p(\lambda)$. The statistical error of lidar derived parameters is estimated using the method presented in Hu et al. (2019). The data presented in this study are recorded in nighttime, so the background radiation is negligible. The error in the extinction and backscatter coefficient is about 10%, which leads to about 15% of error in the lidar ratios, at 355 and 532 nm. The error in the backscatter coefficient at 1064 nm is about 20%. The error in PLDR is calculated in terms of the backscatter ratio, VLDR and molecular depolarization ratio. For the data presented in this study, the error in PLDR is no greater than 15% at 532 and 1064 nm. Therefore, we conservatively use 15% as the error in PLDR for 532 and 1064 nm. At 355 nm, the error of 15% still holds when dust concentration is high enough, but when the concentration drops, the error could exceed 15%. In the case study, errors at 355 nm are calculated separately. The errors for the water vapor mixing ratio (WVMR) and relative humidity (RH) are about 20%.

B5

Sun/sky photometer

Three sun/sky photometers are deployed in the Kashi observation site. One is affiliated to the AERONET (AErosol RObotic NETwork, Holben et al. (1998)) network and the other two are affiliated to SONET (Sun-Sky Radiometer Observation Network). SONET is a ground-based sun/photometer network with the extension of multi-wavelength polarization measurement capability to provide long-term columnar atmospheric aerosol properties over China (Li et al., 2018). The three sun/sky photometers provide complementary measurements by following different measurement protocols. In all, they can measure daytime aerosol optical depth (denoted as AOD hereafter) at 340, 380, 440, 675, 870, 1020 and 1640 nm, polarized/unpolarized sky radiances at 440, 675, 870 and 1020 nm and moon AOD as well. The succeeding data treatment and retrieval are performed following the protocols and standards of AERONET or SONET, depending on the affiliation of the instruments.

Satellite data

Satellite data have complementary advantages due to their large spatial coverage compared with ground-based remote sensing technique. In order to monitor dust activities of the Taklamakan desert, we use the UV aerosol index (UVAI hereafter) derived from the OMPS (Ozone Mapping Profiler Suite) onboard the Suomi-NPP (National Polar-orbiting Partnership) satellite (Flynn et al., 2004; Seftor et al., 2014). OMPS provides full daily coverage data and the overpass time for Kashi region is around 06:30 UTC. The UVAI is calculated using the signal in the 340 and 380 nm channels (Hsu et al., 1999):

$$\mathrm{UVAI} = -100 \times \left\{ \log_{10}\left[\frac{I_{340}}{I_{380}}\right]_{meas} - \log_{10}\left[\frac{I_{340}}{I_{380}}\right]_{calc} \right\}, \tag{3}$$

A5

where I_{340} and I_{380} represent the backscattered radiance at 340 and 380 nm. The subscripts "meas" and "calc" respectively represent the real measurements and model simulation in a pure Rayleigh atmosphere. By the definition of UVAI, its positive values correspond to UV-absorptive aerosols such as desert dust and carbonaceous aerosols. Hence, the UVAI from OMPS is a good parameter for monitoring the activity of the Taklamakan desert.

Auxiliary data

A radiosonde station (39.47°N, 75.99°N) in Kashi is 6 km to the observation site. The data are accessible on the website of the Wyoming weather data website (see the link). The radio sounding data are recorded at 00:00 and 12:00 every day at local time.

They provide the vertical temperature and pressure profiles for the calculation of molecule scattering parameters in lidar data processing. The HYSPLIT (Hybrid Single-Particle Lagrangian Integrated Trajectory, Stein et al. (2015); Rolph et al. (2017)) model developed by the National Oceanic and Atmospheric Administration (NOAA) Air Resources Laboratory is used for the back trajectory of the air mass and for the air mass clustering. The HYSPLIT model is driven by the 0.5° gridded GDAS (Global Data Assimilation System) data and could produce the transport pathways of the air mass at different vertical levels. Besides, instruments measuring particulate matter (PM10 and PM2.5), gas concentration (SO2, O3 and NOx), particle size distribution, particle scattering and absorption coefficients, solar radiation and a cloud monitor are also deployed in the field campaign. These data contribute to relevant air quality and solar radiation studies within the frame of the DAO campaign.

3 Results and analysis

3.1 Overview

Figure 2 presents the monthly averaged AOD at 500 nm, Ångström exponent between 440 and 870 nm and the FMF (fine mode fraction, the fraction of fine mode AOD to total AOD) in Kashi site from 2013 to 2017. The data are derived from SONET network. The highest AOD occurs in spring, i.e. March and April, while the lowest values occur in summer time, i.e. June and July. The Ångström exponent is positively correlated to the FMF and negatively correlated to the AOD. The lowest mean Ångstöm exponent occurs in March and April, indicating that dust particles are dominant due to the seasonal increase of dust activities in this period (Littmann, 1991; Qian et al., 2002). In December and January, the Ångström exponent and FMF increase significantly, which proves that fine particles are an important aerosol component in winter.

Figure 3(a) plots the AOD at 500 nm and the Ångström exponent measured during the DAO campaign in April 2019. The AOD varies from 0.07 to 4.70 and the Ångström exponent varies from 0.0 to 0.8. For AOD greater than 0.2, the corresponding Ångström exponent mostly falls into the range of 0.0 to 0.2. While for AOD lower than 0.2, the Ångström exponent is mostly between 0.3 to 0.7. The negative correlation between the AOD and the Ångström exponent indicates that coarse particles are the main cause for the increase of AOD. This argument is supported by the variation of the particulate matter plotted in Figure 3(b).

We select four representative cases from the nearly 1 month lidar observations. The four cases are recorded on 03, 09, 15 and 24 April 2019. In order to distinguish "pure" Taklamakan dust observations, we define Taklamakan dust by EAE$_{355-532}$ (Ångström exponent related to extinction coefficient) smaller than 0.1 and PLDR$_{532}$ greater than 0.32 at 532 nm. Polluted dust **B1** is defined with PLDR smaller than 0.30 at 532 nm and EAE no smaller than 0.2. Back trajectories are also used as a reference for identifying the aerosol origins. The maps of UVAI are plotted in Figure 4. On 09 and 24 April, intense aerosol plumes were observed over the Taklamakan desert. One extreme dust event occurred on 24 April when the AOD (at 500 nm) reached about 4.70 at 08:40 UTC, with instantaneous Ångström exponent about -0.02 and the visibility about 1 km (see the link). The PM10 increased to the monthly maximum on 24 April, reaching nearly 1500 μg/m^3. It should be noted that, in this extreme case where AOD reached 4.70, the accuracy of the measured AOD may degrade because of the decreasing signal-to-noise ratio. Moreover, weak incoming solar radiation might disturb the performance of the cloud screening in the quality control

A6

procedure, thus disabling the discrimination of cloud contaminated and non-contaminated measurements. On 03 and 15 April, the activity of the Taklamakan desert became less intense compared with the first two cases. The concentration of dust particles decreased and the features of polluted dust appeared. Lidar quicklooks at 532 nm for the four cases are plotted in Figure 5.

3.2 Case studies

3.2.1 Case 1: 09 April 2019

Dust plumes over the Taklamakan desert are detected on 07, 08 and 09 April, as shown in Figure 4. The most intense plume in the three days appeared on 07 April, with maximum UVAI about 4.0. On 09 April, a belt-like plume appeared in the north and northwest of the desert. Figure 5(b) shows the range-corrected lidar signal at 532 nm collected between 9 and 10 April. The boundary layer height slightly increases from 3000 m to 4000 m in the night, and strong backscattered lidar signal is seen below 2000 m. Figure 6 shows the profiles of the optical properties, WVMR and RH averaged between 17:00 and 22:00 UTC, 09 April 2019. The extinction coefficients gradually decrease with height. At 1000 m, the extinction coefficients are greater than 0.5 km^{-1} and remain almost stable below 2000 m. The RH is no more than 40±8% below 2000 m and rises to 60±12% at 3800 m. The lidar ratio varies between 40±6 and 48±7 sr at 532 nm and between 55±8 and 62±9 sr at 355 nm. The PLDR is about 0.32±0.05 at 355 nm and 0.36±0.05 at 532 nm. The VLDR at 1064 nm is about 0.32±0.03. The backscatter coefficient, as well as the PLDR at 1064 nm is not available above 1800 m, since the1064 nm lidar signal has distorted in upper boundary layer. We can expect that the VLDR is approximate to PLDR at 1064 nm under in this case, because the dust content is so high that molecular scattering at 1064 nm can be neglected. The EAE$_{355-532}$ is about -0.10±0.30 at 800 m and rises to 0.10±0.30 at 3800 m. The BAE$_{355-532}$ (Ångström exponent related to backscatter coefficient) is negative and varies from -0.7±0.3 to -0.4±0.3. Below 3000 m, the lidar ratios mildly decrease with height, while the PLDRs do not show obvious vertical variations. Above 3000 m, the vertical variations in the lidar ratios and PLDRs become more significant. The vertical variations of the lidar ratios and PLDRs are possibly the result of particle sedimentation or/and vertically dependent particle origins.

B8

On 09 April, the Taklamakan desert was covered by a low-pressure zone with easterly and northeasterly wind prevailing over the western part of the desert. It is a favorable condition for the elevation of dust particles. Figure 7 shows the 48-hour back trajectory ending at 20:00 UTC for air mass at 1000, 2000 and 3000 m. The air masses at the three vertical levels are originated from the Taklamakan desert. They all passed over the area where dust plumes have been observed and then diverged when approaching the rim of the desert. In the end, the air masses at 1000, 2000 and 3000 m arrived at the observation site from the northeast, east and southeast respectively. The particles observed by LILAS on 09 April are fresh desert dust, without long-range transport. Therefore, they could contain a large fraction of coarse-mode particles especially giant particles (radius> 20 μm). Moreover, the back trajectories in Figure 7 shows convective strong air flows arising from below 500 m to 3000 m within 3 hours, suggesting the possibility of lifting large particles near the surface to higher levels.

A7

3.2.2 Case 2: 24 April 2019

On 24 April, the observation site was enclosed by floating dust. In the daytime, the sky radiance dropped below the detection limit of the sun/sky photometer, so the AERONET and SONET retrieval can not be applied. A large and intense plume was first detected in the morning of 23 April 2019 (Figure 4). On 24 April, a hot spot of UVAI appeared over the observation site. The daily average of AOD is 3.63 and Ångström exponent is about -0.01, according to the daytime sun/sky photometer measurements. The lidar quicklook on 24 April in Figure 5 shows that the boundary layer height rises from about 1200 m to 2000 m from 14:00 to 24:00 UTC. Due to the high dust attenuation in the boundary layer, both sun/sky photometer and lidar cannot detect whether clouds exist on 24 April. Figure 8 plots the averaged parameters between 15:00–24:00 UTC, 24 April 2019. The dust layer was so thick that the laser beam can not penetrate. The amplitude of Raman signal dropped by 5–6 orders in the lower 2000 m. In this condition, we can not find an aerosol-free zone to for the calibration of lidar signal, therefore, the calculation of the backscatter coefficient using Raman method is not possible. But the extinction coefficient can be derived from the Raman signal (Ansmann et al., 1992). The extinction coefficients are 1.0 ± 0.1 km^{-1} at 800 m and increases to about 1.5 ± 0.2 km $^{-1}$ at 1500 m. The extinction coefficient at 355 nm is removed at above 1500 m because it starts to oscillate due to insufficient signal-to-noise ratio. The extinction coefficient at 532 nm decreases to about 1.1 ± 0.1 km^{-1} at 2000 m. By assuming that the lidar ratios are about 55 sr and 45 sr at 355 and 532 nm, respectively, we obtain the backscatter coefficient from the extinction coefficient, and then calculate the PLDRs (in Figure 8(c)). The PLDR is about 0.32 at 355 nm and 0.37 at 532 nm, which are rather consistent with the results in Case 1. The uncertainties of the PLDRs are not accessible because the uncertainties of the assumption of lidar ratio are not known.

The back trajectories (not shown) indicates that dust particles (at 1000 and 2000 m) are originated from the northeast and east, where intense dust plumes were observed on 23 and 24 April. Figure 9 shows synoptic conditions at 00:00 UTC, 23 April and 06:00 UTC, 24 April. The meteorological conditions on 23 and 24 April are favorable for dust emission, similar to Case 1. The Taklamakan desert is enclosed by a low-pressure zone (Figs. 9(a) and (c)). The plume observed by OMPS on 23 April was probably lofted in the local morning. In the eastern part of the Taklamakan desert, 37–39°N, 83–88°E, the wind velocity at 10 m (a.g.l) reaches more than 50 km/h (Figure. 9(a)) and at 850 hPa level the maximum wind velocity reaches 90 km/h (Figure. 9(b)). The high wind velocity near the surface and large vertical wind gradient help elevate dust particles from the surface into the atmosphere. On 23 and 24 April, easterly and northeasterly wind are prevailing in the desert region, thus blowing the lifted dust particles to the observation site. Case 2 is a more severe manifestation of Case 1 regarding the intensity of the dust loading. In both cases, the observed dust particles are originated from nearby dust source. Compared with typical depolarization ratios in worldwide dust observations, which are 0.23-0.30 at 355 nm and 0.30-0.35 at 532 nm, the depolarization ratios we obtained in the two cases are relatively higher (Veselovskii et al., 2016; Freudenthaler et al., 2009; Hofer et al., 2017, 2020). While previous observation sites were mostly not as close to the dust source as in our campaign, the differences are probably due to the fraction of coarse-mode particles that remain in our dust observation. Burton et al. (2015) also observed dust particles near the source in North America and reported PLDR of 0.37 at 532 nm, which is consistent with our result. However, the PLDR at 355 nm measured by Burton et al. (2015) is about 0.24, lower than what we obtained.

A8

3.2.3 Case 3: 15 April 2019

On 15 April, the daily mean AOD on 15 April was 0.63 and the Ångström exponent was about 0.10. Compared with the previous two cases, the Ångström exponent increase obviously. The boundary layer height started to increase at 15:00 UTC and stayed at 3500 m in the night of 15 April. Cirrus clouds were continuously present during the period of lidar measurement (Figure 5(c)). The lidar derived profiles between 18:00–20:00 UTC are plotted in Figure 10. The extinction coefficients in the boundary layer are about 0.15 km^{-1} and decrease to almost zero at 3500 m. The RH increases up to 60±12% at 2200 m. Below this height, the lidar ratio, PLDR, EAE and BAE are almost stable. The lidar ratio is about 51±8 sr at 355 nm and 45±7 sr at 532 nm. The PLDRs at 355, 532 and 1064 nm are around 0.32±0.07, 0.34±0.05 and 0.31±0.05, respectively. The $EAE_{355-532}$ is about 0.02±0.30, showing a gentle increase with height, and the $BAE_{355-532}$ is about -0.29±0.30. Above 2200 m, the RH starts to increase and reaches its maximum, i.e. 80±16%, at 2800 m. The $EAE_{355-532}$ and $BAE_{355-532}$ increase to 0.10±0.30 and -0.06±0.30, respectively. On contrary, the lidar ratios and PLDRs decrease and reach their minima at about 2800 m. The lidar ratio is about 40±6 sr at 2400–2800 m, with a weak spectral dependence, and the PLDRs are about 0.23±0.06 at 355 nm, 0.26±0.04 at 532 nm and 0.24±0.03 at 1064 nm. It should be noticed that the backscatter coefficient at 1064 nm is performed using Klett method with an assumption of lidar ratio equal to 40 sr (Klett, 1985).

Dust activities were observed by the OMPS on 13 and 15 April 2019 (Figure 4), while the intensity was less stronger than in Case 1 and 2 and the distance between the dust plume and the observation site is farther. The 48-hour back trajectories ending at 19:00 UTC are shown in Figure 11. Air masses at the three vertical levels (1000, 2000 and 3000 m) are originated from the eastern part of the Taklamakan desert, where no intense dust activities have been observed by OMPS in the recent three days. It explains the decrease of dust content in the boundary layer. When dust loading decreases, the impact of fine mode particles emerges. The changes of EAE, BAE, PLDR and lidar ratios above 2200 m are a clear evidence of polluted dust. The pollution could be lifted up from the ground in local area by convection or be transported from other area. Additionally, the RH at above 2500 m is about 60±12%–80±16%, which could lead to the hygroscopic growth of some aerosol species. Pure dust is regarded as hydrophobic aerosols because its compounds are insoluble, but when mixed with hygroscopic aerosol species, for example, nitrate, the ensemble of aerosol mixture could become hygroscopic. The fine mode particles can be hydrophobic or hydroscopic, depending on their chemical compositions(Carrico et al., 2003; Shi et al., 2008; Pan et al., 2009). In this case, there were no clear evidence indicating the occurrence of hygroscopic growth or the mixing state of dust and pollution particles. A9

3.2.4 Case 4: 03 April 2019

The daily mean AOD on 03 April is 0.16 and the Ångström exponent is about 0.11. The boundary layer height is about 3000 to 4000 m, rising slightly in the night of 03–04 April. Starting from 16:30 UTC, some liquid cloud layers occurred at the top of the boundary layer (Figure 5(a)). Figure 12 shows the profiles derived from lidar observations at 14:00–16:00 UTC, 03 April. The extinction coefficients decrease from about 0.28±0.03 km^{-1} at 1000 m to about 0.10±0.01 km^{-1} at 3000 m, with $EAE_{355-532}$ ($BAE_{355-532}$) increasing from 0.01±0.30 (-0.38±0.3) to 0.28±0.30 (0.02±0.30). Below 2100 m, the lidar ratios are about 45±7 sr at 532 nm and 51±8 sr at 355 nm. The PLDRs are about 0.35±0.05 at 532 nm and 0.32±0.05 at 1064 nm and 0.28±–0.32±0.07 at 355 nm. Between 2100 and 3000 m, the variation of lidar ratios is not monotonic. At 2500 m, the lidar ratios reach the minimum of 38 ± 6 sr at 532 nm and 42 ± 6 sr at 355 nm, and the PLDRs are about 0.27±0.06 at 355 nm and 0.33±0.05 at 532 nm. Both the lidar ratios and PLDRs at 2400-2800 m range are very consistent with the properties of Central Asia dust reported by Hofer et al. (2017) and Hofer et al. (2020). Above 2500 m, the lidar ratios and the RH (as well as WVMR) re-increase, and PLDRs decrease. At 3000 m, the PLDR at 532 nm drops below 0.30, suggesting that aerosols are different from those at lower boundary layer. The signatures of lidar ratio, RH and PLDR are possibly linked to the occurrence of polluted dust particles. In addition, long-range transported dust could also possess such PLDRs due to the deposition of big particles in the transport. This case is classified as polluted dust because the PLDR below 0.30 at 532 nm, the increase of WVMR (as well as RH) and $\mathrm{EAE}_{355-532}$) at the boundary layer top fit better the characteristics of polluted dust.

A10

B9 &A11

Figure 13 plots the 72-hour back trajectories for 1000, 2000 and 3000 m. Air masses at 1000 and 2000 m are from the Taklamakan desert, while the air mass at 3000 m is from Central Asia. It corroborates the similarities of the lidar ratios and PLDRs between the measurements in Hofer's studies and in our study. When extending the trajectory duration to 96 hours, the results (not plotted) suggest that air mass at 3000 m is originated from North Africa. This result suggests that dust particles observed in Kashi may have a long-transported aerosol component. The air mass clustering based on 24-hour back trajectories (not shown) indicates that about 52% of air mass at 3000 m is from North Africa and Arabian Peninsula. At 3500 m, this proportion increases to 74% and there is also a fraction of air mass coming from Europe. The complexity in the aerosol sources in the transport pathways explains the variability of aerosol properties at upper boundary layer in Case 4.

4 Discussion

Aerosol source

B1

The optical parameters in the 4 cases are summarized in Table 2. The coarse-mode dust and fine-mode particles originated from anthropogenic emission or transport are the two important aerosol components in Kashi. During the campaign, dust is undoubtedly the predominant component. In dust events (Case 1 and Case 2), dust particles are lifted from the Taklamakan desert by the low-pressure system along with strong wind, and then blown to the observation site by the easterly or northeasterly wind. In dry deposition, coarse-mode particles, especially giant particles (radius > 20 μm) settle down faster than the fine-mode dust particles. In many previous campaigns, the observed dust particles have undergone long-range transport, ranging from several hundreds or thousands kilometers (Dieudonné et al., 2015; Murayama et al., 2004; Veselovskii et al., 2016; Ansmann et al., 2003; Haarig et al., 2017; Hofer et al., 2017, 2020; Filioglou et al., 2020). While the transport distance is much shorter in DAO campaign. Thus, the observed dust particles in DAO campaign are more likely to contain a large fraction of coarse-mode and giant particles, which is an important difference of our observations compared with most previous observations. Moreover, the mineral composition of dust is size-dependent. For example, Kandler et al. (2009, 2011) found, in Saharan dust, a tendency of higher quartz content in larger particles, while in the size range smaller than 1 μm, a significant fraction of sulfate was found. The iron-bearing minerals, which is linked to the dust absorption, are more concentrated in the fraction with radius smaller than 2.0 μm. The difference in the size distribution could lead to a difference in mineralogical composition and chemical properties

A11

(Ryder et al., 2018; Biagio et al., 2019).

The influence of pollution is not clearly seen in the dust storms. However, when the activities of the Taklamakan desert wane and dust concentration becomes lower, the impact of pollution emerges. Observations in Case 3 clearly demonstrate the contrast of dust in the lower boundary layer and polluted dust particles at the boundary layer top. During the 1-month campaign, the traces of pollution, featured with increased EAE$_{355-532}$ and decreased PLDRs are frequently observed. The evidence of pollution in Taklamakan dust has been found in previous in-situ measurements. Huang et al. (2010) sampled aerosol particles in springtime at Tazhong site, which is located in the north rim of Taklamakan desert, and found that the As element was moderately enriched. The As element is a tracer of pollution, originated probably from coal burning. It is also found that the concentration of sulfate in Taklamakan dust is at a high level. The increased concentration of sulfate in the Taklamakan dust could be related to the provenance of the Taklamakan desert, because it is speculated to be ocean 5–7 millions years ago (Sun and Liu, 2006). Sulfate could also come from anthropogenic emission, for example, the uptake of the SO2 gases. Iwasaka et al. (2003) examined the aerosol samples using electron microscopy in Dunhuang, China, which is in the downwind of transported Taklamakan dust. They found that mineral dust is the main component in the coarse-mode aerosols, while in the fine mode, ammonia sulfate, which is mainly from anthropogenic emissions, is the major component. These studies indicate that the Taklamakan dust near the source region have been contaminated by other aerosols with anthropogenic origins. It is in agreement with our analysis, however, in this study we cannot clarify the exact involved aerosol species and the mixing state in the polluted dust. In our study, polluted dust mostly appeared at the boundary layer top, which agrees with the finding of Iwasaka et al. (2003). These fine particles are possibly lifted by convective air flow and then remain at higher altitude as bigger particles settle down.

Long-range transported aerosols are another possible aerosol origin in Kashi. Based on model simulations, some previous studies have reported intercontinental dust transport from North Africa or the Middle East to the East Asia (Park et al., 2005; Tanaka et al., 2005; Sugimoto et al., 2019). Figure 14 plots the air mass clustering for three different vertical levels in April 2019. The contribution of air masses from Central Asia, Middle East, Europe and North Africa always exists and the influence increases with height. At 1000 m, the main aerosol source is from the Taklamakan desert and accounts for about 73%. At 3000 m, air mass from Central Asia, Middle East and North Africa accounts for about 51%, and there is about 2% of air mass from Europe. While at 4000 m, air mass from the Taklamakan occupies only 29% and the rest are from Central Asia, the Middle East and North Africa. The west-to-east airmass transport is associated with the midlatitude westerlies, which is a continuous force for air mass transport (Yumimoto et al., 2009; Yu et al., 2019). In Case 4, we observed dust signatures that differ from Taklamakan dust but correspond well with the results from Hofer et al. (2017) and Hofer et al. (2020) in Dushanbe. Nevertheless, there are various aerosol sources in the intercontinental transport pathway, such as dust from North Africa, Middle East and Central Asia, pollution and biomass burning from East Europe. Moreover, the aerosol properties could be modified during the transport. Hence, it is difficult to find out the exact aerosol types using lidar observations.

Lidar ratio and depolarization ratio

B1

We found that, for Taklamakan dust, the lidar ratios are about 45±7 sr at 532 nm and 51–56±8 sr at 355 nm. The PLDRs are about 0.28–0.32±0.07 at 355 nm, 0.36±0.05 at 532 nm and 0.31±0.05 at 1064 nm. Table 3 presents an overview of the lidar ratios and PLDRs of Asian, Saharan and American dust in previous publications. Jin et al. (2010) derived a lidar ratio of 42±3 sr at 532 nm for Taklamakan dust, which agrees well with our results. The observation site in Jin et al. (2010) was very close to Kashi, however, their results were based on the observations of an elastic lidar, so it requires the assumption of vertically independent lidar ratio and complementary measurements. Observations obtained from other Asian sites show mean lidar ratio in the range of 40–50 (39–43) sr and PLDR in the range of 0.17–0.29 (0.20–0.35) at 355(532) nm (Dieudonné et al., 2015; Murayama et al., 2004; Hofer et al., 2017, 2020; Filioglou et al., 2020). Both the lidar ratios and PLDRs are slightly lower than the results we obtained from Taklamakan dust. Case 4 in this study shows the coincidence of characteristics of Taklamakan dust in the lower boundary layer and Central Asian dust (Hofer et al., 2017) in the upper boundary layer. This coincidence proves that the differences of lidar ratios and PLDRs between Taklamakan dust and Central Asia dust are not caused by a systematic bias of measurements in two different lidar systems, but that the two types of dust are optically different. The large fraction of coarse-mode and giant particles in Taklamakan dust are supposed to be the main reason responsible for this difference. Moreover, differences of the dust mineralogical composition in various geographical locations may also contribute to the differences in optical properties. For example, observations in SAMUM and SHADOW campaigns revealed lower PLDRs and higher lidar ratios in Saharan dust compared with Asian dust (Groß et al., 2011; Veselovskii et al., 2016, 2020). It could be explained by the argument that Saharan dusts tend to be more absorbing than Asian dust due to its relative higher content of iron oxides (Biagio et al., 2019).

A3

Recent studies concluded that there are similarities in dust size and shape parameters, which explain the relatively uniform distribution dust PLDRs for globally distributed dust sources. Nevertheless, the variability of dust properties should still be considered. PLDRs as high as Taklamakan dust have ever been found in several previous studies. Burton et al. (2015) found comparable PLDR of 0.37 at 532 nm in American dust near the source, but at 355 nm, the PLDR was about 0.24, falling in the typical range of dust. Sakai et al. (2010) derived PLDR (at 532 nm) of 0.39 for Asian and Saharan dust with high number concentration of supermicrometer particles, while for submicrometer particles, the PLDR was about 0.14–0.17. It proves that increase of big particle concentration could strongly increase the PLDR. Miffre et al. (2016) measured artificial dust samples with mainly submicrometer particles and derived PLDR of 0.37 at 355 nm and 0.36 at 532 nm. The high PLDRs are likely caused by the sharp edges and corners produced in the fabrication of dust samples. In naturally formed dust particles, these corners or edges may be trimmed by aeolian or fluvial erosion. This could be one reason why previous dust observations never found PLDR greater than 0.30 at 355 nm. While near the source and in heavy dust event, we suppose that the lifted dust may contain a fraction of big and morphologically complicated particles, which have strong depolarizing effects. Since Taklamakan dust observations in the source region are quite rare, more observational data are needed for complementing the data set of dust characteristics.

5 Conclusions

The first session of DAO campaign was conducted in Kashi, China in April 2019. The objective of DAO campaign is to provide a comprehensive characterization of Taklamakan dust using multi-wavelength Mie-Raman lidar measurements. During the nearly 1 month campaign, we found that, dust particles, originated mainly from the Taklamakan desert, are the dominant aerosol component in springtime in Kashi, while the influence of fine-mode particles needs also to be considered. Kashi is a populated region, pollution emitted from anthropogenic activities very likely the main component in fine-mode aerosols. Additionally, air mass clustering using the HYSPLIT model suggests that long-range transported aerosols from Africa, Europe, the Middle East and Central Asia could be a potential aerosol origin in Kashi. This study provides the first characterization of the spectral lidar ratios and PLDRs of the Taklamakan dust. One distinct feature of Taklamakan dust is its relatively high PLDRs compared with other Asian dust and Saharan dust. We suppose this difference is related to the coarse-mode and giant particles that remain in the Taklamakan dust near the source region. The results fill the gap of the characterization of Taklamakan dust and provide reference for succeeding studies and for implementing the climate modeling. This study also points out the importance of considering the dust mixing with pollution in climate modeling. Our results show that, in the most dusty season of the year and at an observation site with 150 km to the desert, the observed Taklamakan dust has already been polluted. Pollution could alter the optical and microphysical properties of dust particles, thus influencing the direct radiative forcing. Moreover, polluted dust could modify the cloud formation process by acting as cloud condensation nuclei and ice nuclei, which impose indirect influence on the earth's radiation budget and the long-term climate change. The DAO campaign offers a nice collection of measurements relevant to cloud-dust interactions, which will be presented in the next step.

Data availability. The satellite data from OMPS and AIRS can be found in NASA's GES DIS service center. The meteorological data, GDAS data and the HYSPLIT dispersion model are available in the NOAA ARL site (https://ready.arl.noaa.gov/HYSPLIT.php). All the other data presented in this study are available upon any request of readers.

Author contributions. The project was supervised by PG and ZL. QH, TP and IV were in charge of the Lidar operation and maintenance. QH, IV and HW performed the data analysis. QH wrote the manuscript of this paper. KL provide the sun/sky photometer data. MK helped in the lidar operation and instrument preparation.

Competing interests. The authors declare that they have no conflict of interest.

Acknowledgements. We acknowledge the colleagues in the Institute of Remote Sensing and Digital Earth () for their kind help and for the financial support. And we thank the colleagues in the GPI RAS (Prokhorov General Physics Institute of the Russian Academy of Sciences), LOA (Service National d'Observation, PHOTONS/AERONET-ACTRIS), ESA/IDEAS+ project and IAP (Institue of Atmospheric Physics) for the participation and the efforts they have made for the campaign. The Russian Science Foundation, (project 16-17-10241) is acknowledged for providing lidar data processing algorithms.

References

Ansmann, A., Riebesell, M., Wandinger, U., Weitkamp, C., Voss, E., Lahmann, W., and Michaelis, W.: Combined Raman elastic-backscatter lidar for vertical profiling of moisture, aerosol extinction, backscatter, and lidar ratio, Applied Physics B: Lasers and Optics, 55, 18–28, 1992.

Ansmann, A., Bösenberg, J., Chaikovsky, A., Comerón, A., Eckhardt, S., Eixmann, R., Freudenthaler, V., Ginoux, P., Komguem, L., Linné, H., et al.: Long-range transport of Saharan dust to northern Europe: The 11–16 October 2001 outbreak observed with EARLINET, Journal of Geophysical Research: Atmospheres, 108, 2003.

Biagio, C. D., Formenti, P., Balkanski, Y., Caponi, L., Cazaunau, M., Pangui, E., Journet, E., Nowak, S., Andreae, M. O., Kandler, K., et al.: Complex refractive indices and single-scattering albedo of global dust aerosols in the shortwave spectrum and relationship to size and iron content, Atmospheric Chemistry and Physics, 19, 15 503–15 531, 2019.

Boucher, O., Randall, D., Artaxo, P., Bretherton, C., Feingold, G., Forster, P., Kerminen, V.-M., Kondo, Y., Liao, H., Lohmann, U., et al.: Clouds and aerosols, in: Climate change 2013: the physical science basis. Contribution of Working Group I to the Fifth Assessment Report of the Intergovernmental Panel on Climate Change, pp. 571–657, Cambridge University Press, 2013.

Bovchaliuk, V., Goloub, P., Podvin, T., Veselovskii, I., Tanre, D., Chaikovsky, A., Dubovik, O., Mortier, A., Lopatin, A., Korenskiy, M., et al.: Comparison of aerosol properties retrieved using GARRLiC, LIRIC, and Raman algorithms applied to multi-wavelength lidar and sun/sky-photometer data, Atmospheric Measurement Techniques, 9, 3391–3405, 2016.

Burton, S., Hair, J., Kahnert, M., Ferrare, R., Hostetler, C., Cook, A., Harper, D., Berkoff, T., Seaman, S., Collins, J., et al.: Observations of the spectral dependence of linear particle depolarization ratio of aerosols using NASA Langley airborne High Spectral Resolution Lidar, Atmospheric Chemistry and Physics, 15, 13 453–13 473, 2015.

Campbell, J. R., Reid, J. S., Westphal, D. L., Zhang, J., Hyer, E. J., and Welton, E. J.: CALIOP aerosol subset processing for global aerosol transport model data assimilation, IEEE Journal of Selected Topics in Applied Earth Observations and Remote Sensing, 3, 203–214, 2010.

Carrico, C. M., Kus, P., Rood, M. J., Quinn, P. K., and Bates, T. S.: Mixtures of pollution, dust, sea salt, and volcanic aerosol during ACE-Asia: Radiative properties as a function of relative humidity, Journal of Geophysical Research: Atmospheres, 108, 2003.

Dieudonné, E., Chazette, P., Marnas, F., Totems, J., and Shang, X.: Lidar profiling of aerosol optical properties from Paris to Lake Baikal (Siberia), Atmospheric Chemistry and Physics, 15, 5007–5026, 2015.

Doxsey-Whitfield, E., MacManus, K., Adamo, S. B., Pistolesi, L., Squires, J., Borkovska, O., and Baptista, S. R.: Taking advantage of the improved availability of census data: a first look at the gridded population of the world, version 4, Papers in Applied Geography, 1, 226–234, 2015.

Engelstaedter, S., Tegen, I., and Washington, R.: North African dust emissions and transport, Earth-Science Reviews, 79, 73–100, 2006.

Esselborn, M., Wirth, M., Fix, A., Weinzierl, B., Rasp, K., Tesche, M., and Petzold, A.: Spatial distribution and optical properties of Saharan dust observed by airborne high spectral resolution lidar during SAMUM 2006, Tellus B: Chemical and Physical Meteorology, 61, 131–143, 2009.

Fan, J., Wang, Y., Rosenfeld, D., and Liu, X.: Review of aerosol–cloud interactions: Mechanisms, significance, and challenges, Journal of the Atmospheric Sciences, 73, 4221–4252, 2016.

Filioglou, M., Giannakaki, E., Backman, J., Kesti, J., Hirsikko, A., Engelmann, R., O'Connor, E., Leskinen, J. T. T., Shang, X., Korhonen, H., Lihavainen, H., Romakkaniemi, S., and Komppula, M.: Optical and geometrical aerosol particle properties over the United Arab Emirates, Atmospheric Chemistry and Physics, 20, 8909–8922, https://doi.org/10.5194/acp-20-8909-2020, https://acp.copernicus.org/articles/20/8909/2020/, 2020.

Flynn, L. E., Homstein, J., and Hilsenrath, E.: The ozone mapping and profiler suite (OMPS). The next generation of US ozone monitoring instruments, in: Geoscience and Remote Sensing Symposium, 2004. IGARSS'04. Proceedings. 2004 IEEE International, vol. 1, IEEE, 2004.

Freudenthaler, V., Esselborn, M., Wiegner, M., Heese, B., Tesche, M., Ansmann, A., Müller, D., Althausen, D., Wirth, M., Fix, A., Ehret, G., Knippertz, P., Toledano, C., Gasteiger, J., Garhammer, M., and Seefeldner, M.: Depolarization ratio profiling at several wavelengths in pure Saharan dust during SAMUM 2006, Tellus B, 61, 165–179, 2009.

Ginoux, P., Prospero, J. M., Gill, T. E., Hsu, N. C., and Zhao, M.: Global-scale attribution of anthropogenic and natural dust sources and their emission rates based on MODIS Deep Blue aerosol products, Reviews of Geophysics, 50, 2012.

Groß, S., Tesche, M., Freudenthaler, V., Toledano, C., Wiegner, M., Ansmann, A., Althausen, D., and Seefeldner, M.: Characterization of Saharan dust, marine aerosols and mixtures of biomass-burning aerosols and dust by means of multi-wavelength depolarization and Raman lidar measurements during SAMUM 2, Tellus B: Chemical and Physical Meteorology, 63, 706–724, 2011.

Groß, S., Freudenthaler, V., Schepanski, K., Toledano, C., Schäfler, A., Ansmann, A., and Weinzierl, B.: Optical properties of long-range transported Saharan dust over Barbados as measured by dual-wavelength depolarization Raman lidar measurements, Atmospheric Chemistry and Physics, pp. 11 067–11 080, 2015.

Haarig, M., Ansmann, A., Althausen, D., Klepel, A., Groß, S., Freudenthaler, V., Toledano, C., Mamouri, R.-E., Farrell, D. A., Prescod, D. A., et al.: Triple-wavelength depolarization-ratio profiling of Saharan dust over Barbados during SALTRACE in 2013 and 2014, Atmospheric Chemistry and Physics, 17, 10 767, 2017.

Hofer, J., Althausen, D., Abdullaev, S. F., Makhmudov, A. N., Nazarov, B. I., Schettler, G., Engelmann, R., Baars, H., Fomba, K. W., Müller, K., et al.: Long-term profiling of mineral dust and pollution aerosol with multiwavelength polarization Raman lidar at the Central Asian site of Dushanbe, Tajikistan: case studies, Atmospheric Chemistry and Physics, 17, 14 559, 2017.

Hofer, J., Ansmann, A., Althausen, D., Engelmann, R., Baars, H., Fomba, K. W., Wandinger, U., Abdullaev, S. F., and Makhmudov, A. N.: Optical properties of Central Asian aerosol relevant for spaceborne lidar applications and aerosol typing at 355 and 532 nm, Atmospheric Chemistry and Physics, 20, 9265–9280, https://doi.org/10.5194/acp-20-9265-2020, https://acp.copernicus.org/articles/20/9265/2020/, 2020.

Holben, B. N., Eck, T. F., Slutsker, I., Tanre, D., Buis, J., Setzer, A., Vermote, E., Reagan, J., Kaufman, Y., Nakajima, T., et al.: AERONET—A federated instrument network and data archive for aerosol characterization, Remote sensing of environment, 66, 1–16, 1998.

Hsu, N. C., Herman, J., Torres, O., Holben, B., Tanre, D., Eck, T., Smirnov, A., Chatenet, B., and Lavenu, F.: Comparisons of the TOMS aerosol index with Sun-photometer aerosol optical thickness: Results and applications, Journal of Geophysical Research: Atmospheres, 104, 6269–6279, 1999.

Hu, Q., Goloub, P., Veselovskii, I., Bravo-Aranda, J.-A., Popovici, I. E., Podvin, T., Haeffelin, M., Lopatin, A., Dubovik, O., Pietras, C., et al.: Long-range-transported Canadian smoke plumes in the lower stratosphere over northern France, Atmospheric Chemistry and Physics, 19, 1173–1193, 2019.

Huang, J., Minnis, P., Chen, B., Huang, Z., Liu, Z., Zhao, Q., Yi, Y., and Ayers, J. K.: Long-range transport and vertical structure of Asian dust from CALIPSO and surface measurements during PACDEX, Journal of Geophysical Research: Atmospheres, 113, 2008.

Huang, K., Zhuang, G., Li, J., Wang, Q., Sun, Y., Lin, Y., and Fu, J. S.: Mixing of Asian dust with pollution aerosol and the transformation of aerosol components during the dust storm over China in spring 2007, Journal of Geophysical Research: Atmospheres, 115, 2010.

Huneeus, N., Schulz, M., Balkanski, Y., Griesfeller, J., Prospero, M., Kinne, S., Bauer, S., Boucher, O., Chin, M., Dentener, F., et al.: Global dust model intercomparison in AeroCom phase I, Atmospheric Chemistry and Physics, 11, 7781–7816, 2011.

Iwasaka, Y., Shi, G.-Y., Yamada, M., Matsuki, A., Trochkine, D., Kim, Y., Zhang, D., Nagatani, T., Shibata, T., Nagatani, M., et al.: Importance of dust particles in the free troposphere over the Taklamakan Desert: electron microscopic experiments of particles collected with a balloonborne particle impactor at Dunhuang, China, Journal of Geophysical Research: Atmospheres, 108, 2003.

Iwasaka, Y., Li, J., Shi, G.-Y., Kim, Y., Matsuki, A., Trochkine, D., Yamada, M., Zhang, D., Shen, Z., and Hong, C.: Mass transport of background Asian dust revealed by balloon-borne measurement: dust particles transported during calm periods by westerly from Taklamakan desert, in: Advanced environmental monitoring, pp. 121–135, Springer, 2008.

Jin, Y., Kai, K., Shibata, T., Zhang, K., and Zhou, H.: Validation of the dust layer structure over the Taklimakan Desert, China by the CALIOP space-borne lidar using ground-based lidar, Sola, 6, 121–124, 2010.

Kai, K., Nagata, Y., Tsunematsu, N., Matsumura, T., Kim, H.-S., Matsumoto, T., Hu, S., Zhou, H., Abo, M., and Nagai, T.: The Structure of the Dust Layer over the Taklimakan Deser during the Dust Storm in April 2002 as Observed Using a Depolarization Lidar, Journal of the Meteorological Society of Japan. Ser. II, 86, 1–16, 2008.

Kandler, K., Schütz, L., Deutscher, C., Ebert, M., Hofmann, H., Jäckel, S., Jaenicke, R., Knippertz, P., Lieke, K., Massling, A., et al.: Size distribution, mass concentration, chemical and mineralogical composition and derived optical parameters of the boundary layer aerosol at Tinfou, Morocco, during SAMUM 2006, Tellus B: Chemical and Physical Meteorology, 61, 32–50, 2009.

Kandler, K., Lieke, K., Benker, N., Emmel, C., Küpper, M., Müller-Ebert, D., Ebert, M., Scheuvens, D., Schladitz, A., Schütz, L., et al.: Electron microscopy of particles collected at Praia, Cape Verde, during the Saharan Mineral Dust Experiment: particle chemistry, shape, mixing state and complex refractive index, Tellus B: Chemical and Physical Meteorology, 63, 475–496, 2011.

Kanji, Z. A., Ladino, L. A., Wex, H., Boose, Y., Burkert-Kohn, M., Cziczo, D. J., and Krämer, M.: Overview of Ice Nucleating Particles, Meteorological Monographs, 58, 1.1–1.33, https://doi.org/10.1175/AMSMONOGRAPHS-D-16-0006.1, https://doi.org/10.1175/AMSMONOGRAPHS-D-16-0006.1, 2017.

Klett, J. D.: Lidar inversion with variable backscatter/extinction ratios, Applied Optics, 24, 1638–1643, 1985.

Kojima, T., Buseck, P. R., Iwasaka, Y., Matsuki, A., and Trochkine, D.: Sulfate-coated dust particles in the free troposphere over Japan, Atmospheric research, 82, 698–708, 2006.

Li, Z., Xu, H., Li, K., Li, D., Xie, Y., Li, L., Zhang, Y., Gu, X., Zhao, W., Tian, Q., et al.: Comprehensive study of optical, physical, chemical, and radiative properties of total columnar atmospheric aerosols over China: an overview of sun–sky radiometer observation network (SONET) measurements, Bulletin of the American Meteorological Society, 99, 739–755, 2018.

Littmann, T.: Dust storm frequency in Asia: climatic control and variability, International Journal of Climatology, 11, 393–412, 1991.

Liu, Z., Sugimoto, N., and Murayama, T.: Extinction-to-backscatter ratio of Asian dust observed with high-spectral-resolution lidar and Raman lidar, Applied Optics, 41, 2760–2767, 2002.

Miffre, A., Mehri, T., Francis, M., and Rairoux, P.: UV–VIS depolarization from Arizona Test Dust particles at exact backscattering angle, Journal of Quantitative Spectroscopy and Radiative Transfer, 169, 79–90, 2016.

Murayama, T., Müller, D., Wada, K., Shimizu, A., Sekiguchi, M., and Tsukamoto, T.: Characterization of Asian dust and Siberian smoke with multi-wavelength Raman lidar over Tokyo, Japan in spring 2003, Geophysical Research Letters, 31, 2004.

Pan, X., Yan, P., Tang, J., Ma, J., Wang, Z., Gbaguidi, A., and Sun, Y.: Observational study of influence of aerosol hygroscopic growth on scattering coefficient over rural area near Beijing mega-city., Atmospheric Chemistry & Physics, 9, 2009.

Park, C. B., Sugimoto, N., Matsui, I., Shimizu, A., Tatarov, B., Kamei, A., Lee, C. H., Uno, I., Takemura, T., and Westphal, D. L.: Long-range transport of Saharan dust to east Asia observed with lidars, Sola, 1, 121–124, 2005.

Petrov, M. P. and S.Alitto, G.: Takla Makan Desert, https://www.britannica.com/place/Takla-Makan-Desert, 2019.

Qian, W., Quan, L., and Shi, S.: Variations of the dust storm in China and its climatic control, Journal of Climate, 15, 1216–1229, 2002.

Reed, K. A., Bacmeister, J. T., Huff, J. J. A., Wu, X., Bates, S. C., and Rosenbloom, N. A.: Exploring the Impact of Dust on North Atlantic Hurricanes in a High-Resolution Climate Model, Geophysical Research Letters, 46, 1105–1112, 2019.

Rolph, G., Stein, A., and Stunder, B.: Real-time environmental applications and display system: Ready, Environmental Modelling & Software, 95, 210–228, 2017.

Ryder, C. L., Marenco, F., Brooke, J. K., Estelles, V., Cotton, R., Formenti, P., McQuaid, J. B., Price, H. C., Liu, D., Ausset, P., Rosenberg, P. D., Taylor, J. W., Choularton, T., Bower, K., Coe, H., Gallagher, M., Crosier, J., Lloyd, G., Highwood, E. J., and Murray, B. J.: Coarse-mode mineral dust size distributions, composition and optical properties from AER-D aircraft measurements over the tropical eastern Atlantic, Atmospheric Chemistry and Physics, 18, 17 225–17 257, https://doi.org/10.5194/acp-18-17225-2018, https://acp.copernicus.org/articles/18/17225/2018/, 2018.

Sakai, T., Nagai, T., Zaizen, Y., and Mano, Y.: Backscattering linear depolarization ratio measurements of mineral, sea-salt, and ammonium sulfate particles simulated in a laboratory chamber, Applied optics, 49, 4441–4449, 2010.

Seftor, C., Jaross, G., Kowitt, M., Haken, M., Li, J., and Flynn, L.: Postlaunch performance of the Suomi National Polar-orbiting Partnership Ozone Mapping and Profiler Suite (OMPS) nadir sensors, Journal of Geophysical Research: Atmospheres, 119, 4413–4428, 2014.

Sekiyama, T., Tanaka, T., Shimizu, A., and Miyoshi, T.: Data assimilation of CALIPSO aerosol observations., Atmospheric Chemistry & Physics, 10, 2010.

Shi, Z., Zhang, D., Hayashi, M., Ogata, H., Ji, H., and Fujiie, W.: Influences of sulfate and nitrate on the hygroscopic behaviour of coarse dust particles, Atmospheric Environment, 42, 822–827, 2008.

Stein, A., Draxler, R. R., Rolph, G. D., Stunder, B. J., Cohen, M., and Ngan, F.: NOAA's HYSPLIT atmospheric transport and dispersion modeling system, Bulletin of the American Meteorological Society, 96, 2059–2077, 2015.

Sugimoto, N., Shimizu, A., Nishizawa, T., and Jin, Y.: Long-range transport of mineral dust observed with the Asian Dust and aerosol lidar observation Network (AD-Net), in: E3S Web of Conferences, vol. 99, EDP Sciences, 2019.

Sun, J. and Liu, T.: The age of the Taklimakan Desert, Science, 312, 1621–1621, 2006.

Tanaka, T. Y. and Chiba, M.: A numerical study of the contributions of dust source regions to the global dust budget, Global and Planetary Change, 52, 88–104, 2006.

Tanaka, T. Y., Kurosaki, Y., Chiba, M., Matsumura, T., Nagai, T., Yamazaki, A., Uchiyama, A., Tsunematsu, N., and Kai, K.: Possible transcontinental dust transport from North Africa and the Middle East to East Asia, Atmospheric Environment, 39, 3901–3909, 2005.

Tesche, M., Ansmann, A., Mueller, D., Althausen, D., Mattis, I., Heese, B., Freudenthaler, V., Wiegner, M., Esselborn, M., Pisani, G., et al.: Vertical profiling of Saharan dust with Raman lidars and airborne HSRL in southern Morocco during SAMUM, Tellus B: Chemical and Physical Meteorology, 61, 144–164, 2009.

Textor, C., Schulz, M., Guibert, S., Kinne, S., Balkanski, Y., Bauer, S., Berntsen, T., Berglen, T., Boucher, O., Chin, M., et al.: Analysis and quantification of the diversities of aerosol life cycles within AeroCom, Atmospheric Chemistry and Physics, 6, 1777–1813, 2006.

Thompson, A. J., Skinner, C. B., Poulsen, C. J., and Zhu, J.: Modulation of mid-Holocene African rainfall by dust aerosol direct and indirect effects, Geophysical Research Letters, 46, 3917–3926, 2019.

Uno, I., Eguchi, K., Yumimoto, K., Takemura, T., Shimizu, A., Uematsu, M., Liu, Z., Wang, Z., Hara, Y., and Sugimoto, N.: Asian dust transported one full circuit around the globe, Nature Geoscience, 2, 557–560, 2009.

VanCuren, R. A. and Cahill, T. A.: Asian aerosols in North America: Frequency and concentration of fine dust, Journal of Geophysical Research: Atmospheres, 107, AAC–19, 2002.

Veselovskii, I., Whiteman, D., Korenskiy, M., Suvorina, A., and Pérez-Ramírez, D.: Use of rotational Raman measurements in multiwavelength aerosol lidar for evaluation of particle backscattering and extinction, Atmospheric Measurement Techniques, 8, 4111–4122, 2015.

Veselovskii, I., Goloub, P., Podvin, T., Bovchaliuk, V., Derimian, Y., Augustin, P., Fourmentin, M., Tanre, D., Korenskiy, M., Whiteman, D., et al.: Retrieval of optical and physical properties of African dust from multiwavelength Raman lidar measurements during the SHADOW campaign in Senegal, Atmos. Chem. Phys, 16, 7013–7028, 2016.

Veselovskii, I., Hu, Q., Goloub, P., Podvin, T., Korenskiy, M., Derimian, Y., Legrand, M., and Castellanos, P.: Variability of Lidar-Derived Particle Properties Over West Africa Due to Changes in Absorption: Towards an Understanding, Atmospheric Chemistry and Physics Discussions, 2020, 1–37, https://doi.org/10.5194/acp-2020-98, https://www.atmos-chem-phys-discuss.net/acp-2020-98/, 2020.

Wang, Y., Sartelet, K., Bocquet, M., and Chazette, P.: Assimilation of ground versus lidar observations for PM10 forecasting, Atmospheric Chemistry and Physics, 13, 269–283, https://doi.org/10.5194/acp-13-269-2013, https://hal.inria.fr/hal-00783554, 2013.

Yu, Y., Kalashnikova, O. V., Garay, M. J., and Notaro, M.: Climatology of Asian dust activation and transport potential based on MISR satellite observations and trajectory analysis, Atmospheric Chemistry and Physics, 19, 363–378, 2019.

Yumimoto, K., Uno, I., Sugimoto, N., Shimizu, A., Liu, Z., and Winker, D.: Adjoint inversion modeling of Asian dust emission using lidar observations, Atmospheric Chemistry and Physics, 8, 2869–2884, 2008.

Yumimoto, K., Eguchi, K., Uno, I., Takemura, T., Liu, Z., Shimizu, A., and Sugimoto, N.: An elevated large-scale dust veil from the Taklimakan Desert: Intercontinental transport and three-dimensional structure as captured by CALIPSO and regional and global models, Atmospheric Chemistry and Physics, 9, 8545–8558, 2009.

Zhang, J., Campbell, J. R., Reid, J. S., Westphal, D. L., Baker, N. L., Campbell, W. F., and Hyer, E. J.: Evaluating the impact of assimilating CALIOP-derived aerosol extinction profiles on a global mass transport model, Geophysical research letters, 38, 2011.

Zhang, J., Hu, M.-M., Wang, Y.-Y., and Shu, H.-B.: TRIM32 protein modulates type I interferon induction and cellular antiviral response by targeting MITA/STING protein for K63-linked ubiquitination, Journal of Biological Chemistry, 287, 28 646–28 655, 2012.

Table 1. Daily averaged AOD at 500 nm and Ångström exponent (between 440 and 870 nm) measured by the sun/sky photometer in daytime. The values on the right side of '±' represent the standard deviation of the values on the left side.

	AOD$_{500}$	AE$_{440-870}$
Case 1, 09 April	1.48±0.10	0.04±0.02
Case 2, 24 April	3.63±1.28	-0.01±0.03
Case 3, 15 April	0.63±0.03	0.10±0.02
Case 4, 03 April	0.49±0.16	0.11±0.03

Table 2. A summary of optical properties derived from lidar observations in the case studies. The values before the '±' symbol represent the mean in the range of the layer height. The values after the '±' symbol represent the statistical error of the values before the symbol.

	Case 1: dust haze 15:00–16:00 09 April	**Case 2: dust storm** 15:00–16:00 24 April	**Case 3: polluted dust** 15:00–16:00 15 April		**Case 4: polluted dust** 15:00–16:00 03 April	
Layer height [m]	800–3800	800–2000	1000–2200	2400–2800	1000–1500	1500–3000
PLDR$_{355}$	0.32±0.05	0.32±0.05	0.32±0.07	0.23±0.06	0.30–0.32±0.07	0.21±0.05–0.29±0.07
PLDR$_{532}$	0.36±0.05	0.36±0.05	0.34±0.05	0.26±0.03	0.35±0.05	0.28±0.04–0.34±0.05
(V)PLDR$_{1064}$	0.31±0.04[a]	–	0.31±0.04	0.24±0.03	0.32±0.05	0.28±0.04–0.33±0.05
LR$_{355}$ [sr]	56±8	55[b]	51±8	42±6	51±8	43±6–57±8
LR$_{532}$ [sr]	46±7	45[b]	45±7	40±6	45±7	38±6–49±8
EAE$_{355-532}$	-0.01±0.30	0.01±0.30	0.02±0.30	0.10±0.30	0.02±0.30	0.14±0.30–0.30±0.30
BAE$_{355-532}$	-0.51±0.30	–	-0.29±0.30	-0.06±0.30	-0.29±0.30	-0.13±0.30–0.20±0.30
RH [%]	20±4–60±12	10±2–20±4	30±6–60±12	80±16	20±4–60±12	45±9–70±14
WVMR [g/kg]	2.2±0.5	–	3.5±7	4.0±0.8	2.7±0.6	2.7±0.6

[a] PLDR$_{1064}$ is not available in this case, but VLDR$_{1064}$ is. We assume VLDR$_{1064}$≈PLDR$_{1064}$ considering aerosol scattering is much stronger than molecular scattering. [b] 55 and 45 sr are assumed lidar ratios based on the results in Case 1.

Table 3. A review of dust lidar ratios and particle linear depolarization ratios in literatures. The values of lidar ratios and PLDRs, as well as their errors are based on the results in the references. Error estimates are not provided if their are not available in the original publication.

Dust source	Observation site	PLDRs			LRs		Reference
		355	532	1064	355	532	
Saharan dust	Ouarzazate^{1a}	–	0.30	–	–	38–50	Esselborn et al. (2009)
	Ouarzazate^{1b}	–	–	–	53–55	53–55	Tesche et al. (2009)
	Cape Verde	0.24–0.27	0.29–0.31	–	48–70	48–70	Groß et al. (2011)
	M'Bour^{2a}	–	0.34±0.05	–	68±10	50±8	Veselovskii et al. (2016)
	M'Bour^{2b}	–	0.32±0.05	–	55–60±9	55–60±8	Veselovskii et al. (2020)
	Leipzig	–	0.15-0.25		50–90	40–80	Ansmann et al. (2003)
	Barbados	0.26±0.03	0.27±0.01	–	53±5	56±7	Groß et al. (2015)
	Barbados	0.25±0.03	0.28±0.02	0.23±0.02	40–60	40–60	Haarig et al. (2017)
Asian dust	Aksu	–	–	–	–	42±3	Jin et al. (2010)
	Japan	–	0.20	–	49	43	Murayama et al. (2004)
	Kazan	0.23±0.02	–	–	43±14	–	Dieudonné et al. (2015)
	Omsk	0.17±0.02	–	–	50±13	–	
	Dushanbe^{3a}	0.23±0.01	0.35±0.01	–	47±2	43±3	Hofer et al. (2017)
	Dushanbe^{3b}	0.29±0.01	0.35±0.01	–	40±1	39±1	
	Dushanbe^{3c}	0.24±0.03	0.33±0.04	–	43±3	39±4	Hofer et al. (2020)
	UAE	0.25±0.02	0.31±0.02	–	45±5	42±5	Filioglou et al. (2020)
	Kashi	0.28±0.07 – 0.32±0.07	0.36±0.05	0.31±0.05	51±8 – 56±8	45±7	This study
American dust	Chihuahuan	0.24±0.05	0.37±0.02	0.38±0.01	–	–	Burton et al. (2015)
	Pico de Orizaba	–	0.33±0.02	0.40±0.01	–	–	Burton et al. (2015)

A12

^{1a}HSRL measurements; ^{1b}Raman lidar measurement; ^{2a} 29 March 2015 in the dry season; ^{2b}23–24 April 2015 in the transition period; ^{3a}Extreme dust case on 8 August 2015, ^{3b}Most extreme dust case on 14 July 2016; ^{3c} Statistical results estimated from 17 dust cases with $\mathrm{PLDR}_{532} > 0.31$.

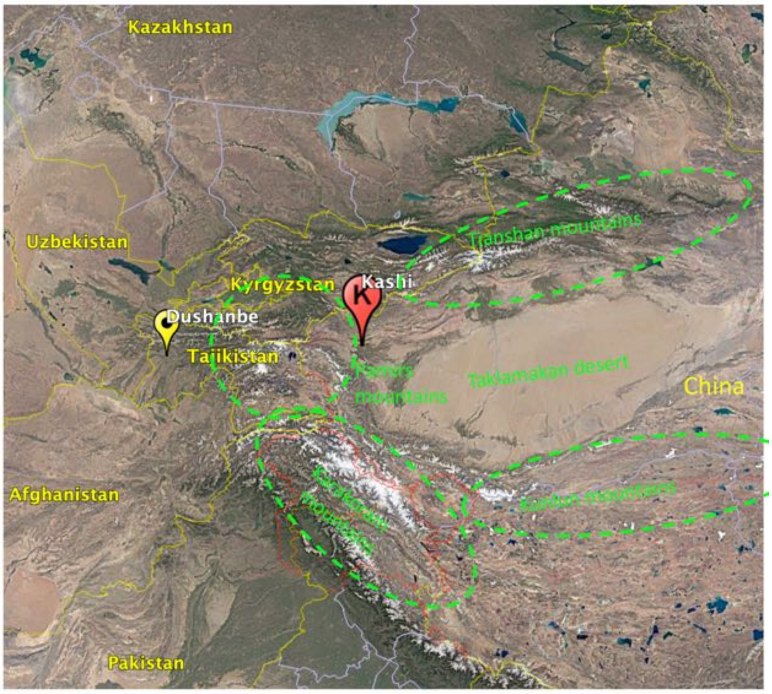

A13

Figure 1. The location of the observation site in Kashi (at 39.51N, 75.93E). The observation site is about 628 km in the east of Dushanbe, Tajikistan (38.53N, 68.77E). The green ellipses indicate the mountain ranges surrounding the Taklamakan desert, including the Tianshan mountains, the Pamir mountains, the Karakoram mountains, the Kunlun and Altun mountains. @ Google Maps 2020.

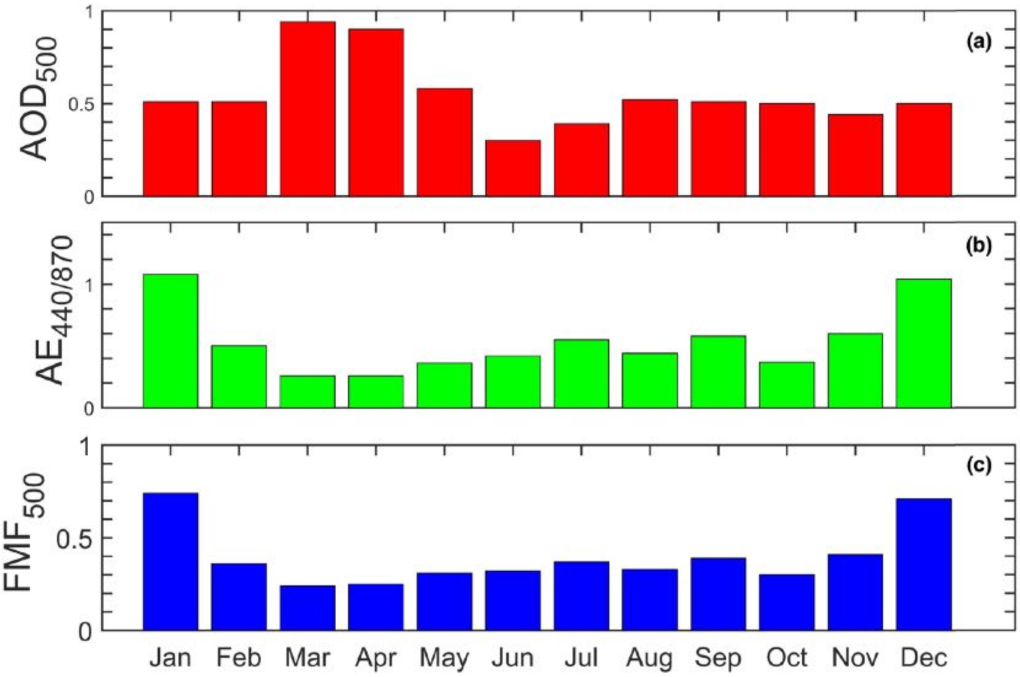

Figure 2. Monthly means of (a) the AOD at 500 nm, (b) Angström exponent (440–870) and (c) FMF at 500 nm from 2013 to 2017. The data are obtained from the SONET network.

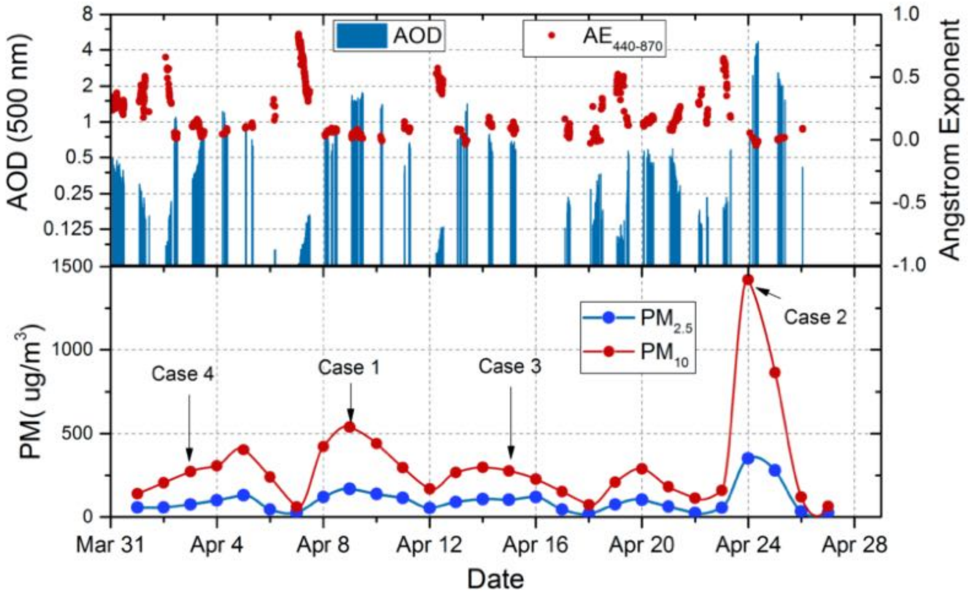

B6

Figure 3. The AOD at 500 nm, Angström exponent (440–870) and daily particulate matter (in $\mu g\, m^{-3}$) in April 2019. The AODs are measured by the sun/sky photometer deployed in Kashi site, and the data are stored in the SONET network. The particulate matter measurements are public data from a meteorological station, 5 km to the observation site.

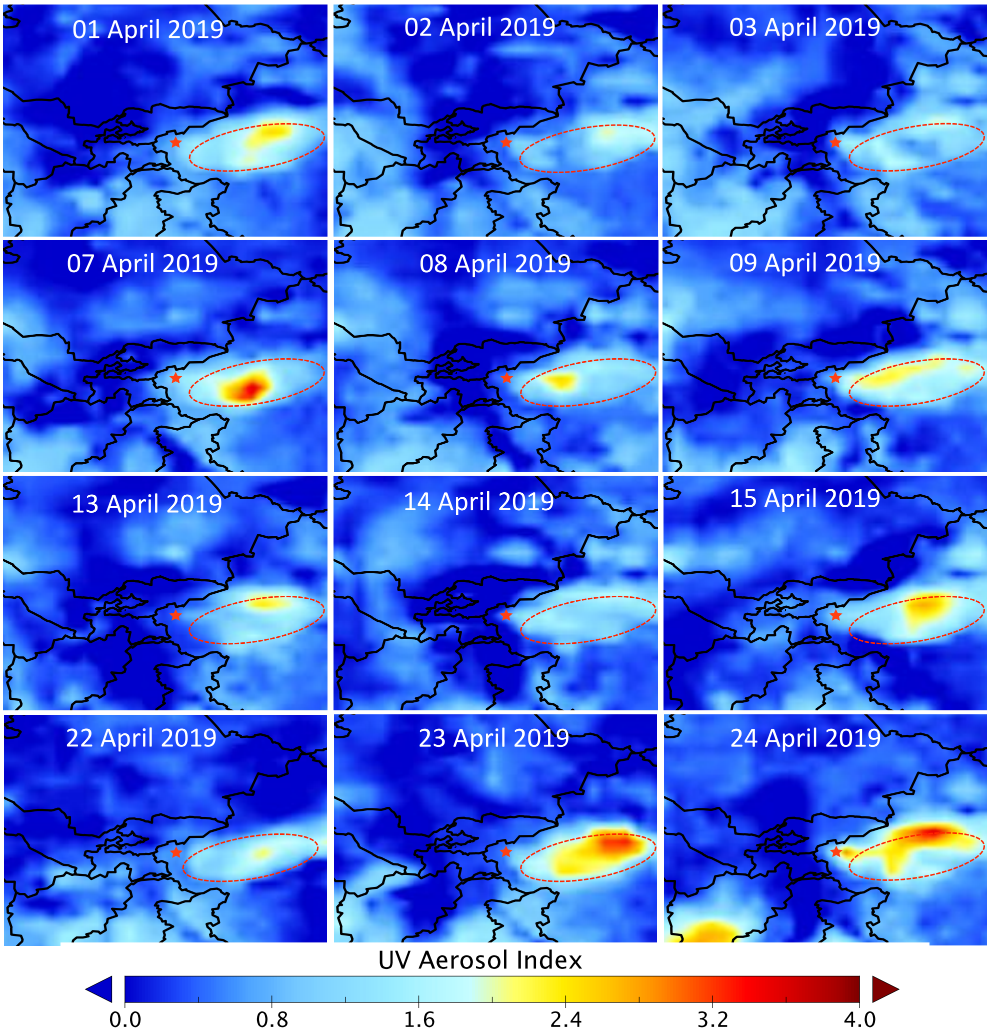

Figure 4. The UVAI derived from OMPS instrument onboard the Suomi-NPP satellite. The red star represents the location of the observation site. The dashed red ellipse represents the location of the Taklamakan desert.

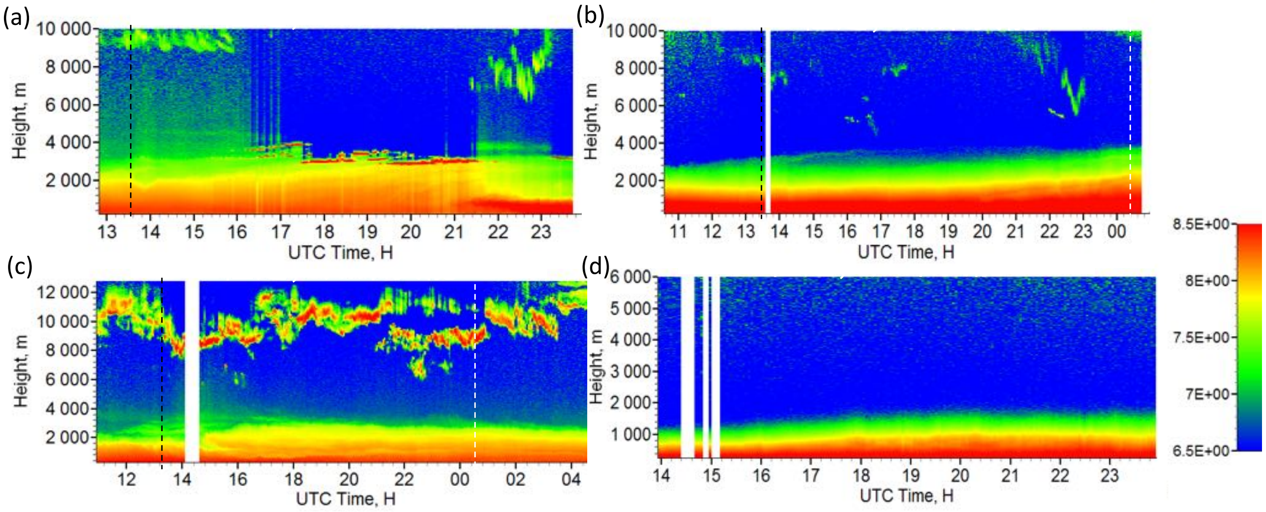

Figure 5. The quicklooks of the range-corrected lidar signal at 532 nm in the four cases: (a) Case 4: 03 April 2019, (b) Case 1: 09 April 2019, (c) Case 3: 15 April 2019and (d) Case 2: 24 April 2019. The dashed black lines represent the sunset time and dashed white lines represent the sunrise time.

B7

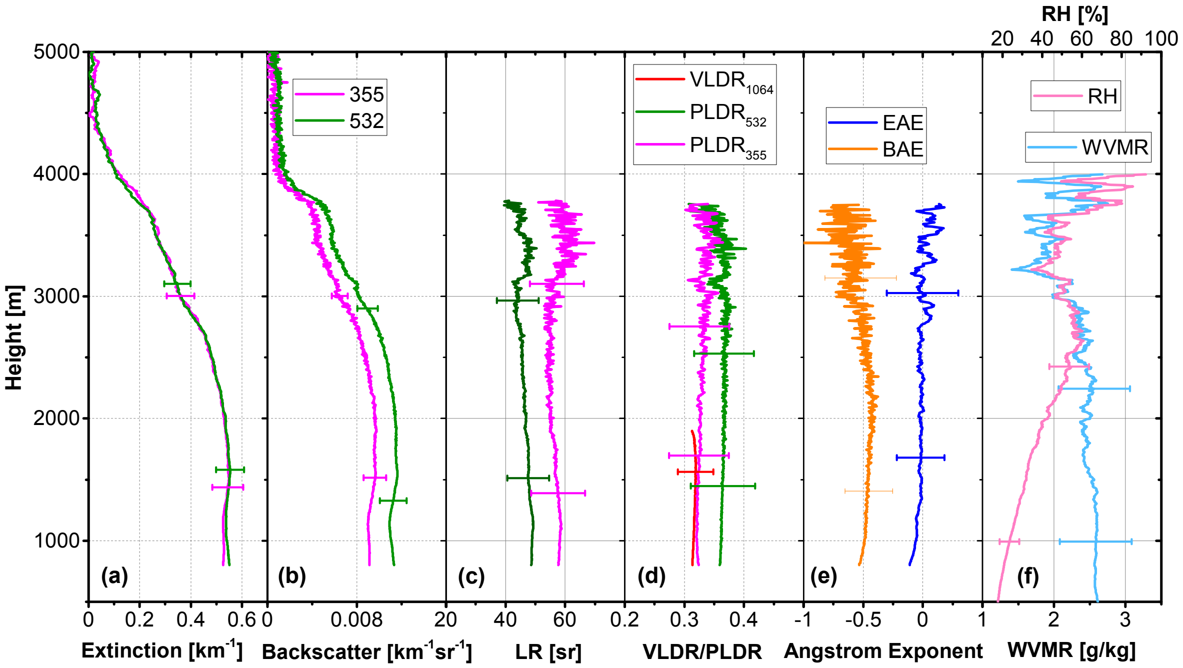

Figure 6. Case 1: Lidar derived parameters at 17:00–22:00 UTC, 09 April 2019. (a) Extinction coefficient, (b) backscattering coefficient, (c) lidar ratio, (d) PLDR/VLDR, (e) $\mathrm{EAE}_{355-532}$ and $\mathrm{BAE}_{355-532}$, (f) WVMR and RH.

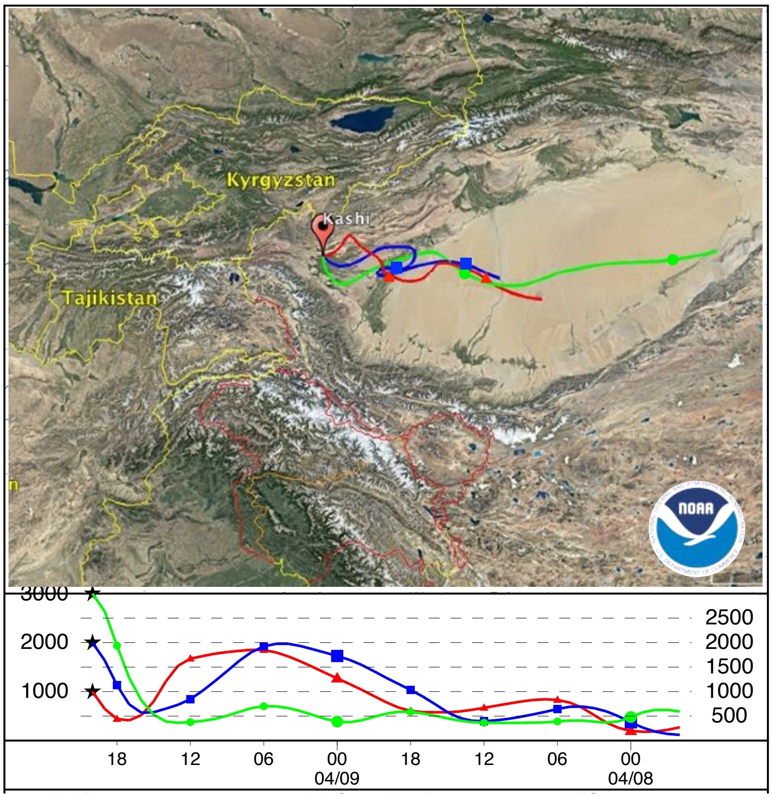

Figure 7. Case 1: The 48-hour back trajectories ending at 20:00 UTC, 09 April 2019 for air mass at 1000, 2000 and 3000 m. @ Google Maps 2020.

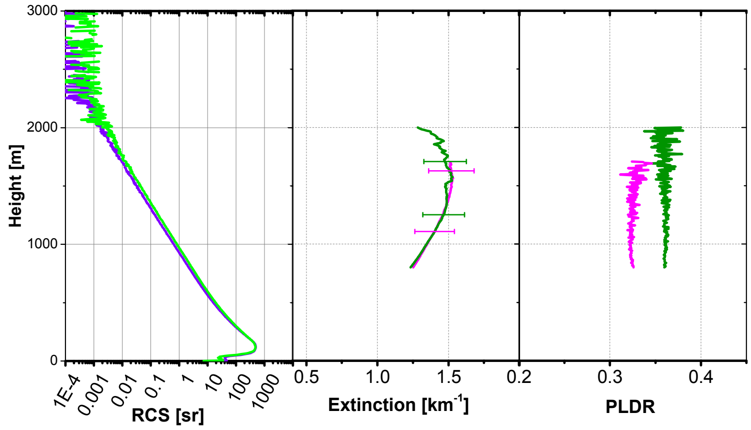

Figure 8. Case 2: Lidar derived parameters at 15:00–24:00 UTC, 24 April 2019. (a) The Raman lidar signals at 530 and 387 nm. (b) The extinction coefficients at 355 and 532 nm. (c) The PLDRs at 355 and 532 nm.

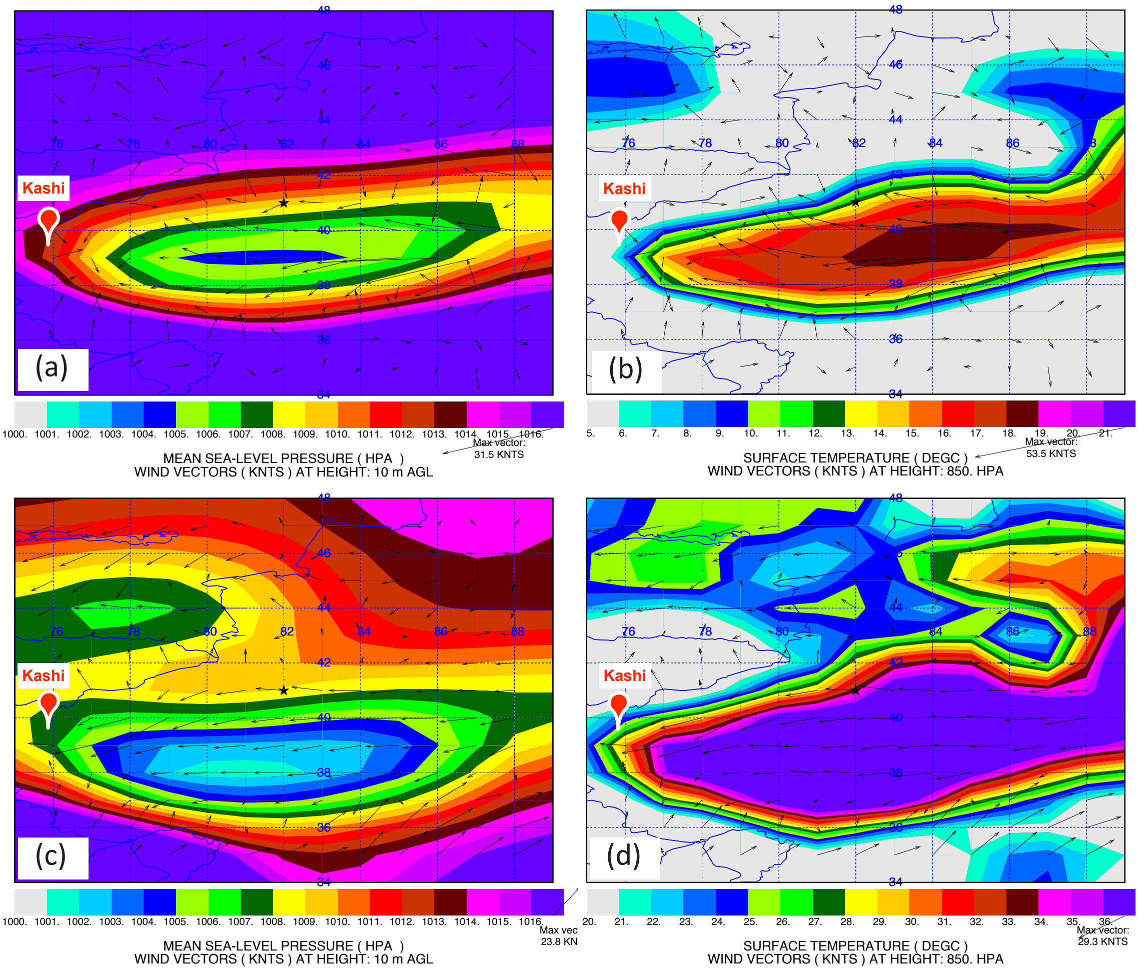

Figure 9. Case 2: The synoptic condition at 00:00 UTC, 23 April (a, b) and 06:00 UTC, 24 April (c, d), 2019. The data are obtained from the 1-degree GDAS archived meteorological data. (a) and (c) The mean sea level pressure at the surface overlaid with wind vector at 10 m above the ground level. (b) and (d) The temperature at 2 m vertical level overlaid with wind vector at 850 hPa vertical level.

B10

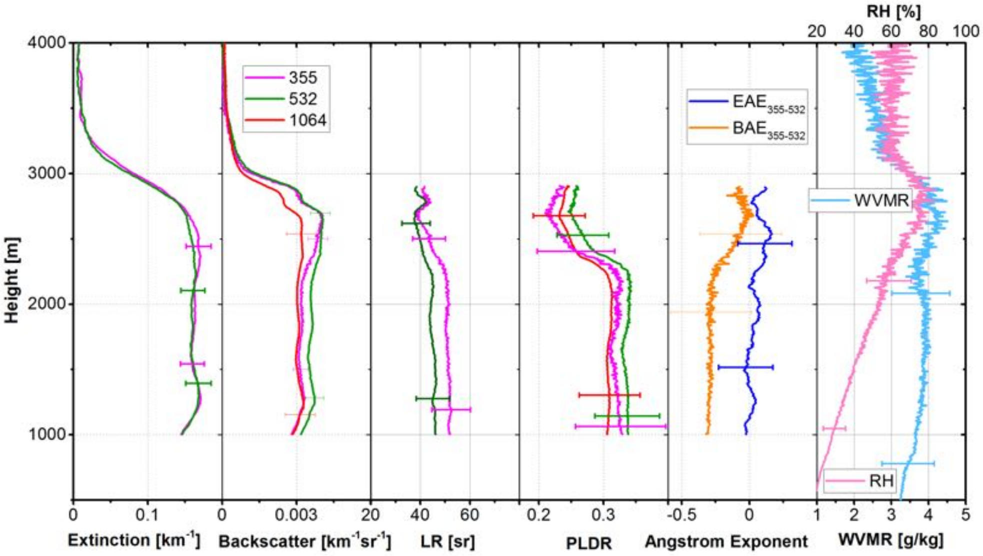

Figure 10. Case 3: Lidar derived parameters at 18:00–20:00 UTC, 15 April 2019. (a) Extinction coefficient, (b) backscattering coefficient, (c) lidar ratio, (d) PLDR, (e) EAE$_{355-532}$ and BAE$_{355-532}$, (f) WVMR and RH.

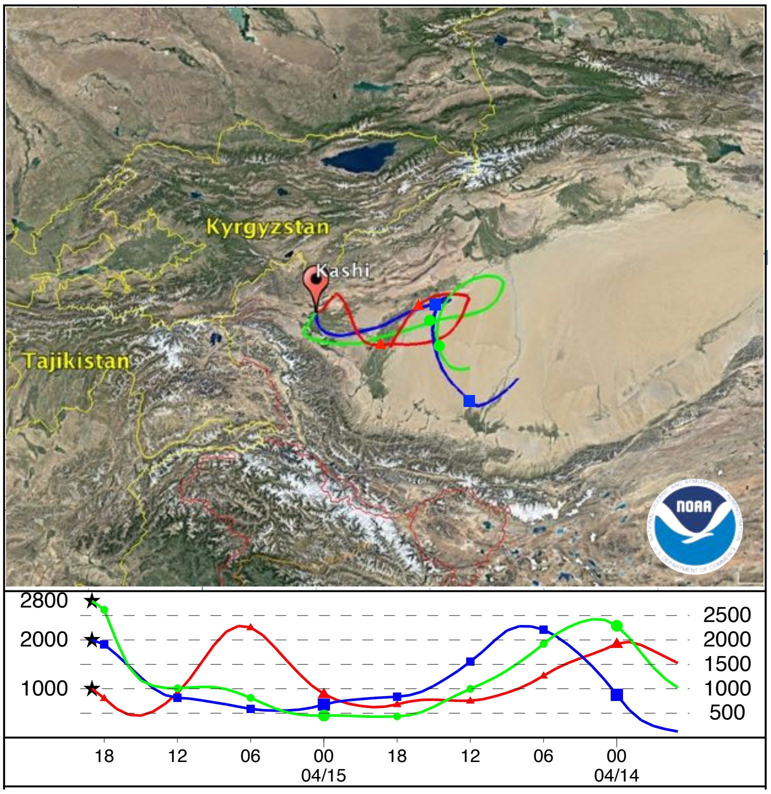

Figure 11. Case 3: The 48-hour back trajectories ending at 19:00 UTC, 15 April 2019 for air mass at 1000, 2000 and 2800 m. @ Google Maps 2020.

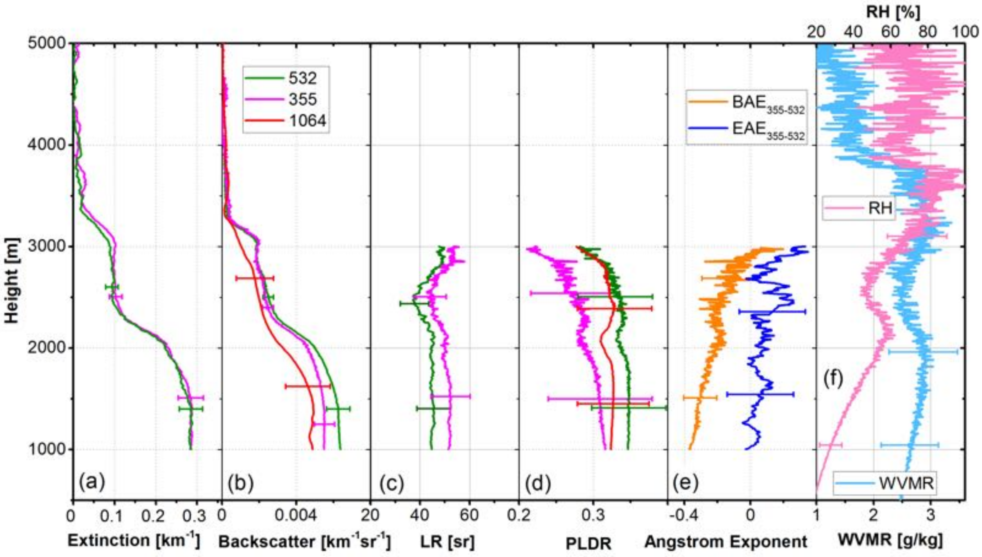

Figure 12. Case 4: Lidar derived parameters at 14:00–16:00 UTC, 03 April 2019. (a) Extinction coefficient, (b) backscattering coefficient, (c) lidar ratio, (d) PLDR, (e) $\text{EAE}_{355-532}$ and $\text{BAE}_{355-532}$, (f) WVMR and RH.

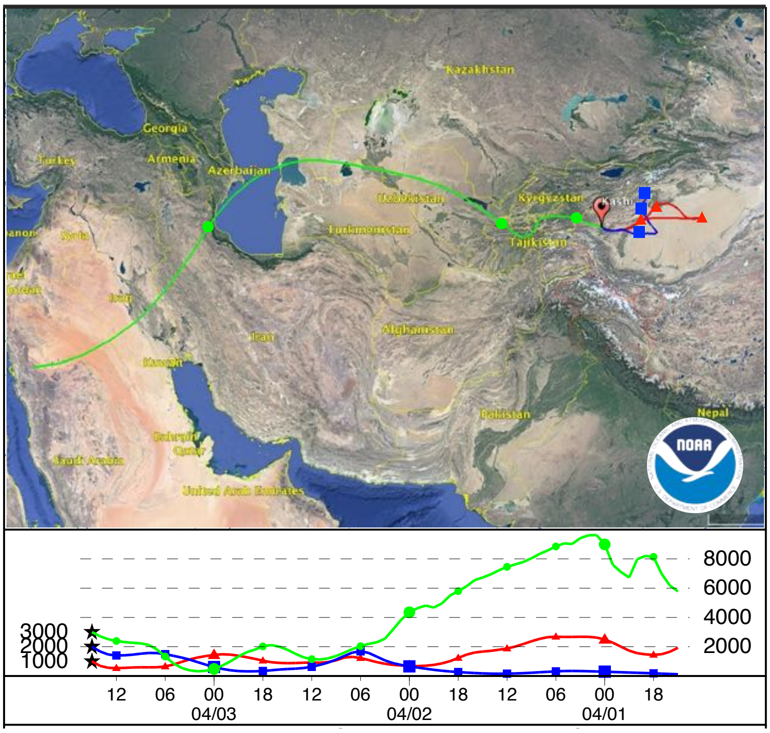

Figure 13. Case 4: The 72-hour back trajectories ending at 15:00 UTC, 03 April 2019 for air mass at 1000, 2000 and 3000 m. @ Google Maps 2020.

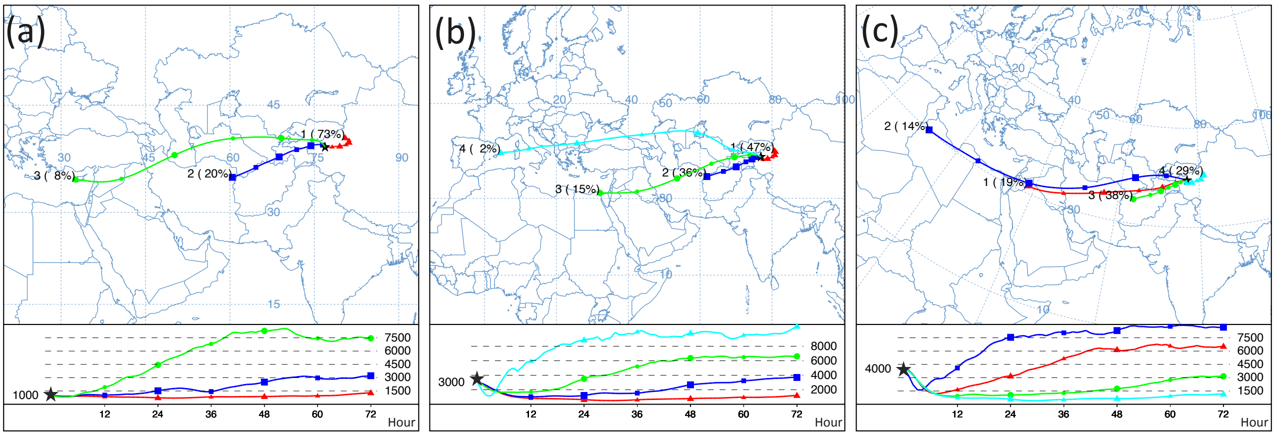

Figure 14. The clustering of air mass in April 2019. The clustering is performed using HYSPLIT and based on back trajectories with a 2-hour time resolution and 72-hour duration. (a) 1000 m, (b) 3000 m, (c) 4000 m.

The characterization of Taklamakan dust properties using a multi-wavelength Raman polarization lidar in Kashi, China

Qiaoyun Hu[1], Haofei Wang[2,4,5], Philippe Goloub[1], Zhengqiang Li[2], Igor Veselovskii[3], Thierry Podvin[1], Kaitao Li[2], and Mikhail Korensky[3]

[1]Univ. Lille, CNRS, UMR 8518 - LOA - Laboratoire d'Optique Atmosphérique, F-59000 Lille, France
[2]State Environmental Protection Key Laboratory of Satellite Remote Sensing, Aerospace Information Research Institute, Chinese Academy of Sciences, Beijing, China
[3]Physics Instrumentation Center of General Physics Institute, Troitsk, Moscow, 142190, Russia
[4]University of Chinese Academy of Sciences, Beijing, 100101, China
[5]Key Laboratory of Radiometric Calibration and Validation for Environmental Satellites, National Satellite Meteorology Center, Beijing, 100081, China

Correspondence: Haofei Wang (wanghf@radi.ac.cn)

Abstract. The Taklamakan desert is an important dust source for the global atmospheric dust budget and a cause of the dust weather in Eastern Asia. The characterization of ~~the properties and vertical distributions of~~ Taklamakan dust in the source region is still very limited. To fill this gap, the DAO (Dust Aerosol Observation) was conducted in April 2019 in Kashi, China~~in 2019.~~. Kashi site is about 150 km to the west rim of the Taklamakan desert and is strongly impacted by desert dust aerosols, especially in spring time, i.e. April and May. ~~Apart from dust, fine particles coming from local anthropogenic emissions or~~According to sun/~~and transported aerosols are also a non-negligible aerosol component.~~ sky photometer measurements, the aerosol optical depth (at 500 nm) varies in the range of 0.07–4.70 and the Ångström Exponent (between 440 and 870 nm) varies in the range of 0.0–0.8 in April 2019. In this study, we provide the first profiling of the $2\alpha+3\beta+3\delta$ ~~lidar profiles~~ parameters of Taklamakan dust based on a multi-wavelength ~~Raman~~ Mie-Raman polarization lidar. ~~Four cases, including two Taklamakan dustevents (Case 1 and 2) and two polluted dust events (Case 3 and 4) are presented. The lidar ratio in the Taklamakan dust outbreak~~ For Taklamakan dust, the Ångström Exponent related to extinction coefficient (EAE, between 355 and 532 nm) is about 0.01±0.30, and the lidar ratio is found to be 45±7 (51±~~8 – 56~~8–56±8~~sr at 355 nm and 45±7 sr at~~) sr at 532 ~~nm~~(355) nm. The particle linear depolarization ratios (PLDRs) are about 0.28~~±0.04~~–0.32±~~0.05~~ 0.07 at 355 nm, ~~0.35~~0.36±0.05 at 532 nm and 0.31±0.05 at 1064 nm. ~~The observed polluted dust is commonly featured with reduced particle linear depolarization ratio and enhanced extinction and backscatter Ångström exponent. In Case 3, the lidar ratio of polluted dust is about 42±6 sr at 355 nm and 40±6 sr at 532 nm. The particles linear depolarization ratios decrease to about 0.25, with a weak spectral dependence. In Case 4, the variability of lidar ratio and particle linear depolarization ratio is higher than in Case 3, which reflects the~~ Both lidar ratios and depolarization ratios are higher than the typical values of Central Asia dust in the literature. The difference is probably linked to the fact that observations in the DAO campaign were collected close to the dust source, therefore, there is a large fraction of coarse-mode and giant particles (radius $> 20\ \mu$m) in the Taklamakan dust. Apart from dust, fine particles coming from local anthropogenic emissions and long-range transported aerosols are also non-negligible aerosol components. The signatures of pollution emerge when dust concentration decreases. The polluted dust (defined by PLDR$_{532}$ $\leq$0.30 and

EAE$_{355-532}$ $\geq$0.20) is featured with reduced PLDRs and enhanced EAE$_{355-532}$ compared with Taklamakan dust. The mean PLDRs of polluted dust generally distributed in the range of 0.20–0.30. Due to the complexity of the nature of ~~mixed pollutant and the mixing state. The results provide~~ the involved pollutants and their mixing state with dust, the lidar ratios exhibit larger variabilities compared with dust. The study provides the first reference ~~for the~~ of novel characteristics of Taklamakan dust measured by ~~Raman~~ Mie-Raman polarization lidar. The data could contribute to complementing the dust model and improving the accuracy of climate modeling.

1 Introduction

Airborne dust is the most abundant aerosol species and accounts for nearly 35% of the total aerosol mass in the atmosphere (Boucher et al., 2013), with an annual flux of ~~$\sim$2000 T yr^{-1} (Textor et al., 2006; Huneeus et al., 2011)~~1000–5000 Tg per year (Engelstaedter et al., 2006; Textor et al., 2006; Huneeus et al., 2011). According to the estimation of Ginoux et al. (2012), about 75% of the atmospheric dust is originated from natural emission and anthropogenic dust emission accounts for $\sim$25%. The area spreading from the Sahara desert, the Arabian Peninsula, Central Asia to East Asia is the most significant natural dust source. Based on model simulations, Tanaka and Chiba (2006) estimated that the Saharan desert contributes to $\sim$62% of the total dust emission and the contribution of Arabian Peninsula, Central Asia and East Asia is about half of the Saharan emission. The dust sources in North and South America, and Australia altogether account for about 25% of total emission. The suspending dust particles can directly influence the planetary radiation budget, and indirectly impact the climate through interfering with cloud properties and cloud process. Dust particles, as well as other ice nucleating particles (INP), can aide the formation of ice crystals in the heterogeneous ice nucleation regime. Due to their effective ice nucleating capability and abundant concentration, mineral dust particles are considered as the most important INP (Kanji et al., 2017). Recent studies found that atmospheric dust is also linked to the activity of tropical cyclones and rainfall (Reed et al., 2019; Thompson et al., 2019).

A comprehensive dataset of dust properties is ~~with~~ of significant importance for understanding the effects of dust in the ecosystem and for reducing the uncertainties of ~~the~~ climate model. However, this task is very challenging and needs the support of ~~observation~~ observational data. The properties of dust particles are determined by the texture of soils, the mineralogical compositions, vegetation cover and surface properties, which could vary globally from location to location. The modeling of dust horizontal and vertical distribution, and dust cycle, i.e. dust emission, transport and deposition, is crucial to ~~the~~ climatic modeling. ~~This work demands also observational data as input and validation.~~ So far, the vertically resolved information can only be obtained from lidar (Light detection and ranging) measurements. A multi-wavelength ~~Raman~~ Mie-Raman polarization aerosol lidar can obtain multiple parameters at a vertical level. This capability makes it ~~an~~ a useful tool for ~~in~~ aerosol study. The profiles of backscatter coefficient, extinction coefficient and depolarization ratio derived from satellite lidar and ground-based lidars have been used as model inputs and have been proved useful for improving the accuracy of model simulation and forecasting (Yumimoto et al., 2008; Campbell et al., 2010; Sekiyama et al., 2010; Wang et al., 2013; Zhang et al., 2011, 2012).

~~Compared with Saharan dust, the characterization of Asian dust is not adequately explored.~~ In Asia, dust sources distribute over a large area and cover different terrain types. The high-elevated bare lands in Iran, Afghanistan and Tajikistan, and the Taklamakan desert in the Tarim basin, the Loess plateau and the Gobi desert in China are the main dust sources. In addition, excessive land-use and human activities ~~could also form new dust source~~formed new dust sources. There are a good number of publications reporting transported Asian dust observed in the downwind countries in East Asian (Liu et al., 2002; Murayama et al., 2004; Huang et al., 2008; Iwasaka et al., 2008). Long-range transported dust can cross the Pacific ocean and occasionally reach America (VanCuren and Cahill, 2002; Uno et al., 2009). However, very few field campaigns have been carried out for Asian dust study. Compared with Saharan dust, the characteristics of Asian dust were not adequately explored. The earliest field campaign characterizing Asian dust date back to 1989, when an experiment was carried out in Tajikistan for studying desert dust properties and the impact on meteorological conditions. The CADEX (Central Asian Dust EXperiment) project was planned to provide a data set of optical and microphysical properties of dust from Central Asia. ~~Within this framework, a~~ A multi-wavelength ~~Raman~~ Mie-Raman polarization lidar was deployed in Dushanbe, Tajikistan. This results in Hofer et al. (2017) and Hofer et al. (2020) provided important dust ~~parameters~~properties, such as vertically resolved lidar ratios, linear depolarization ratios and mass concentrations. In 2002 and 2009, a elastic polarization lidar system (without Raman channel) was set up in Aksu (40.62°N, 80.83°E, in Xinjiang, China) near the north rim of Taklamakan desert (Kai et al., 2008; Jin et al., 2010). Jin et al. (2010) obtained the first lidar ratio of the Taklamakan dust in the source region, however, it requires extra assumptions and supplementary measurements. Sparse lidar observations in the downwind of transported Taklamakan dust have been reported but none of them provides intensive dust characteristics and the observation sites are far from the desert. ~~Hence, a novel and comprehensive data set for the characteristics and vertical distribution of Taklamakan dust is important.~~

In 2019, the DAO (Dust Aerosol Observation) campaign was conducted in April to June in China. This campaign was supported by the "Belt and Road Initiative" and involved researchers from China, France and Russia. The first observation site in the DAO campaign is in Kashi (also called Kashgar) in April 2019, which is about 150 km to the western rim of the Taklamakan desert. The objective of the first session of DAO campaign is to study the characteristics of Taklamakan dust. The second session of the campaign was in Beijing in May and June, for investigating the impact of transported dust on the air quality in megacity. The main topic of this paper is the characterization of Taklamakan dust, therefore, only the measurements in Kashi will be ~~presented~~analyzed. This study is organized into 5 sections. The description of DAO campaign is presented in Section 2, and the results and case study is in Section 3. The discussions and conclusions are presented in Section 4 and 5, respectively.

2 The DAO (Dust Aerosol Observation) campaign

2.1 Overview

The Taklamakan desert is located in the ~~central~~ center of the Tarim Basin in the Uygur Autonomous Region of Xinjiang, China, covering an area of about 320,000 km^2. The mean elevation of the Taklamakan desert is about 1200–1500 m a.s.l (Petrov and S.Alitto, 2019). It is surrounded in three directions by high mountain ranges (see Figure 1). The observation site (39.51°N, 75.93°E, time zone: GMT+08:00) is in the northwest of the Kashi city and close to the border to Tajikistan, Kyrgyzstan and

Afghanistan. Kashi features a desert climate with a big temperature difference between winter and summer. The coldest month is January with average temperature of -10.2–0.3°C and the warmest month is in July with average temperature of 18.6–32.1°C. The annual rainfall in Kashi is about 64 mm. The spring in Kashi is long and comes quickly. The rapidly heated surface sand in the desert could generate ascending currents which ~~result in the~~ could result in frequent dust storm in springtime. This is the main reason that the field campaign was performed in springtime.

Except for desert dust, anthropogenic emission is ~~the other~~ another important aerosol source. There are about 4.65 million habitants (predicted for 2017, see the link) in the Kashi prefecture, including the Kashi city and 11 subordinate counties. Kashi prefecture is a very populated region in Xinjiang with more than 1000 persons per square kilometer in the city center (Doxsey-Whitfield et al., 2015). Fine aerosol particles originated from biomass burning and local anthropogenic emissions, such as heating, traffic and industrial pollution are an important aerosol component. Moreover, there are populated cities in the neighboring countries such as Kyrgyzstan ~~, Tajikistan and Pakistan~~and Tajikistan. Under favorable meteorological conditions, various ~~aerosol~~aerosols, for example, pollution, could be potentially transported to Kashi and mix with dust aerosols.

2.2 Instrumentation and methodology

Lidar system

The multi-wavelength ~~Raman polarization lidar~~ Mie-Raman polarization lidar called LILAS (Lille Lidar Atmosphere Study) is the main instrument installed in observation site. The lidar system ~~, LILAS (Lille Lidar Atmosphere Study)~~ has been operated in LOA (Laboratoire d’Optique Atmosphérique, Lille, France) since 2013 (Bovchaliuk et al., 2016; Veselovskii et al., 2016; Hu et al., 2019). During the DAO campaign, LILAS was transported from Lille to Kashi (and Beijing in the second session of the campaign) to perform observations. LILAS uses a Nd: YAG laser that emits at three wavelengths: 355, 532 and 1064 nm. The laser repetition rate is 20 Hz. A Glan prism is used to clean the polarization of the laser beam. The emitting power after the Glan prism is about 70, 90 and 100 mJ at 355, 532 and 1064 nm, respectively. LILAS system has three Raman channels, including 387 (vibrational-rotational), 530 (rotational) and 408 nm (water vapor). The use of rotational Raman at 530 nm provides a stronger Raman signal and relieves the dependence of the derived extinction and backscatter coefficients on the assumption of Ångström exponent (Veselovskii et al., 2015). The backscattered light is collected ~~using~~ by a 400 mm Newton telescope. The incomplete overlap range of LILAS system is about 1000–1500 m in distance, depending on the selected field of view angle. In the receiving optics, the three elastic channels are equipped with both a perpendicular and a parallel channel with respect to the polarization plane of the emitted linearly polarized laser light, in order to measure the linear depolarization ratio at three wavelengths. ~~The~~ LILAS can provide the profiles of the 2α+3β+3δ (α: extinction coefficient, β: backscatter coefficient, δ: particle linear depolarization ratio (PLDR)) parameters. Benefited from the coupled Raman channels, the extinction and backscatter coefficients at 355 and 532 nm are calculated using the Raman method proposed by Ansmann et al. (1992). The Raman signal generated by the radiation at 1064 nm is not measured by LILAS, thereby Raman method is not applicable. The backscatter coefficient at 1064 nm is calculated using the Klett method, where a vertically constant lidar ratio (extinction-to-backscatter ratio) is assumed (Klett, 1985). The particle linear depolarization ratios are derived from Equation 1:

$$\delta^p = \frac{(1+\delta^m)\delta^v R - (1+\delta^v)\delta^m}{(1+\delta^m)R - (1+\delta^v)}, \tag{1}$$

where R represents the ratio of the total backscatter coefficient, involving molecules and particles, to the particle backscatter coefficient. δ^m represents the molecular depolarization ratio. δ^v represents the volume linear depolarization ratio (VLDR), which equals to the calibration coefficient multiplied by the ratio of the signal of the perpendicular channel to the parallel channel. The polarization calibration is performed following the ±45° method (Freudenthaler et al., 2009). During the DAO campaign, the polarization calibration has been performed at least once per day. ~~LILAS can provide the profiles of the 2α+3β+3δ (2 extinction coefficients + 3 backscatter coefficients + 3 particle linear depolarization ratios) parameters.~~

The Ångström exponent of the extinction coefficient and backscatter coefficient are calculated by the Equation 2:

$$\mathring{A} = -\frac{\log p(\lambda_1) - \log p(\lambda_2)}{\log \lambda_1 - \log \lambda_2} \tag{2}$$

where $p(\lambda)$ represents the optical parameters, such as AOD, extinction or backscatter coefficient at wavelength λ, $\mathring{A}$ represents the Ångström exponent of the corresponding parameters $p(\lambda)$. The statistical error of lidar derived parameters is estimated ~~to be 10% for the~~ using the method presented in Hu et al. (2019). The data presented in this study are recorded in nighttime, so the background radiation is negligible. The error in the extinction and backscatter coefficient ~~, and~~ is about 10%, which leads to about 15% ~~for~~ of error in the lidar ratios~~and particle linear depolarization ratios. The errors for the water vapor mixing ratio and relative humidity are~~ , at 355 and 532 nm. The error in the backscatter coefficient at 1064 nm is about 20%. The ~~other error sources, such as alignment of laser beam and errors in the selection of reference, are not considered in the~~ error ~~estimate.~~ in PLDR is calculated in terms of the backscatter ratio, VLDR and molecular depolarization ratio. For the data presented in this study, the error in PLDR is no greater than 15% at 532 and 1064 nm. Therefore, we conservatively use 15% as the error in PLDR for 532 and 1064 nm. At 355 nm, the error of 15% still holds when dust concentration is high enough, but when the concentration drops, the error could exceed 15%. In the case study, errors at 355 nm are calculated separately. The errors for the water vapor mixing ratio (WVMR) and relative humidity (RH) are about 20%.

Sun/sky photometer

Three sun/sky photometers are deployed in the Kashi observation site. One is affiliated to the AERONET (AErosol RObotic NETwork, Holben et al. (1998)) network and the other two are affiliated to SONET (Sun-Sky Radiometer Observation Network). SONET is a ground-based sun/photometer network with the extension of multi-wavelength polarization measurement capability to provide long-term columnar atmospheric aerosol properties over China (Li et al., 2018). The three sun/sky photometers provide complementary measurements by following different measurement protocols. In all, they can measure daytime aerosol optical depth (denoted as AOD hereafter) at 340, 380, 440, 675, 870, 1020 and 1640 nm, polarized/unpolarized sky radiances at 440, 675, 870 and 1020 nm and moon AOD as well. The succeeding data treatment and retrieval are performed following the protocols and standards of AERONET or SONET, depending on the affiliation of the instruments.

Satellite data

Satellite data have complementary advantages due to their large spatial coverage compared ~~to~~ with ground-based remote sensing technique. In order to ~~show the activity of the~~ monitor dust activities of the Taklamakan desert, we use the UV aerosol index (UVAI hereafter) derived from the OMPS (Ozone Mapping Profiler Suite) onboard the Suomi-NPP (National Polar-orbiting Partnership) satellite (Flynn et al., 2004; Seftor et al., 2014). OMPS provides full daily coverage data and the overpass time for Kashi region is around 06:30 UTC. The UVAI is calculated using the signal in the 340 and 380 nm channels (Hsu et al., 1999):

$$\mathrm{UVAI} = -100 \times \left\{ \log_{10} \left[\frac{I_{340}}{I_{380}}\right]_{meas} - \log_{10} \left[\frac{I_{340}}{I_{380}}\right]_{calc} \right\}, \tag{3}$$

where ~~$I_{...}$ represents~~ I_{340} and I_{380} represent the backscattered radiance at ~~corresponding wavelength~~340 and 380 nm. The subscripts "meas" and "calc" respectively represent the real measurements and model simulation in a pure Rayleigh atmosphere. By the definition of UVAI, its positive values correspond to UV-absorptive aerosols such as desert dust and carbonaceous aerosols. Hence, the UVAI from OMPS is a good parameter for monitoring the activity of the Taklamakan desert.

Auxiliary data

A radiosonde station (39.47°N, 75.99°N) in Kashi is 6 km to the observation site. The data are accessible on the website of the Wyoming weather data website (see the link). The radio sounding data are recorded at 00:00 and 12:00 every day at local time. They provide the vertical temperature and pressure profiles for the calculation of molecule scattering parameters in lidar data processing. The HYSPLIT (Hybrid Single-Particle Lagrangian Integrated Trajectory, Stein et al. (2015); Rolph et al. (2017)) model developed by the National Oceanic and Atmospheric Administration (NOAA) Air Resources Laboratory is used for the back trajectory of the air mass and for the air mass clustering. The HYSPLIT model is driven by the 0.5° gridded GDAS (Global Data Assimilation System) data and could produce the transport pathways of the air mass at different vertical levels. Besides, instruments measuring particulate matter (PM10 and PM2.5), gas concentration (SO2, O3 and NOx), particle size distribution, particle scattering and absorption coefficients, solar radiation and a cloud monitor are also deployed in the field campaign. These data contribute to relevant air quality and solar radiation studies within the frame of the DAO campaign.

3 Results and analysis

3.1 Overview

Figure 2 presents the monthly averaged AOD at 500 nm, Ångström exponent between 440 and 870 nm and the FMF (fine mode fraction, the fraction of fine mode AOD to total AOD) in Kashi site from 2013 to 2017. The data are derived from SONET network. The highest AOD occurs in spring, i.e. March and April, while the lowest values occur in summer time, i.e. June and July. The Ångström exponent is positively correlated to the FMF and negatively correlated to the AOD. The lowest mean Ångstöm exponent occurs in March and April, indicating that dust particles are dominant due to the seasonal increase of dust activities in this period (Littmann, 1991; Qian et al., 2002). In December and January, the Ångström exponent and FMF increase significantly, which proves that fine particles are an important aerosol ~~source in Kashi. The fine particles are mostly originated from heating, biomass burning, traffic and industrial pollution in the local area.~~component in winter.

Figure 3(a) plots the AOD at 500 nm and the Ångström exponent measured during the DAO campaign in April 2019. The AOD varies from 0.07 to 4.70 and the Ångström exponent varies from 0.0 to 0.8. For AOD greater than 0.2, ~~there is a high possibility that~~ the corresponding Ångström exponent mostly falls into the range of 0.0 to 0.2. While for AOD lower than 0.2, the Ångström exponent is mostly between 0.3 to 0.7. The negative correlation between the AOD and the Ångström exponent indicates that coarse particles are the main cause for the increase of AOD. This argument is supported by the variation of the particulate matter plotted in Figure 3(b).

We select four representative cases from the nearly 1 month lidar observations. The four cases are recorded on 03, 09, 15 and 24 April 2019. In order to distinguish "pure" Taklamakan dust observations, we define Taklamakan dust by EAE$_{355-532}$ (Ångström exponent related to extinction coefficient) smaller than 0.1 and PLDR$_{532}$ greater than 0.32 at 532 nm. Polluted dust is defined with PLDR smaller than 0.30 at 532 nm and EAE no smaller than 0.2. Back trajectories are also used as a reference for identifying the aerosol origins. The maps of UVAI are plotted in Figure 4. On 09 and 24 April, intense aerosol plumes were observed over the Taklamakan desert. One extreme dust event occurred on 24 April when the AOD (at 500 nm) reached about 4.70 at 08:40 UTC, with instantaneous Ångström exponent about -0.02 and the visibility about 1 km (see the link). The PM10 increased to the monthly maximum on 24 April, reaching nearly 1500 μg/m^3. ~~High aerosol content makes the cloud screening difficult, so~~ It should be noted that, in this extreme case where AOD reached 4.70, the accuracy of the measured AOD ~~might degrade due to uncertain cloud contamination~~may degrade because of the decreasing signal-to-noise ratio. Moreover, weak incoming solar radiation might disturb the performance of the cloud screening in the quality control procedure, thus disabling the discrimination of cloud contaminated and non-contaminated measurements. On 03 and 15 April, the activity of the Taklamakan desert became less intense compared ~~to~~ with the first two cases. The concentration of dust particles ~~decrease~~ decreased and the features of polluted dust ~~appear~~appeared. Lidar quicklooks at 532 nm for the four cases are plotted in Figure 5.

3.2 Case studies

3.2.1 Case 1: 09 April 2019

Dust plumes over the Taklamakan desert are detected on 07, 08 and 09 April, as shown in Figure 4. The most intense plume in the three days appeared on 07 April, with maximum UVAI about 4.0. On 09 April, a belt-like plume appeared in the north and northwest of the desert. Figure 5(b) shows the range-corrected lidar signal at 532 nm collected between 9 and 10 April. The boundary layer height slightly increases from 3000 m to 4000 m in the night, and strong backscattered lidar signal is seen below 2000 m. Figure 6 shows the profiles of the optical properties, ~~water vapor mixing ratio (WVMR) and relative humidity (RH)~~ WVMR and RH averaged between 17:00 and 22:00 UTC, 09 April 2019. The extinction coefficients ~~generally~~ gradually decrease with height. At 1000 m, the extinction coefficients are greater than 0.5 km^{-1} and remain almost stable below 2000 m. The RH is no more than 40±8% below 2000 m and rises to 60±12% at 3800 m. The lidar ratio varies between 40±6 and

48±7 sr at 532 nm and between 55±8 and 62±9 sr at 355 nm. The ~~particle linear depolarization ratio (PLDR)~~ PLDR is about 0.32±0.05 at 355 nm and 0.36±0.05 at 532 nm. The ~~volume linear depolarization ratio (VLDR)~~ VLDR at 1064 nm is about 0.32±0.03. The backscatter coefficient, as well as the PLDR at 1064 nm is not available above 1800 m, ~~due to the distortion of 1064~~ since the1064 nm lidar signal ~~caused by the high concentration of dust particles.~~ has distorted in upper boundary layer. We can expect that the VLDR is approximate to PLDR at 1064 nm under ~~this condition, since~~ in this case, because the dust content is so high that molecular scattering at 1064 nm can be neglected. The EAE$_{355-532}$ is about -0.10±0.30 at 800 m and rises to 0.10±0.30 at 3800 m. The BAE$_{355-532}$ (Ångström exponent ~~of backscatter coefficient(BAE$_{355-532}$~~related to backscatter coefficient) is negative and varies from -0.7±0.3 to -0.4±0.3. Below 3000 m, the lidar ratios mildly decrease with height, while the PLDRs do not show obvious vertical variations. Above 3000 m, the vertical variations in the lidar ratios and PLDRs become more significant. The vertical variations of the lidar ratios and PLDRs are possibly the result of particle sedimentation or/and vertically dependent particle origins.

On 09 April, the Taklamakan desert ~~is~~ was covered by a low-pressure zone with easterly and northeasterly wind prevailing over the western part of the desert. It is a favorable condition for the elevation of dust particles. Figure 7 shows the 48-hour back trajectory ending at 20:00 UTC for air mass at 1000, 2000 and 3000 m. The air masses at the three vertical levels are originated from the Taklamakan desert. They all passed over the area where dust plumes have been observed and then diverged when approaching the rim of the desert. In the end, the air masses at 1000, 2000 and 3000 m arrived at the observation site from the northeast, east and southeast respectively~~, after being lifted from~~ . The particles observed by LILAS on 09 April are fresh desert dust, without long-range transport. Therefore, they could contain a large fraction of coarse-mode particles especially giant particles (radius> 20 μm). Moreover, the back trajectories in Figure 7 shows convective strong air flows arising from below 500 m to 3000 m within 3 hours, suggesting the possibility of lifting large particles near the surface to higher levels.

3.2.2 Case 2: 24 April 2019

On 24 April, the observation site was enclosed by floating dust. In the daytime, the sky radiance dropped below the detection limit of the sun/sky photometer, so the AERONET and SONET retrieval can not be applied. A large and intense plume was first detected in the morning of 23 April 2019 (Figure 4). ~~And on~~ On 24 April, a hot spot of UVAI appeared over the observation site. The daily average of AOD is 3.63 and Ångström exponent is about -0.01, according to the daytime sun/sky photometer measurements. The lidar quicklook on 24 April in Figure 5 shows that the boundary layer height rises from about 1200 m to 2000 m from 14:00 to 24:00 UTC. Due to the high dust attenuation in the boundary layer, both sun/sky photometer and lidar cannot detect whether clouds exist on 24 April. Figure 8 plots the averaged parameters between 15:00–24:00 UTC, 24 April 2019. The dust layer was so thick that the laser beam can not penetrate. The amplitude of Raman signal dropped by 5–6 orders in the lower 2000 m. In this condition, we can not find ~~a~~ an aerosol-free zone to for the calibration of lidar signal, therefore, the calculation of the backscatter coefficient using Raman method is not possible. But the extinction coefficient can be derived from the Raman signal (Ansmann et al., 1992). The extinction coefficients are 1.0±0.1 km^{-1} at 800 m and increases to about 1.5±0.2 km $^{-1}$ at 1500 m. The extinction coefficient at 355 nm is removed at above 1500 m because it starts to oscillate due to insufficient signal-to-noise ratio. The extinction coefficient at 532 nm decreases to about 1.1±0.1 km^{-1} at 2000 m. By assuming that the lidar ratios are about 55 sr and 45 sr at 355 and 532 nm, respectively, we obtain the backscatter coefficient from the extinction coefficient, and then calculate the PLDRs (in Figure 8(c)). The PLDR is about 0.32 at 355 nm and 0.37 at 532 nm, which are rather consistent with the results in Case 1. The uncertainties of the PLDRs are not accessible because the uncertainties of the assumption of lidar ratio are not known.

The back trajectories (not shown) indicates that dust particles (at 1000 and 2000 m) are originated from the northeast and east, where intense dust plumes were observed on 23 and 24 April. Figure 9 shows synoptic conditions at 00:00 UTC, 23 April and 06:00 UTC, 24 April. The meteorological conditions on 23 and 24 April are favorable for dust emission, similar to Case 1. The Taklamakan desert is enclosed by a low-pressure zone (Figs. 9(a) and (c)). The plume observed by OMPS on 23 April was probably lofted in the local morning. In the eastern part of the Taklamakan desert, 37–39°N, 83–88°E, the wind velocity at 10 m (a.g.l) reaches more than 50 km/h (Figure. 9(a)) and at 850 hPa level the maximum wind velocity reaches 90 km/h (Figure. 9(b)). The high wind velocity near the surface and large vertical wind gradient help elevate dust particles from the surface into the atmosphere. On 23 and 24 April, easterly and northeasterly wind are prevailing in the desert region, thus blowing the lifted dust particles to the observation site. Case 2 is a more severe manifestation of Case 1 regarding the intensity of the dust loading. In both cases, the observed dust particles are originated from nearby dust source. Compared with typical depolarization ratios in worldwide dust observations, which are 0.23-0.30 at 355 nm and 0.30-0.35 at 532 nm, the depolarization ratios we obtained in the two cases are relatively higher (Veselovskii et al., 2016; Freudenthaler et al., 2009; Hofer et al., 2017, 2020). While previous observation sites were mostly not as close to the dust source as in our campaign, the differences are probably due to the fraction of coarse-mode particles that remain in our dust observation. Burton et al. (2015) also observed dust particles near the source in North America and reported PLDR of 0.37 at 532 nm, which is consistent with our result. However, the PLDR at 355 nm measured by Burton et al. (2015) is about 0.24, lower than what we obtained.

3.2.3 Case 3: 15 April 2019

~~The~~ On 15 April, the daily mean AOD on 15 April was 0.63 ~~,~~ and the Ångström exponent was about 0.10. Compared ~~to~~ with the previous two cases, the Ångström exponent increase obviously. The boundary layer height started to increase at 15:00 UTC and stayed at 3500 m in the night of 15 April. Cirrus clouds were continuously present during the period of lidar measurement (Figure 5(c)). The lidar derived ~~parameters~~ profiles between 18:00–20:00 UTC are plotted in Figure 10. The extinction coefficients in the boundary layer are about 0.15 km^{-1} and decrease to almost zero at 3500 m. The RH increases up to 60±12% at 2200 m. Below this height, the lidar ratio, PLDR, EAE and BAE are almost stable. The lidar ratio is about 51±8 sr at 355 nm and 45±7 sr at 532 nm. The PLDRs at 355, 532 and 1064 nm are around 0.32±~~0.05~~0.07, 0.34±0.05 and 0.31±0.05, respectively. The EAE$_{355-532}$ is about 0.02±0.30, showing a gentle increase with height, and the BAE$_{355-532}$ is about -0.29±0.30. Above 2200 m, the RH starts to increase and reaches its maximum, i.e. 80±16%, at 2800 m. The EAE$_{355-532}$ and BAE$_{355-532}$ increase to 0.10±0.30 and -0.06±0.30, respectively. On contrary, the lidar ratios and PLDRs decrease and reach ~~the minimum~~ their minima at about 2800 m. The lidar ratio is about 40±6 sr at 2400–2800 m, with a weak spectral dependence, and the PLDRs are about 0.23±~~0.03~~ 0.06 at 355 nm, 0.26±0.04 at 532 nm and 0.24±0.03 at 1064 nm. It should be noticed that the backscatter coefficient at 1064 nm is performed using Klett method with an assumption of lidar ratio equal to 40 sr (Klett, 1985).

Dust activities were observed by the OMPS on 13 and 15 April 2019 (Figure 4), while the intensity was less stronger than in Case 1 and 2 and the distance between the dust plume and the observation site is farther. The 48-hour back trajectories ending at 19:00 UTC are shown in Figure 11. Air masses at the three vertical levels (1000, 2000 and 3000 m) are originated from the eastern part of the Taklamakan desert, where no intense dust activities have been observed by OMPS in the recent three days. It explains the decrease of dust content in the boundary layer. When dust loading decreases, the impact of fine mode particles emerges. The changes of EAE, BAE, PLDR and lidar ratios above 2200 m ~~is~~ are a clear evidence of polluted dust. The pollution could be lifted up from the ground in local area by convection or be transported from other area. Additionally, the RH at above 2500 m is about 60±12%–80±16%, which could lead to the hygroscopic growth of some aerosol species. Pure dust is regarded as hydrophobic aerosols because its compounds are insoluble, but when ~~coated by~~ mixed with hygroscopic aerosol species, for example, nitrate, the ~~polluted dust~~ ensemble of aerosol mixture could become hygroscopic. The fine mode particles can be hydrophobic or hydroscopic, depending on their chemical compositions(Carrico et al., 2003; Shi et al., 2008; Pan et al., 2009). In this case, there were no clear evidence indicating the occurrence of hygroscopic growth ~~is not evident~~or the mixing state of dust and pollution particles.

3.2.4 Case 4: 03 April 2019

The daily mean AOD on 03 April is 0.16 and the Ångström exponent is about 0.11. The boundary layer height is about 3000 to 4000 m, rising slightly in the night of 03–04 April. Starting from 16:30 UTC, some liquid cloud layers occurred at the top of the boundary layer (Figure 5(a)). Figure 12 shows the profiles derived from lidar observations at 14:00–16:00 UTC, 03 April. The extinction coefficients decrease from about 0.28±0.03 km^{-1} at 1000 m to about 0.10±0.01 km^{-1} at 3000 m, with $\mathrm{EAE}_{355-532}$ ($\mathrm{BAE}_{355-532}$) increasing from 0.01±0.30 (-0.38±0.3) to 0.28±0.30 (0.02±0.30). Below 2100 m, the lidar ratios are about 45±7 sr at 532 nm and 51±8 sr at 355 nm. The PLDRs are about 0.35±0.05 at 532 nm and 0.32±0.05 at 1064 nm and 0.28±~~0.04~~–0.32±~~0.05~~ 0.07 at 355 nm. Between 2100 and 3000 m, the variation of lidar ratios is not monotonic. At 2500 m, the lidar ratios reach the minimum of 38 ± 6 sr at 532 nm and 42 ± 6 sr at 355 nm~~. The lidar ratios , $\mathrm{BAE}_{355-532}$ and $\mathrm{EAE}_{355-532}$ at this height all coincide well with the values at the boundary layer top in Case 3, which suggests the presence of polluted dust particles in Case 4.~~ , and the PLDRs are about 0.27±0.06 at 355 nm and 0.33±0.05 at 532 nm. Both the lidar ratios and PLDRs at 2400-2800 m range are very consistent with the properties of Central Asia dust reported by Hofer et al. (2017) and Hofer et al. (2020). Above 2500 m, the lidar ratios and the RH (~~also the~~ as well as WVMR) re-increase, ~~with the PLDRs decreasing. These signs may suggest the existence of a different aerosol types between 2500 and~~ and PLDRs decrease. At 3000 ~~m~~m, the PLDR at 532 nm drops below 0.30, suggesting that aerosols are different from those at lower boundary layer. The signatures of lidar ratio, RH and PLDR are possibly linked to the occurrence of polluted dust particles. In addition, long-range transported dust could also possess such PLDRs due to the deposition of big particles in the transport. This case is classified as polluted dust because the PLDR below 0.30 at 532 nm, the increase of WVMR (as well as RH) and $\mathrm{EAE}_{355-532}$) at the boundary layer top fit better the characteristics of polluted dust.

Figure 13 plots the 72-hour back trajectories for 1000, 2000 and 3000 m. Air masses at 1000 and 2000 m are from the Taklamakan desert, while the air mass at 3000 m is from Central Asia. It corroborates the similarities of the lidar ratios and PLDRs between the measurements in Hofer's studies and in our study. When extending the trajectory duration to 96 hours, the results (not plotted) suggest that air mass at 3000 m is originated from North Africa. This ~~finding~~ result suggests that dust particles observed in Kashi may have a ~~proportion of~~ long-transported aerosol component. The air mass clustering based on 24-hour back trajectories (not shown) indicates that about 52% of air mass at 3000 m is from North Africa and Arabian Peninsula. At 3500 m, this proportion increases to 74% and there is also a fraction of air mass coming from Europe. ~~In the long transport pathway, aerosol properties could modify due to deposition and mixing with various aerosols. Hence, the complexity~~ The complexity in the aerosol sources in the transport pathways explains the variability of aerosol properties at ~~the boundary layer top is difficult to be resolved.~~ upper boundary layer in Case 4.

4 Discussion

Aerosol source

The optical parameters in the 4 cases are summarized in Table 2. ~~In order to distinguish Taklamakan dust observations, we define Taklamakan dust by EAE$_{355-532}$ smaller than 0.1 and PLDR$_{532}$ greater than 0.32 at 532 nm. Back trajectories are also used as a reference for identifying the aerosol origins. The observations falling beyond this category are classified as polluted dust.~~ ~~**Aerosol source**~~~~The coarse-mode dust and fine-mode particles originated from anthropogenic emission or transport are the two important aerosol components in Kashi.~~ During the campaign, dust is undoubtedly the predominant component. In ~~the dust storms~~ dust events (Case 1 and Case 2), dust particles are lifted from the Taklamakan desert by the low-pressure system along with strong wind, and then blown to the observation site by the easterly or northeasterly wind. In dry deposition, coarse-mode particles, especially giant particles settle down faster than the fine-mode dust particles. In many previous campaigns, the observed dust particles have undergone long-range transport, ranging from several hundreds or thousands kilometers (Dieudonné et al., 2015; Murayama et al., 2004; Veselovskii et al., 2016; Ansmann et al., 2003; Haarig et al., 2017; . While the transport distance is much shorter in DAO campaign. Thus, the observed dust particles in DAO campaign are more likely to contain a large fraction of coarse-mode and giant particles, which is an important difference of our observations compared with most previous observations. Moreover, the mineral composition of dust is size-dependent. In the study of Saharan dust, Kandler et al. (2009, 2011) found a tendency of higher quartz content in larger particles, but a significant fraction of sulfate was found in the size range smaller than 1 μm. The iron-bearing minerals, which is linked to the dust absorption, are more concentrated in the fraction with radius smaller than 2.0 μm. The difference in the size distribution could lead to a difference in mineralogical composition and chemical properties (Ryder et al., 2018; Biagio et al., 2019).

The influence of pollution is not clearly seen in the dust storms. However, when the activities of the Taklamakan desert wane and dust concentration becomes lower, the impact of pollution emerges. Observations in Case 3 ~~and 4~~ clearly demonstrate the contrast of dust in the lower boundary layer and polluted dust particles at the boundary layer top. During the 1-month campaign, the traces of pollution, featured with increased EAE$_{355-532}$ and decreased PLDRs are frequently observed. The evidence of pollution in Taklamakan dust has been found in previous in-situ measurements. Huang et al. (2010) sampled aerosol particles in springtime at Tazhong site, which is located in the north rim of Taklamakan desert, and found that the As element was moderately enriched. The As element is a tracer of pollution, originated probably from coal burning. It is also found that the concentration of sulfate in Taklamakan dust is at a high level. The increased concentration of sulfate in the Taklamakan dust could be related to the provenance of the Taklamakan desert, because it is speculated to be ocean 5–7 millions years ago (Sun and Liu, 2006). Sulfate could also come from anthropogenic emission, for example, the uptake of the SO2 gases. Iwasaka et al. (2003) examined the aerosol samples ~~by the~~ using electron microscopy in Dunhuang, China, which is in the downwind of transported Taklamakan dust. They found that mineral dust is the main component in the coarse-mode aerosols, while in the fine mode, ammonia sulfate, which is mainly from anthropogenic emissions, is the major component. These studies indicate that the Taklamakan dust near the source region have been contaminated by other ~~aerosol species~~ aerosols with anthropogenic origins. It is in agreement with our ~~conclusion~~analysis, however, in this study we cannot clarify the exact ~~involving~~ involved aerosol species and the mixing state in the polluted dust. In our study, polluted dust mostly appeared at the boundary layer top, which agrees with the finding of Iwasaka et al. (2003). These fine particles are possibly lifted by convective air flow and ~~concentrate~~ then remain at higher altitude as bigger particles settle down.~~The mixing of mineral dust with these aerosol species can modify their properties of light scattering, hygroscopic properties and interfere the cloud process (Kojima et al., 2006; Fan et al., 2016) .~~

Long-range transported aerosols are another possible aerosol ~~source~~ origin in Kashi. Based on model simulations, some previous studies have reported intercontinental dust transport from North Africa or the Middle East to the East Asia (Park et al., 2005; Tanaka et al., 2005; Sugimoto et al., 2019). Figure 14 plots the air mass clustering for three different vertical levels in April 2019. The contribution of air masses from ~~the west, such as~~ Central Asia, Middle East, Europe and North Africa always exists and the influence increases with height. At 1000 m, the main aerosol source is from the Taklamakan ~~region~~ desert and accounts for ~~only~~ about 73%. At 3000 m, air mass from Central Asia, Middle East and North Africa accounts for about 51%, and there is about 2% of air mass from Europe. While at 4000 m, air mass from the Taklamakan occupies only 29% and the rest are from Central Asia, the Middle East and North Africa. The west-to-east airmass transport ~~are~~ is associated with the mid-latitude westerlies, which is a continuous force for air mass transport (Yumimoto et al., 2009; Yu et al., 2019). ~~There~~ In Case 4, we observed dust signatures that differ from Taklamakan dust but correspond well with the results from Hofer et al. (2017) and Hofer et al. (2020) in Dushanbe. Nevertheless, there are various aerosol sources in the intercontinental transport pathway, such as ~~Saharan~~ dust from North Africa, Middle East and Central Asia, pollution and biomass burning from East Europe. ~~And~~ Moreover, the aerosol properties could be modified during the transport. Hence, it is difficult to find out the exact ~~aerosols brought to the site~~aerosol types using lidar observations.

Lidar ratio and depolarization ratio

We found that, for Taklamakan dust, the lidar ratios are about 45±7 sr at 532 nm and 51–56±8 sr at 355 nm. The PLDRs are about 0.28–0.32±~~0.05~~ 0.07 at 355 nm, ~~0.35~~0.36±0.05 at 532 nm and 0.31±0.05 at 1064 nm. ~~Polluted dust in Case 3 has lidar ratio of about 42±6 sr at 355 nm and 40±6 sr at 532 nm; and PLDR of about 0.23±0.03, 0.26±0.03 and 0.24±0.03~~

~~at 355, 532 and 1064 nm, respectively. In Case 4, the lidar ratio of polluted dust varies non-monotonically in the range of 43±6 to 57±8 sr at 355 nm and 38±6 to 49± 8 sr at 532 nm. The PLDRs vary in the range of 0.21±0.03–0.29±0.04 at 355 nm, 0.28±0.04–0.34±0.05 at 532 nm, and 0.28±0.04–0.33±0.05 at 1064 nm.~~ Table 3 presents an overview of the lidar ratios and PLDRs of Asian~~dust, Saharan dust~~, Saharan and American dust in previous publications. Jin et al. (2010) derived a lidar ratio of 42±3 sr at 532 nm for Taklamakan dust, which agrees well with our results. The observation site in Jin et al. (2010) was very close to Kashi, however, their results were based on the observations of an elastic lidar, so it requires the assumption of vertically independent lidar ratio and complementary measurements. ~~Hofer et al. (2017) reported lidar ratios (PLDRs) of 47±2 sr (0.23±0.01) at 355 nm and 43±3 sr(0.35±0.01) at 532 nm, based on Raman lidar observations in Dushanbe (Tajikistan) on 8 August 2015. Dieudonné et al. (2015) obtained similar results (at 355 nm) in Kazan and Omsk (Russia) for dust originated from the Caspian sea and the Aral sea. Murayama et al. (2004) observed transported Asian dust in Japan and derived lidar ratio about 49 sr at 355 and 43 sr at 532 nm. A special case is on 14 July 2016 in Hofer et al. (2017) when an extreme dust event was observed. The lidar ratios (PLDRs) were estimated to be 40±1 sr (0.29±0.01~~Observations obtained from other Asian sites show mean lidar ratio in the range of 40–50 (39–43) sr and PLDR in the range of 0.17–0.29 (0.20–0.35) at 355~~nm and 39±1 sr (0.35±0.01) at~~ (532~~nm. The PLDRs are consistent with Taklamakan dust, but~~) nm (Dieudonné et al., 2015; Murayama et al., 2004; Hofer et al., 2017, 2020; Filioglou et al., 2020). Both the lidar ratios ~~at 355 and 532 nm are both lower than in our study. Moreover, the lidar ratios at 355~~ and ~~532 nm in this case are very close. While in our study~~ PLDRs are slightly lower than the ~~lidar ratio of Taklamakan dust at 355 nm always exceeds that at 532 nm. In Saharan dust observations, both spectrally dependent and independent lidar ratios at 355~~ results we obtained from Taklamakan dust. Case 4 in this study shows the coincidence of characteristics of Taklamakan dust in the lower boundary layer and Central Asian dust (Hofer et al., 2017) in the upper boundary layer. This coincidence proves that the differences of lidar ratios and ~~532 nm have been reported. Tesche et al. (2009) found 53–55 sr at 355 and 532 nm, based on the Raman lidar measurements in SAMUM campaign at Ouarzazate. Groß et al. (2011) found lidar ratios of 48–70 sr in Cape Verde using high spectral resolution lidar. In the SHADOW2 campaign, it is found that, in the dry season (November to March), the lidar ratio was 60±9–75±11 sr at 355 nm and 45±7–55±8 sr at 532 nm. While in the transition period from the dry to wet season, the lidar ratios were about 50±8–60±9 sr at both 355 and 532 nm. The seasonal change of lidar ratios reflects the variation of dust absorption, which is resulted from the seasonal change of wind direction (Hu, 2018; Veselovskii et al., 2016, 2020)~~PLDRs between Taklamakan dust and Central Asia dust are not caused by a systematic bias of measurements in two different lidar systems, but that the two types of dust are optically different.

The ~~comparison indicates that the lidar ratios of Asian dust are generally lower than Saharan dust, which might be explained by the difference of dust absorption. Biagio et al. (2019) presented that the SSA (single scattering albedo) of Taklamakan dust sample is greater than Sahel dust, after investigating 19 dust samples collected from global dust sources. Studies found that the absorption of dust is closely correlated to~~ large fraction of coarse-mode and giant particles in Taklamakan dust are supposed to be the main reason responsible for this difference. Moreover, differences of the dust mineralogical composition in various geographical locations may also contribute to the differences in optical properties. For example, observations in SAMUM and SHADOW campaigns revealed lower PLDRs and higher lidar ratios in Saharan dust compared with Asian dust

(Groß et al., 2011; Veselovskii et al., 2016, 2020). It could be explained by the argument that Saharan dusts tend to be more absorbing than Asian dust due to its relative higher content of iron oxides ~~, whose content varies in different geographical dust source (Moosmüller et al., 2012; Biagio et al., 2019). Other factors, such as the particle size distribution, shape and so on, can also determine dust lidar ratio. Moreover, pollution could be another another that impact dust properties . In Asia, there are more potential anthropogenic pollution sources compared with in Africa. The Case 3 in this study shows that dust lidar ratios decrease when mixed with pollution. Depending on the state of mixing and the type of the mixed aerosols, the contamination of pollution could modify the properties of dust.~~ (Biagio et al., 2019).

~~The PLDRs of Asian dust, Saharan dust and American dust mostly fall in the range of 0.23–0.28~~ Recent studies concluded that there are similarities in dust size and shape parameters, which explain the relatively uniform distribution dust PLDRs for globally distributed dust sources. Nevertheless, the variability of dust properties should still be considered. PLDRs as high as Taklamakan dust have ever been found in several previous studies. Burton et al. (2015) found comparable PLDR of 0.37 at 532 nm in American dust near the source, but at 355 ~~nm. While the PLDR~~nm, the PLDR was about 0.24, falling in the typical range of dust. Sakai et al. (2010) derived PLDR (at 532 nm) of 0.39 for Asian and Saharan dust with high number concentration of supermicrometer particles, while for submicrometer particles, the PLDR was about 0.14–0.17. It proves that increase of big particle concentration could strongly increase the PLDR. Miffre et al. (2016) measured artificial dust samples with mainly submicrometer particles and derived PLDR of 0.37 at 355 nm ~~for Taklamakan dust reaches as high as 0.31–0.32. The highest PLDRs at 532~~ and ~~1064 nmhave been observed in American dust that appeared near its source region. The PLDR at 532 nm is the one measured the most often. Its values vary in the range of 0.30–0.35 when the observation site is close to the dust source. After long-range transport, the PLDR~~ 0.36 at ~~532 nmclearly decreases. Thus, we speculate that the high PLDR at 355 nm in Taklamakan dust might be linked to the distance of the observation site to the dust source. Shorter transport distance helps avoid the loss of big particles and the mixing of dust with other types of aerosols.~~532 nm. The high PLDRs are likely caused by the sharp edges and corners produced in the fabrication of dust samples. In naturally formed dust particles, these corners or edges may be trimmed by aeolian or fluvial erosion. This could be one reason why previous dust observations never found PLDR greater than 0.30 at 355 nm. While near the source and in heavy dust event, we suppose that the lifted dust may contain a fraction of big and morphologically complicated particles, which have strong depolarizing effects. Since Taklamakan dust observations in the source region are quite rare, more observational data are needed for complementing the data set of dust characteristics.

5 Conclusions

The first session of DAO campaign was conducted in Kashi, China in April 2019. The objective of DAO campaign is to provide a comprehensive characterization of Taklamakan dust using multi-wavelength Mie-Raman lidar measurements. During the nearly 1 month campaign, we found that, dust particles, originated mainly from the Taklamakan desert, are the dominant aerosol component in springtime in Kashi, while the influence of fine-mode particles needs also to be considered. Kashi is a populated region, pollution emitted from anthropogenic activities very likely the main component in fine-mode aerosols. Additionally, air mass clustering using the HYSPLIT model suggests that long-range transported aerosols from Africa, Europe, the Middle East and Central Asia could be a potential aerosol ~~source~~ origin in Kashi. This study provides the first characterization of the spectral lidar ~~ratio~~ ratios and PLDRs of the Taklamakan dust. One distinct feature of Taklamakan dust is its relatively high PLDRs compared with other Asian dust and Saharan dust. We suppose this difference is related to the coarse-mode and giant particles that remain in the Taklamakan dust near the source region. The results fill the gap of the characterization of Taklamakan dust and provide reference for succeeding studies and for implementing the climate modeling. This study also points out the importance of considering the dust mixing with pollution in climate modeling. Our results show that, in the most dusty season of the year and ~~in~~ at an observation site ~~of~~ with 150 km to the desert, the observed Taklamakan dust has already been polluted. Pollution could alter the optical and microphysical properties of dust particles, thus influencing the direct radiative ~~radiation~~forcing. Moreover, polluted dust could modify the cloud formation process by acting as cloud condensation nuclei and ice nuclei, which ~~will~~ impose indirect influence on the earth's radiation budget and the long-term climate change. ~~There is a collection of cases about the interactionsof polluted dust and clouds in the DAO campaign and this study well~~ The DAO campaign offers a nice collection of measurements relevant to cloud-dust interactions, which will be presented in the next step.

Data availability. The satellite data from OMPS and AIRS can be found in NASA's GES DIS service center. The meteorological data, GDAS data and the HYSPLIT dispersion model are available in the NOAA ARL site (https://ready.arl.noaa.gov/HYSPLIT.php). All the other data presented in this study are available upon any request of readers.

Author contributions. The project was supervised by PG and ZL. QH, TP and IV were in charge of the Lidar operation and maintenance. QH, IV and HW performed the data analysis. QH wrote the manuscript of this paper. KL provide the sun/sky photometer data. MK helped in the lidar operation and instrument preparation.

Competing interests. The authors declare that they have no conflict of interest.

Acknowledgements. We acknowledge the colleagues in the Institute of Remote Sensing and Digital Earth () for their kind help and for the financial support. And we thank the colleagues in the GPI RAS (Prokhorov General Physics Institute of the Russian Academy of Sciences), LOA ~~,~~ (Service National d'Observation, PHOTONS/AERONET-ACTRIS), ESA/~~IDEAL~~IDEAS+ project and IAP (Institue of Atmospheric Physics) for the participation and the efforts they have made for the campaign. The Russian Science Foundation, (project 16-17-10241) is acknowledged for providing lidar data processing algorithms.

References

Ansmann, A., Riebesell, M., Wandinger, U., Weitkamp, C., Voss, E., Lahmann, W., and Michaelis, W.: Combined Raman elastic-backscatter lidar for vertical profiling of moisture, aerosol extinction, backscatter, and lidar ratio, Applied Physics B: Lasers and Optics, 55, 18–28, 1992.

Ansmann, A., Bösenberg, J., Chaikovsky, A., Comerón, A., Eckhardt, S., Eixmann, R., Freudenthaler, V., Ginoux, P., Komguem, L., Linné, H., et al.: Long-range transport of Saharan dust to northern Europe: The 11–16 October 2001 outbreak observed with EARLINET, Journal of Geophysical Research: Atmospheres, 108, 2003.

Biagio, C. D., Formenti, P., Balkanski, Y., Caponi, L., Cazaunau, M., Pangui, E., Journet, E., Nowak, S., Andreae, M. O., Kandler, K., et al.: Complex refractive indices and single-scattering albedo of global dust aerosols in the shortwave spectrum and relationship to size and iron content, Atmospheric Chemistry and Physics, 19, 15 503–15 531, 2019.

Boucher, O., Randall, D., Artaxo, P., Bretherton, C., Feingold, G., Forster, P., Kerminen, V.-M., Kondo, Y., Liao, H., Lohmann, U., et al.: Clouds and aerosols, in: Climate change 2013: the physical science basis. Contribution of Working Group I to the Fifth Assessment Report of the Intergovernmental Panel on Climate Change, pp. 571–657, Cambridge University Press, 2013.

Bovchaliuk, V., Goloub, P., Podvin, T., Veselovskii, I., Tanre, D., Chaikovsky, A., Dubovik, O., Mortier, A., Lopatin, A., Korenskiy, M., et al.: Comparison of aerosol properties retrieved using GARRLiC, LIRIC, and Raman algorithms applied to multi-wavelength lidar and sun/sky-photometer data, Atmospheric Measurement Techniques, 9, 3391–3405, 2016.

Burton, S., Hair, J., Kahnert, M., Ferrare, R., Hostetler, C., Cook, A., Harper, D., Berkoff, T., Seaman, S., Collins, J., et al.: Observations of the spectral dependence of linear particle depolarization ratio of aerosols using NASA Langley airborne High Spectral Resolution Lidar, Atmospheric Chemistry and Physics, 15, 13 453–13 473, 2015.

Campbell, J. R., Reid, J. S., Westphal, D. L., Zhang, J., Hyer, E. J., and Welton, E. J.: CALIOP aerosol subset processing for global aerosol transport model data assimilation, IEEE Journal of Selected Topics in Applied Earth Observations and Remote Sensing, 3, 203–214, 2010.

Carrico, C. M., Kus, P., Rood, M. J., Quinn, P. K., and Bates, T. S.: Mixtures of pollution, dust, sea salt, and volcanic aerosol during ACE-Asia: Radiative properties as a function of relative humidity, Journal of Geophysical Research: Atmospheres, 108, 2003.

Dieudonné, E., Chazette, P., Marnas, F., Totems, J., and Shang, X.: Lidar profiling of aerosol optical properties from Paris to Lake Baikal (Siberia), Atmospheric Chemistry and Physics, 15, 5007–5026, 2015.

Doxsey-Whitfield, E., MacManus, K., Adamo, S. B., Pistolesi, L., Squires, J., Borkovska, O., and Baptista, S. R.: Taking advantage of the improved availability of census data: a first look at the gridded population of the world, version 4, Papers in Applied Geography, 1, 226–234, 2015.

Engelstaedter, S., Tegen, I., and Washington, R.: North African dust emissions and transport, Earth-Science Reviews, 79, 73–100, 2006.

Esselborn, M., Wirth, M., Fix, A., Weinzierl, B., Rasp, K., Tesche, M., and Petzold, A.: Spatial distribution and optical properties of Saharan dust observed by airborne high spectral resolution lidar during SAMUM 2006, Tellus B: Chemical and Physical Meteorology, 61, 131–143, 2009.

Fan, J., Wang, Y., Rosenfeld, D., and Liu, X.: Review of aerosol–cloud interactions: Mechanisms, significance, and challenges, Journal of the Atmospheric Sciences, 73, 4221–4252, 2016.

Filioglou, M., Giannakaki, E., Backman, J., Kesti, J., Hirsikko, A., Engelmann, R., O'Connor, E., Leskinen, J. T. T., Shang, X., Korhonen, H., Lihavainen, H., Romakkaniemi, S., and Komppula, M.: Optical and geometrical aerosol particle properties over the United Arab Emirates, Atmospheric Chemistry and Physics, 20, 8909–8922, https://doi.org/10.5194/acp-20-8909-2020, https://acp.copernicus.org/articles/20/8909/2020/, 2020.

Flynn, L. E., Homstein, J., and Hilsenrath, E.: The ozone mapping and profiler suite (OMPS). The next generation of US ozone monitoring instruments, in: Geoscience and Remote Sensing Symposium, 2004. IGARSS'04. Proceedings. 2004 IEEE International, vol. 1, IEEE, 2004.

Freudenthaler, V., Esselborn, M., Wiegner, M., Heese, B., Tesche, M., Ansmann, A., Müller, D., Althausen, D., Wirth, M., Fix, A., Ehret, G., Knippertz, P., Toledano, C., Gasteiger, J., Garhammer, M., and Seefeldner, M.: Depolarization ratio profiling at several wavelengths in pure Saharan dust during SAMUM 2006, Tellus B, 61, 165–179, 2009.

Ginoux, P., Prospero, J. M., Gill, T. E., Hsu, N. C., and Zhao, M.: Global-scale attribution of anthropogenic and natural dust sources and their emission rates based on MODIS Deep Blue aerosol products, Reviews of Geophysics, 50, 2012.

Groß, S., Tesche, M., Freudenthaler, V., Toledano, C., Wiegner, M., Ansmann, A., Althausen, D., and Seefeldner, M.: Characterization of Saharan dust, marine aerosols and mixtures of biomass-burning aerosols and dust by means of multi-wavelength depolarization and Raman lidar measurements during SAMUM 2, Tellus B: Chemical and Physical Meteorology, 63, 706–724, 2011.

Groß, S., Freudenthaler, V., Schepanski, K., Toledano, C., Schäfler, A., Ansmann, A., and Weinzierl, B.: Optical properties of long-range transported Saharan dust over Barbados as measured by dual-wavelength depolarization Raman lidar measurements, Atmospheric Chemistry and Physics, pp. 11 067–11 080, 2015.

Haarig, M., Ansmann, A., Althausen, D., Klepel, A., Groß, S., Freudenthaler, V., Toledano, C., Mamouri, R.-E., Farrell, D. A., Prescod, D. A., et al.: Triple-wavelength depolarization-ratio profiling of Saharan dust over Barbados during SALTRACE in 2013 and 2014, Atmospheric Chemistry and Physics, 17, 10 767, 2017.

Hofer, J., Althausen, D., Abdullaev, S. F., Makhmudov, A. N., Nazarov, B. I., Schettler, G., Engelmann, R., Baars, H., Fomba, K. W., Müller, K., et al.: Long-term profiling of mineral dust and pollution aerosol with multiwavelength polarization Raman lidar at the Central Asian site of Dushanbe, Tajikistan: case studies, Atmospheric Chemistry and Physics, 17, 14 559, 2017.

Hofer, J., Ansmann, A., Althausen, D., Engelmann, R., Baars, H., Fomba, K. W., Wandinger, U., Abdullaev, S. F., and Makhmudov, A. N.: Optical properties of Central Asian aerosol relevant for spaceborne lidar applications and aerosol typing at 355 and 532 nm, Atmospheric Chemistry and Physics, 20, 9265–9280, https://doi.org/10.5194/acp-20-9265-2020, https://acp.copernicus.org/articles/20/9265/2020/, 2020.

Holben, B. N., Eck, T. F., Slutsker, I., Tanre, D., Buis, J., Setzer, A., Vermote, E., Reagan, J., Kaufman, Y., Nakajima, T., et al.: AERONET—A federated instrument network and data archive for aerosol characterization, Remote sensing of environment, 66, 1–16, 1998.

Hsu, N. C., Herman, J., Torres, O., Holben, B., Tanre, D., Eck, T., Smirnov, A., Chatenet, B., and Lavenu, F.: Comparisons of the TOMS aerosol index with Sun-photometer aerosol optical thickness: Results and applications, Journal of Geophysical Research: Atmospheres, 104, 6269–6279, 1999.

Hu, Q.: Advanced aerosol characterization using sun/sky photometer and multi-wavelength Mie-Raman lidar measurements, Ph.D. thesis, Lille 1, 2018.

Hu, Q., Goloub, P., Veselovskii, I., Bravo-Aranda, J.-A., Popovici, I. E., Podvin, T., Haeffelin, M., Lopatin, A., Dubovik, O., Pietras, C., et al.: Long-range-transported Canadian smoke plumes in the lower stratosphere over northern France, Atmospheric Chemistry and Physics, 19, 1173–1193, 2019.

Huang, J., Minnis, P., Chen, B., Huang, Z., Liu, Z., Zhao, Q., Yi, Y., and Ayers, J. K.: Long-range transport and vertical structure of Asian dust from CALIPSO and surface measurements during PACDEX, Journal of Geophysical Research: Atmospheres, 113, 2008.

Huang, K., Zhuang, G., Li, J., Wang, Q., Sun, Y., Lin, Y., and Fu, J. S.: Mixing of Asian dust with pollution aerosol and the transformation of aerosol components during the dust storm over China in spring 2007, Journal of Geophysical Research: Atmospheres, 115, 2010.

Huneeus, N., Schulz, M., Balkanski, Y., Griesfeller, J., Prospero, M., Kinne, S., Bauer, S., Boucher, O., Chin, M., Dentener, F., et al.: Global dust model intercomparison in AeroCom phase I, Atmospheric Chemistry and Physics, 11, 7781–7816, 2011.

Iwasaka, Y., Shi, G.-Y., Yamada, M., Matsuki, A., Trochkine, D., Kim, Y., Zhang, D., Nagatani, T., Shibata, T., Nagatani, M., et al.: Importance of dust particles in the free troposphere over the Taklamakan Desert: electron microscopic experiments of particles collected with a balloonborne particle impactor at Dunhuang, China, Journal of Geophysical Research: Atmospheres, 108, 2003.

Iwasaka, Y., Li, J., Shi, G.-Y., Kim, Y., Matsuki, A., Trochkine, D., Yamada, M., Zhang, D., Shen, Z., and Hong, C.: Mass transport of background Asian dust revealed by balloon-borne measurement: dust particles transported during calm periods by westerly from Taklamakan desert, in: Advanced environmental monitoring, pp. 121–135, Springer, 2008.

Jin, Y., Kai, K., Shibata, T., Zhang, K., and Zhou, H.: Validation of the dust layer structure over the Taklimakan Desert, China by the CALIOP space-borne lidar using ground-based lidar, Sola, 6, 121–124, 2010.

Kai, K., Nagata, Y., Tsunematsu, N., Matsumura, T., Kim, H.-S., Matsumoto, T., Hu, S., Zhou, H., Abo, M., and Nagai, T.: The Structure of the Dust Layer over the Taklimakan Deser during the Dust Storm in April 2002 as Observed Using a Depolarization Lidar, Journal of the Meteorological Society of Japan. Ser. II, 86, 1–16, 2008.

Kandler, K., Schütz, L., Deutscher, C., Ebert, M., Hofmann, H., Jäckel, S., Jaenicke, R., Knippertz, P., Lieke, K., Massling, A., et al.: Size distribution, mass concentration, chemical and mineralogical composition and derived optical parameters of the boundary layer aerosol at Tinfou, Morocco, during SAMUM 2006, Tellus B: Chemical and Physical Meteorology, 61, 32–50, 2009.

Kandler, K., Lieke, K., Benker, N., Emmel, C., Küpper, M., Müller-Ebert, D., Ebert, M., Scheuvens, D., Schladitz, A., Schütz, L., et al.: Electron microscopy of particles collected at Praia, Cape Verde, during the Saharan Mineral Dust Experiment: particle chemistry, shape, mixing state and complex refractive index, Tellus B: Chemical and Physical Meteorology, 63, 475–496, 2011.

Kanji, Z. A., Ladino, L. A., Wex, H., Boose, Y., Burkert-Kohn, M., Cziczo, D. J., and Krämer, M.: Overview of Ice Nucleating Particles, Meteorological Monographs, 58, 1.1–1.33, https://doi.org/10.1175/AMSMONOGRAPHS-D-16-0006.1, https://doi.org/10.1175/AMSMONOGRAPHS-D-16-0006.1, 2017.

Klett, J. D.: Lidar inversion with variable backscatter/extinction ratios, Applied Optics, 24, 1638–1643, 1985.

Kojima, T., Buseck, P. R., Iwasaka, Y., Matsuki, A., and Trochkine, D.: Sulfate-coated dust particles in the free troposphere over Japan, Atmospheric research, 82, 698–708, 2006.

Li, Z., Xu, H., Li, K., Li, D., Xie, Y., Li, L., Zhang, Y., Gu, X., Zhao, W., Tian, Q., et al.: Comprehensive study of optical, physical, chemical, and radiative properties of total columnar atmospheric aerosols over China: an overview of sun–sky radiometer observation network (SONET) measurements, Bulletin of the American Meteorological Society, 99, 739–755, 2018.

Littmann, T.: Dust storm frequency in Asia: climatic control and variability, International Journal of Climatology, 11, 393–412, 1991.

Liu, Z., Sugimoto, N., and Murayama, T.: Extinction-to-backscatter ratio of Asian dust observed with high-spectral-resolution lidar and Raman lidar, Applied Optics, 41, 2760–2767, 2002.

Miffre, A., Mehri, T., Francis, M., and Rairoux, P.: UV–VIS depolarization from Arizona Test Dust particles at exact backscattering angle, Journal of Quantitative Spectroscopy and Radiative Transfer, 169, 79–90, 2016.

Moosmüller, H., Engelbrecht, J. P., Skiba, M., Frey, G., Chakrabarty, R. K., and Arnott, W. P.: Single scattering albedo of fine mineral dust aerosols controlled by iron concentration, Journal of Geophysical Research: Atmospheres, 117, 2012.

Murayama, T., Müller, D., Wada, K., Shimizu, A., Sekiguchi, M., and Tsukamoto, T.: Characterization of Asian dust and Siberian smoke with multi-wavelength Raman lidar over Tokyo, Japan in spring 2003, Geophysical Research Letters, 31, 2004.

Pan, X., Yan, P., Tang, J., Ma, J., Wang, Z., Gbaguidi, A., and Sun, Y.: Observational study of influence of aerosol hygroscopic growth on scattering coefficient over rural area near Beijing mega-city., Atmospheric Chemistry & Physics, 9, 2009.

Park, C. B., Sugimoto, N., Matsui, I., Shimizu, A., Tatarov, B., Kamei, A., Lee, C. H., Uno, I., Takemura, T., and Westphal, D. L.: Long-range transport of Saharan dust to east Asia observed with lidars, Sola, 1, 121–124, 2005.

Petrov, M. P. and S.Alitto, G.: Takla Makan Desert, https://www.britannica.com/place/Takla-Makan-Desert, 2019.

Qian, W., Quan, L., and Shi, S.: Variations of the dust storm in China and its climatic control, Journal of Climate, 15, 1216–1229, 2002.

Reed, K. A., Bacmeister, J. T., Huff, J. J. A., Wu, X., Bates, S. C., and Rosenbloom, N. A.: Exploring the Impact of Dust on North Atlantic Hurricanes in a High-Resolution Climate Model, Geophysical Research Letters, 46, 1105–1112, 2019.

Rolph, G., Stein, A., and Stunder, B.: Real-time environmental applications and display system: Ready, Environmental Modelling & Software, 95, 210–228, 2017.

Ryder, C. L., Marenco, F., Brooke, J. K., Estelles, V., Cotton, R., Formenti, P., McQuaid, J. B., Price, H. C., Liu, D., Ausset, P., Rosenberg, P. D., Taylor, J. W., Choularton, T., Bower, K., Coe, H., Gallagher, M., Crosier, J., Lloyd, G., Highwood, E. J., and Murray, B. J.: Coarse-mode mineral dust size distributions, composition and optical properties from AER-D aircraft measurements over the tropical eastern Atlantic, Atmospheric Chemistry and Physics, 18, 17 225–17 257, https://doi.org/10.5194/acp-18-17225-2018, https://acp.copernicus.org/articles/18/17225/2018/, 2018.

Sakai, T., Nagai, T., Zaizen, Y., and Mano, Y.: Backscattering linear depolarization ratio measurements of mineral, sea-salt, and ammonium sulfate particles simulated in a laboratory chamber, Applied optics, 49, 4441–4449, 2010.

Seftor, C., Jaross, G., Kowitt, M., Haken, M., Li, J., and Flynn, L.: Postlaunch performance of the Suomi National Polar-orbiting Partnership Ozone Mapping and Profiler Suite (OMPS) nadir sensors, Journal of Geophysical Research: Atmospheres, 119, 4413–4428, 2014.

Sekiyama, T., Tanaka, T., Shimizu, A., and Miyoshi, T.: Data assimilation of CALIPSO aerosol observations., Atmospheric Chemistry & Physics, 10, 2010.

Shi, Z., Zhang, D., Hayashi, M., Ogata, H., Ji, H., and Fujiie, W.: Influences of sulfate and nitrate on the hygroscopic behaviour of coarse dust particles, Atmospheric Environment, 42, 822–827, 2008.

Stein, A., Draxler, R. R., Rolph, G. D., Stunder, B. J., Cohen, M., and Ngan, F.: NOAA's HYSPLIT atmospheric transport and dispersion modeling system, Bulletin of the American Meteorological Society, 96, 2059–2077, 2015.

Sugimoto, N., Shimizu, A., Nishizawa, T., and Jin, Y.: Long-range transport of mineral dust observed with the Asian Dust and aerosol lidar observation Network (AD-Net), in: E3S Web of Conferences, vol. 99, EDP Sciences, 2019.

Sun, J. and Liu, T.: The age of the Taklimakan Desert, Science, 312, 1621–1621, 2006.

Tanaka, T. Y. and Chiba, M.: A numerical study of the contributions of dust source regions to the global dust budget, Global and Planetary Change, 52, 88–104, 2006.

Tanaka, T. Y., Kurosaki, Y., Chiba, M., Matsumura, T., Nagai, T., Yamazaki, A., Uchiyama, A., Tsunematsu, N., and Kai, K.: Possible transcontinental dust transport from North Africa and the Middle East to East Asia, Atmospheric Environment, 39, 3901–3909, 2005.

Tesche, M., Ansmann, A., Mueller, D., Althausen, D., Mattis, I., Heese, B., Freudenthaler, V., Wiegner, M., Esselborn, M., Pisani, G., et al.: Vertical profiling of Saharan dust with Raman lidars and airborne HSRL in southern Morocco during SAMUM, Tellus B: Chemical and Physical Meteorology, 61, 144–164, 2009.

Textor, C., Schulz, M., Guibert, S., Kinne, S., Balkanski, Y., Bauer, S., Berntsen, T., Berglen, T., Boucher, O., Chin, M., et al.: Analysis and quantification of the diversities of aerosol life cycles within AeroCom, Atmospheric Chemistry and Physics, 6, 1777–1813, 2006.

Thompson, A. J., Skinner, C. B., Poulsen, C. J., and Zhu, J.: Modulation of mid-Holocene African rainfall by dust aerosol direct and indirect effects, Geophysical Research Letters, 46, 3917–3926, 2019.

Uno, I., Eguchi, K., Yumimoto, K., Takemura, T., Shimizu, A., Uematsu, M., Liu, Z., Wang, Z., Hara, Y., and Sugimoto, N.: Asian dust transported one full circuit around the globe, Nature Geoscience, 2, 557–560, 2009.

VanCuren, R. A. and Cahill, T. A.: Asian aerosols in North America: Frequency and concentration of fine dust, Journal of Geophysical Research: Atmospheres, 107, AAC–19, 2002.

Veselovskii, I., Whiteman, D., Korenskiy, M., Suvorina, A., and Pérez-Ramírez, D.: Use of rotational Raman measurements in multiwavelength aerosol lidar for evaluation of particle backscattering and extinction, Atmospheric Measurement Techniques, 8, 4111–4122, 2015.

Veselovskii, I., Goloub, P., Podvin, T., Bovchaliuk, V., Derimian, Y., Augustin, P., Fourmentin, M., Tanre, D., Korenskiy, M., Whiteman, D., et al.: Retrieval of optical and physical properties of African dust from multiwavelength Raman lidar measurements during the SHADOW campaign in Senegal, Atmos. Chem. Phys, 16, 7013–7028, 2016.

Veselovskii, I., Hu, Q., Goloub, P., Podvin, T., Korenskiy, M., Derimian, Y., Legrand, M., and Castellanos, P.: Variability of Lidar-Derived Particle Properties Over West Africa Due to Changes in Absorption: Towards an Understanding, Atmospheric Chemistry and Physics Discussions, 2020, 1–37, https://doi.org/10.5194/acp-2020-98, https://www.atmos-chem-phys-discuss.net/acp-2020-98/, 2020.

Wang, Y., Sartelet, K., Bocquet, M., and Chazette, P.: Assimilation of ground versus lidar observations for PM10 forecasting, Atmospheric Chemistry and Physics, 13, 269–283, https://doi.org/10.5194/acp-13-269-2013, https://hal.inria.fr/hal-00783554, 2013.

Yu, Y., Kalashnikova, O. V., Garay, M. J., and Notaro, M.: Climatology of Asian dust activation and transport potential based on MISR satellite observations and trajectory analysis, Atmospheric Chemistry and Physics, 19, 363–378, 2019.

Yumimoto, K., Uno, I., Sugimoto, N., Shimizu, A., Liu, Z., and Winker, D.: Adjoint inversion modeling of Asian dust emission using lidar observations, Atmospheric Chemistry and Physics, 8, 2869–2884, 2008.

Yumimoto, K., Eguchi, K., Uno, I., Takemura, T., Liu, Z., Shimizu, A., and Sugimoto, N.: An elevated large-scale dust veil from the Taklimakan Desert: Intercontinental transport and three-dimensional structure as captured by CALIPSO and regional and global models, Atmospheric Chemistry and Physics, 9, 8545–8558, 2009.

Zhang, J., Campbell, J. R., Reid, J. S., Westphal, D. L., Baker, N. L., Campbell, W. F., and Hyer, E. J.: Evaluating the impact of assimilating CALIOP-derived aerosol extinction profiles on a global mass transport model, Geophysical research letters, 38, 2011.

Zhang, J., Hu, M.-M., Wang, Y.-Y., and Shu, H.-B.: TRIM32 protein modulates type I interferon induction and cellular antiviral response by targeting MITA/STING protein for K63-linked ubiquitination, Journal of Biological Chemistry, 287, 28 646–28 655, 2012.

Table 1. Daily averaged AOD at 500 nm and Ångström exponent (between 440 and 870 nm) measured by the sun/sky photometer in daytime. The values on the right side of '±' represent the standard deviation of the values on the left side.

	AOD$_{500}$	AE$_{440-870}$
Case 1, 09 April	1.48±0.10	0.04±0.02
Case 2, 24 April	3.63±1.28	-0.01±0.03
Case 3, 15 April	0.63±0.03	0.10±0.02
Case 4, 03 April	0.49±0.16	0.11±0.03

Table 2. A summary of optical properties derived from lidar observations in the case studies. The values before the '±' symbol represent the mean in the range of the layer height. The values after the '±' symbol represent the statistical error of the values before the symbol.

	Case 1: **dust haze** 15:00–16:00 09 April	**Case 2:** **dust storm** 15:00–16:00 24 April	**Case 3:** **polluted dust** 15:00–16:00 15 April		**Case 4:** **polluted dust** 15:00–16:00 03 April	
Layer height [m]	800–3800	800–2000	1000–2200	2400–2800	1000–1500	1500–3000
PLDR$_{355}$	0.32±0.05	0.32±0.05	0.32±~~0.05~~ 0.07	0.23±~~0.03~~ 0.06	0.30–0.32±~~0.05~~ 0.07	0.21±~~0.03~~0.05–0.29±~~0.04~~ 0.0
PLDR$_{532}$	0.36±0.05	0.36±0.05	0.34±0.05	0.26±0.03	0.35±0.05	0.28±0.04–0.34±0.05
(V)PLDR$_{1064}$	0.31±0.04[a]	–	0.31±0.04	0.24±0.03	0.32±0.05	0.28±0.04–0.33±0.05
LR$_{355}$ [sr]	56±8	55[b]	51±8	42±6	51±8	43±6–57±8
LR$_{532}$ [sr]	46±7	45[b]	45±7	40±6	45±7	38±6–49±8
EAE$_{355-532}$	-0.01±0.30	0.01±~~0.3~~ 0.30	0.02±0.30	0.10±0.30	0.02±0.30	0.14±0.30–0.30±0.30
BAE$_{355-532}$	-0.51±0.30	–	-0.29±0.30	-0.06±0.30	-0.29±0.30	-0.13±0.30–0.20±0.30
RH [%]	20±4–60±12	10±2–20±4	30±6–60±12	80±16	20±4–60±12	45±9–70±14
WVMR [g/kg]	2.2±0.5	–	3.5±7	4.0±0.8	2.7±0.6	2.7±0.6

[a] PLDR$_{1064}$ is not available in this case, but VLDR$_{1064}$ is. We assume VLDR$_{1064}$≈PLDR$_{1064}$ considering aerosol scattering is much stronger than molecular scattering. [b] 55 and 45 sr are assum lidar ratios based on the results in Case 1.

Table 3. A review of dust lidar ratios and particle linear depolarization ratios in literatures. The values of lidar ratios and PLDRs, as well as their errors are based on the results in the references. Error estimates are not provided if their are not available in the original publication.

Dust source	Observation site	PLDRs 355	PLDRs 532	PLDRs 1064	LRs 355	LRs 532	Reference
Saharan dust	Ouarzazate^{1a}	–	0.30	–	–	38–50	Esselborn et al. (2009)
	Ouarzazate^{1b}	–	–	–	53–55	53–55	Tesche et al. (2009)
	Cape Verde	0.24–0.27	0.29–0.31	–	48–70	48–70	Groß et al. (2011)
	M'~~bour~~Bour^{2a}	–	0.34±0.05	–	68±10	50±8	Veselovskii et al. (2016)
	M'~~bour~~Bour^{2b}	–	0.32±0.05	–	55–60±9	55–60±8	Veselovskii et al. (2020)
	Leipzig	–	0.15-0.25		50–90	40–80	Ansmann et al. (2003)
	Barbados	0.26±0.03	0.27±0.01	–	53±5	56±7	Groß et al. (2015)
	Barbados	0.25±0.03	0.28±0.02	0.23±0.02	40–60	40–60	Haarig et al. (2017)
Asian dust	Aksu	–	–	–	–	42±3	Jin et al. (2010)
	Japan	–	0.20	–	49	43	Murayama et al. (2004)
	Kazan	0.23±0.02	–	–	43±14	–	Dieudonné et al. (2015)
	Omsk	0.17±0.02	–	–	50±13	–	
	Dushanbe^{3a}	0.23±0.01	0.35±0.01	–	47±2	43±3	Hofer et al. (2017)
	Dushanbe^{3b}	0.29±0.01	0.35±0.01	–	40±1	39±1	
	Dushanbe^{3c}	0.24±0.03	0.33±0.04	–	43±3	39±4	Hofer et al. (2020)
	UAE	0.25±0.02	0.31±0.02	–	45±5	42±5	Filioglou et al. (2020)
	Kashi	0.28±~~0.04~~ 0.07 – 0.32±~~0.05~~ 0.07	~~0.35~~0.36±0.05	0.31±0.05	51±8 – 56±8	45±7	This study
American dust	Chihuahuan	0.24±0.05	0.37±0.02	0.38±0.01	–	–	Burton et al. (2015)
	Pico de Orizaba	–	0.33±0.02	0.40±0.01	–	–	Burton et al. (2015)

^{1a}HSRL measurements; ^{1b}Raman lidar measurement; ^{2a} 29 March 2015 in the dry season; ^{2b}23–24 April 2015 in the transition period; ^{3a}Extreme dust case on 8 August 2015, ^{3b}Most extreme dust case on 14 July 2016; ^{3c} Statistical results estimated from 17 dust cases with $\mathrm{PLDR}_{532} > 0.31$.

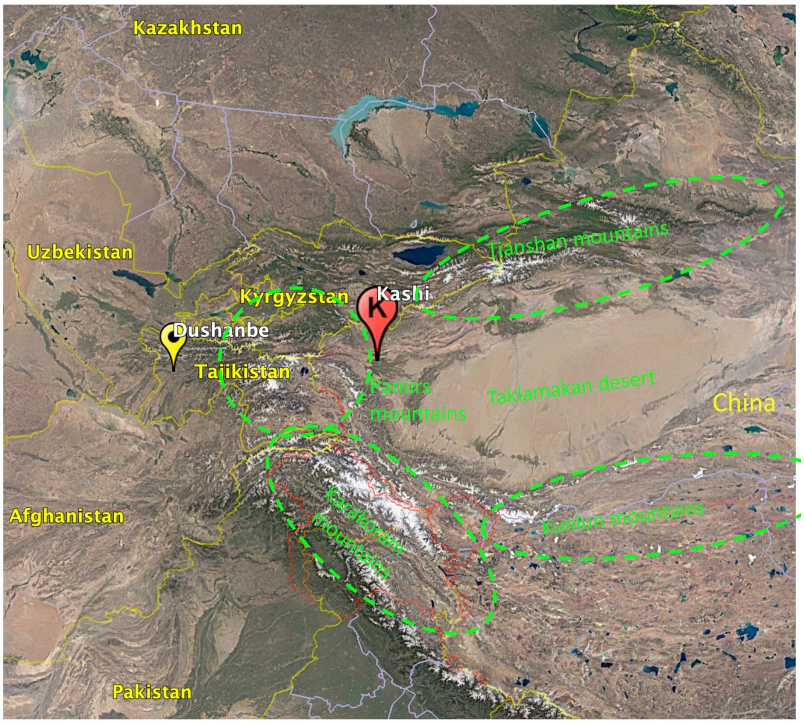

Figure 1. The location of the observation site in Kashi (at 39.51N, 75.93E). The ~~black~~ observation site is about 628 km in the east of Dushanbe, Tajikistan (38.53N, 68.77E). The green ellipses indicate the mountain ranges surrounding the Taklamakan desert, including the Tianshan mountains, the Pamir mountains, the Karakoram mountains, the Kunlun and Altun mountains. @ Google Maps 2020.

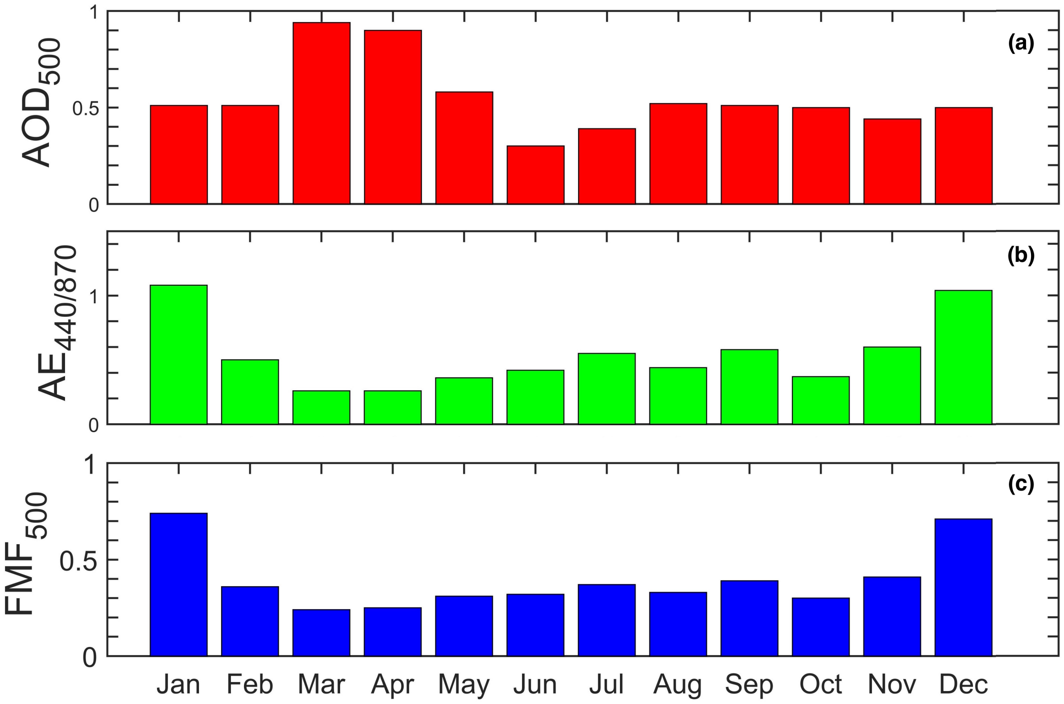

Figure 2. Monthly means of (a) the AOD at 500 nm, (b) Angström exponent (440–870) and (c) FMF at 500 nm from 2013 to 2017. The data are obtained from the SONET network.

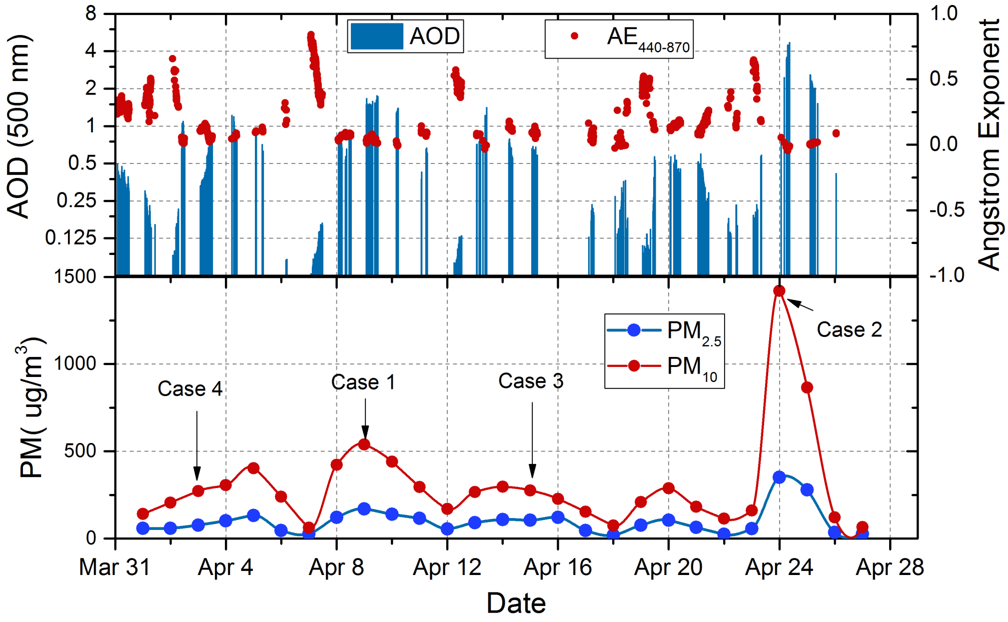

Figure 3. The AOD at 500 nm, Angström exponent (440–870) and daily particulate matter (in $\mu g m^{-3}$) in April 2019. The ~~AOD and AE~~ AODs are measured by the sun/sky photometer deployed in Kashi site, and the data are stored in the SONET network. The particulate matter measurements are public data ~~come~~ from ~~the~~ a meteorological station, 5 km to the observation site.

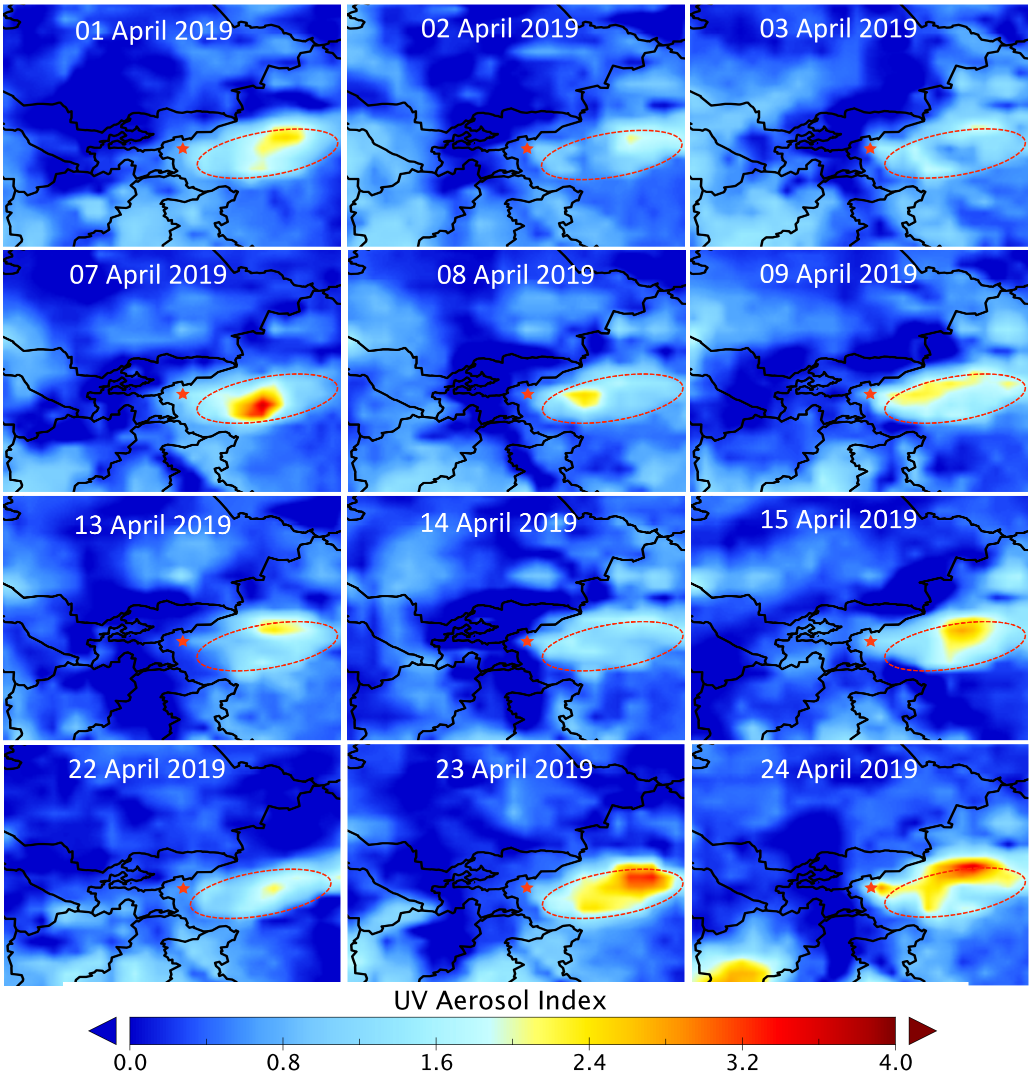

Figure 4. The UVAI derived from OMPS instrument onboard the Suomi-NPP satellite. The red star represents the location of the observation site. The dashed red ellipse represents the location of the Taklamakan desert.

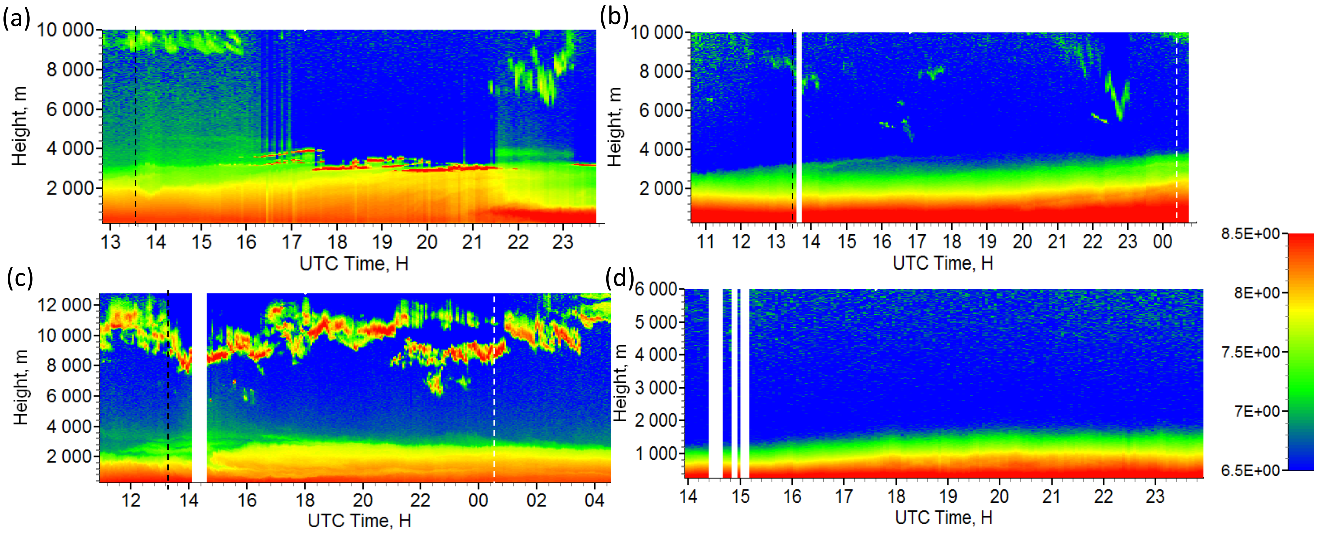

Figure 5. The ~~quicklook~~ quicklooks of the range-corrected lidar ~~siganl~~ signal at 532 nm in the four cases: (a) Case 4: 03 April 2019, (b) Case 1: 09 April 2019, (c) Case 3: 15 April 2019and (d) Case 2: 24 April 2019. The dashed black lines represent the sunset time and dashed white lines represent the sunrise time.

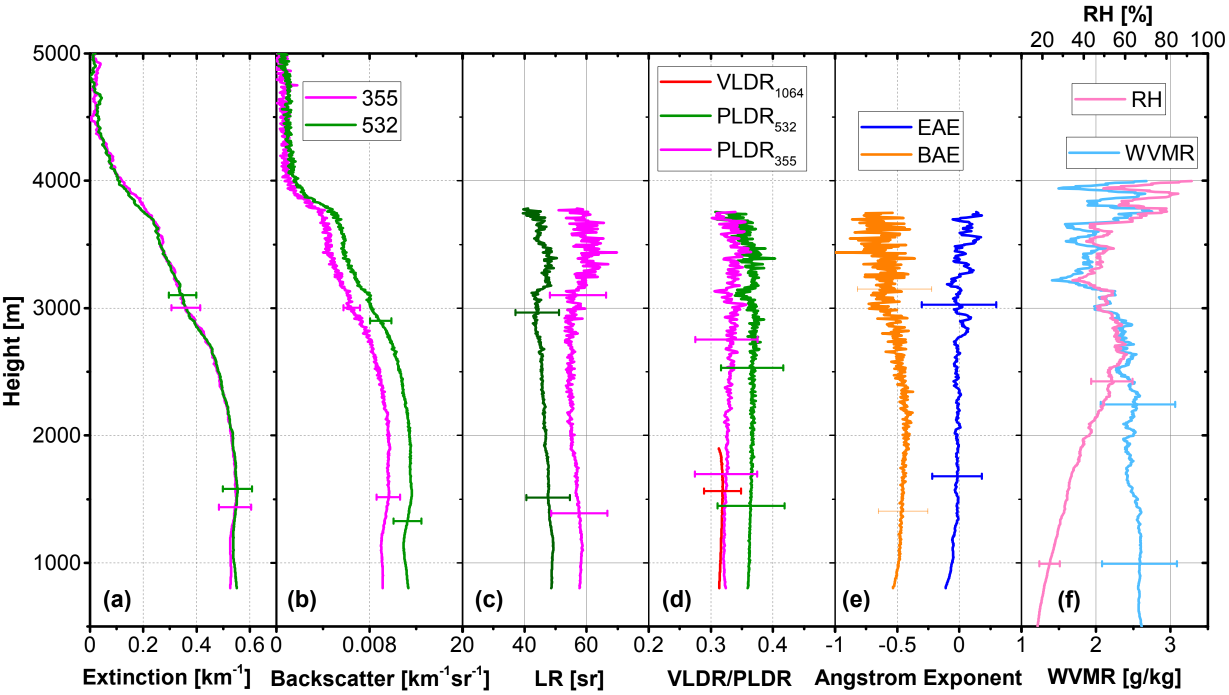

Figure 6. Case 1: Lidar derived parameters at 17:00–22:00 UTC, 09 April 2019. (a) Extinction coefficient, (b) backscattering coefficient, (c) lidar ratio, (d) PLDR/VLDR, (e) ~~Angström expoent~~ EAE$_{355-532}$ and BAE$_{355-532}$, (f) WVMR and ~~relative humidity~~RH.

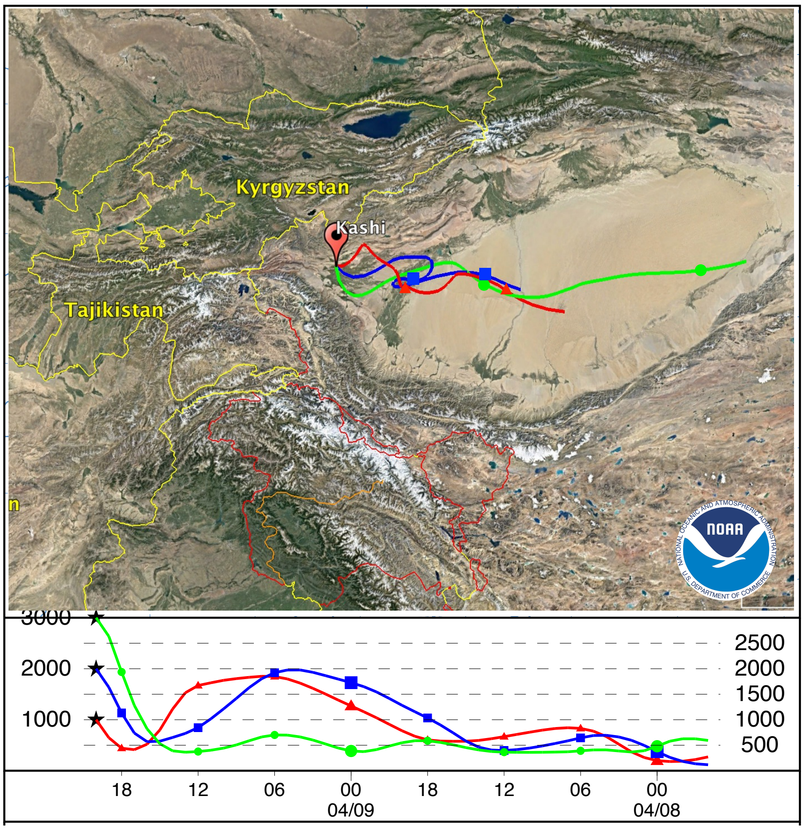

Figure 7. Case 1: The 48-hour back trajectories ending at ~~19~~20:00 UTC, 09 April 2019 for air mass at 1000, 2000 and 3000 m. @ Google Maps 2020.

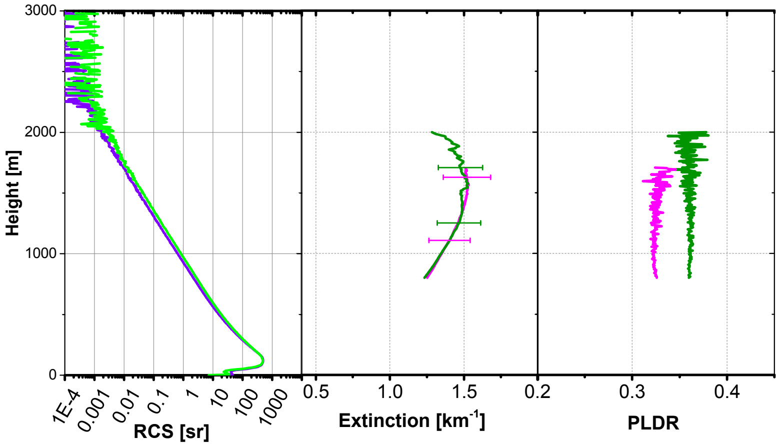

Figure 8. Case 2: Lidar derived parameters at 15:00–24:00 UTC, 24 April 2019. (a) The Raman lidar signals at 530 and 387 nm. (b) The extinction coefficients at 355 and 532 nm. (c) The PLDRs at 355 and 532 nm.

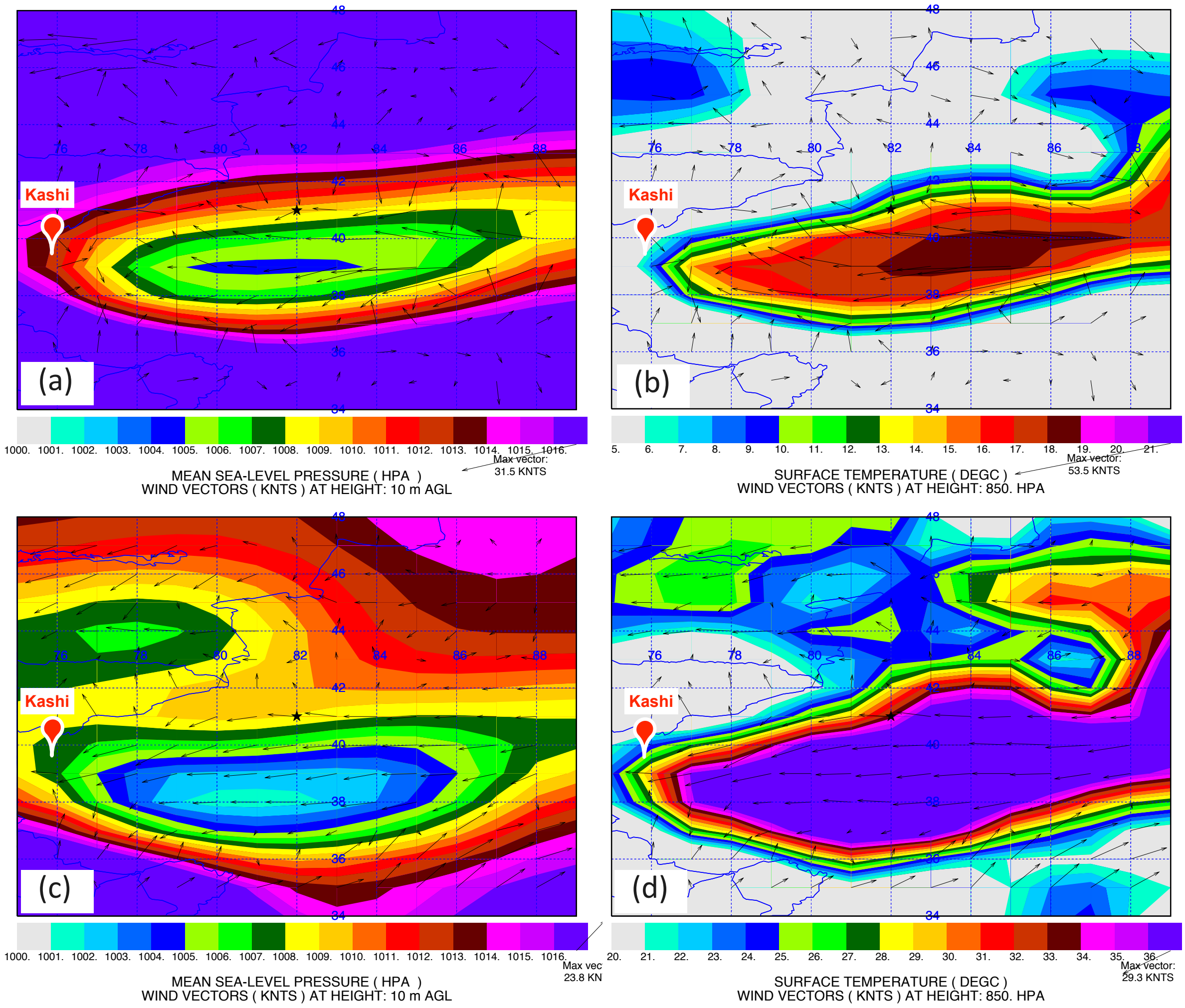

Figure 9. Case 2: The synoptic condition at 00:00 UTC, 23 April (a, b) and 06:00 UTC, 24 April (c, d), 2019. The data are obtained from the 1-degree GDAS archived meteorological data. (a) and (c) The mean sea level pressure at the surface overlaid with wind vector at 10 m above the ground level. (b) and (d) The temperature at 2 m vertical level overlaid with wind vector at 850 hPa vertical level.

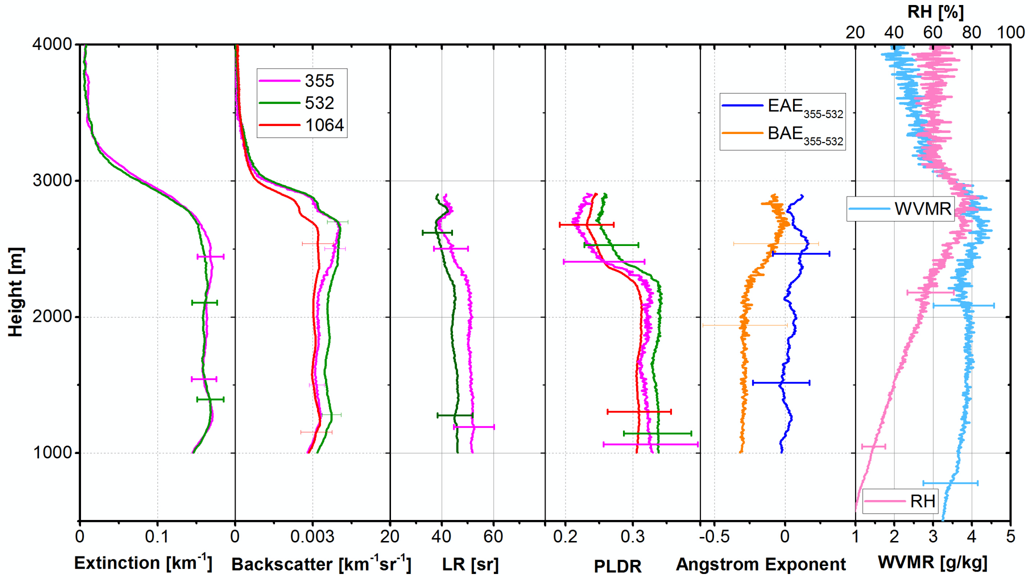

Figure 10. Case 3: Lidar derived parameters at 18:00–20:00 UTC, 15 April 2019. (a) Extinction coefficient, (b) backscattering coefficient, (c) lidar ratio, (d) PLDR, (e) ~~Ångström exponent~~ EAE$_{355-532}$ and BAE$_{355-532}$, (f) WVMR and ~~relative humidity~~RH.

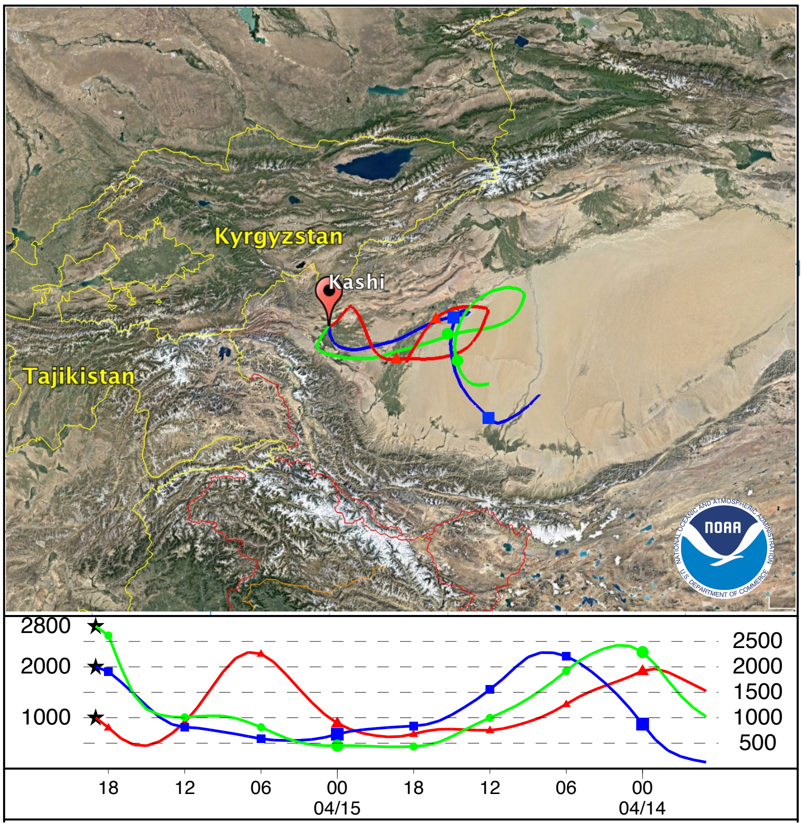

Figure 11. Case 3: The 48-hour back trajectories ending at 19:00 UTC, 15 April 2019 for air mass at 1000, 2000 and 2800 m. @ Google Maps 2020.

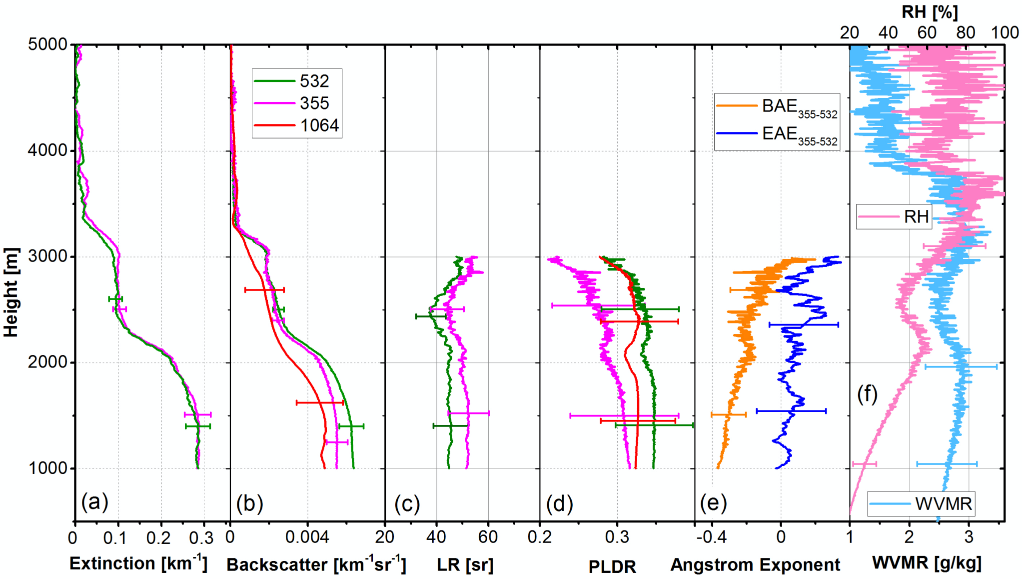

Figure 12. Case 4: Lidar derived parameters at 14:00–16:00 UTC, 03 April 2019. (a) Extinction coefficient, (b) backscattering coefficient, (c) lidar ratio, (d) PLDR, (e) ~~Ångström exponent~~ EAE$_{355-532}$ and BAE$_{355-532}$, (f) WVMR and ~~relative humidity~~RH.

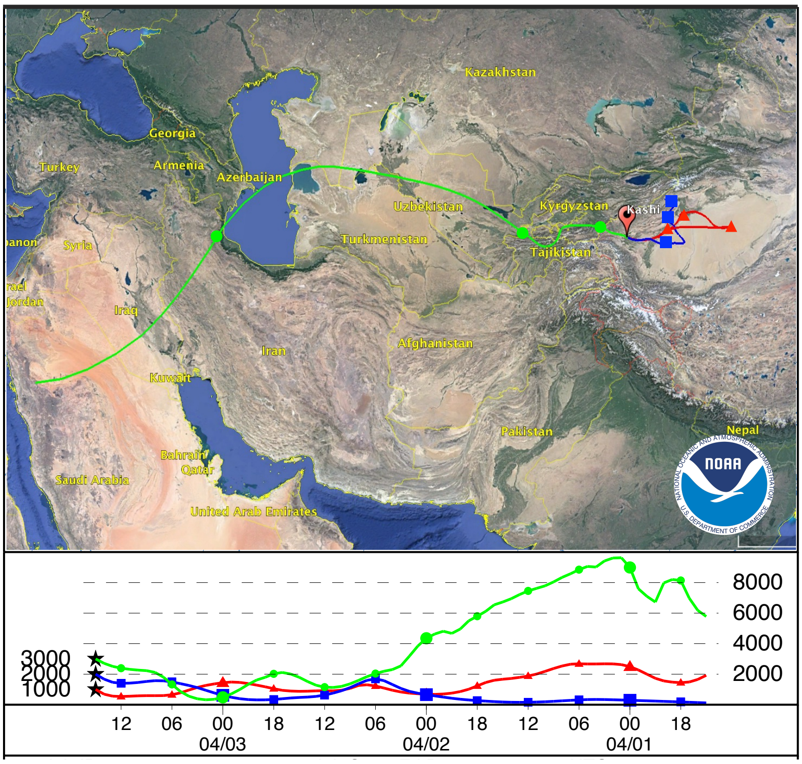

Figure 13. Case 4: The 72-hour back trajectories ending at 15:00 UTC, 03 April 2019 for air mass at 1000, 2000 and 3000 m. @ Google Maps 2020.

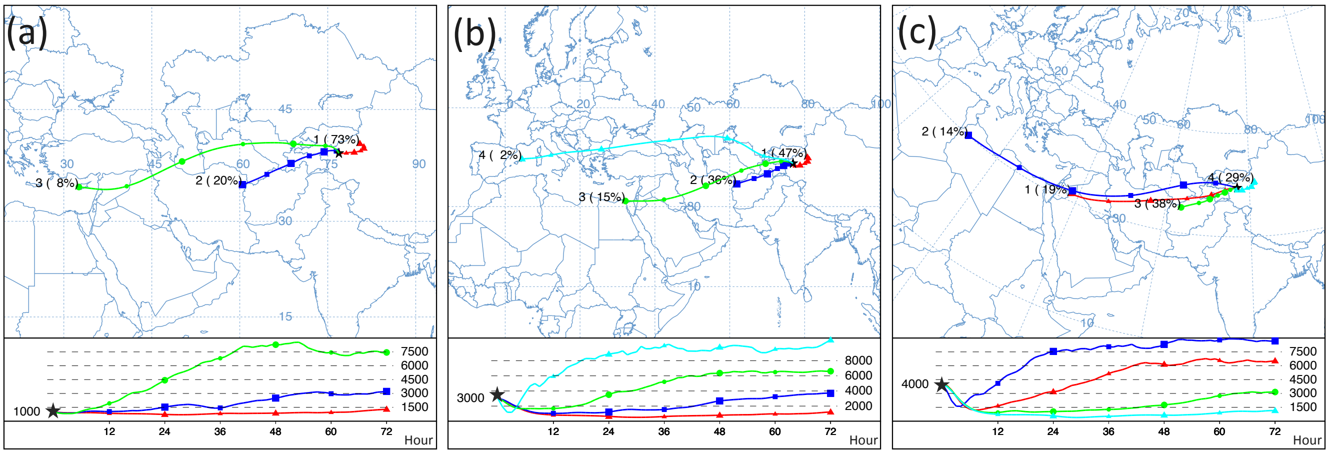

Figure 14. The clustering of air mass in April 2019. The clustering is performed using HYSPLIT and based on back trajectories with a 2-hour time resolution and 72-hour duration. (a) 1000 m, (b) 3000 m, (c) 4000 m.